ON THE EFFICIENCY OF RETRANSMISSION SCHEMES FOR THE OPEN AREA MM-WAVE DEVICE-TO-DEVICE ENVIRONMENT

By

SWAPNIL MHASKE

A dissertation submitted to the

School of Graduate Studies

Rutgers, The State University of New Jersey

In partial fulfillment of the requirements

For the degree of

Doctor of Philosophy

Graduate Program in Electrical and Computer Engineering

Written under the direction of

Predrag Spasojevic

And approved by

_____

_____

_____

_____

New Brunswick, New Jersey

Oct, 2020

ABSTRACT OF THE DISSERTATION

On the Efficiency of Retransmission Schemes for the Open Area Mm-wave Device-to-Device Environment

By SWAPNIL MHASKE

Dissertation Director:

Predrag Spasojevic

One of the differentiating characteristics of the next generation of wireless networks is its operation in the mm-wave bands. Technology developers aim to accomplish data rates of up to ten gigabits per second with an overall latency of less than 1 ms by leveraging the abundant bandwidth in the mm-wave spectrum. However, relative to the spectrum in use today, this comes with two major challenges. Firstly, mm-wave signals suffer from a greater propagation loss. This can be addressed by beamforming to provide directional gains. Secondly, mm-waves are susceptible to penetration loss due to the presence of buildings, vehicles, foliage, or humans in the environment. Such a loss in the signal quality due to environmental objects is collectively referred to as the *blockage* effect. Link outage due to the blockage effect can impact several mechanisms such as beam setup, beamtracking, modulation, and coding. Restoring the link quality may become prohibitively expensive in such scenarios, especially for the 5G NR use cases requiring sub-millisecond latency.

Communication in the mm-wave spectrum amidst blockages raises the question: Is a line-of-sight (LOS) connection between the transmitter and the receiver possible? To investigate and study the mm-wave channel, we implement the spatial channel model (SCM) specified by 3GPP for 5G new radio (NR). Mm-wave cluster propagation mechanism motivated the analysis of the impact of practical issues such as beam misalignment in the

presence of blockages. Further, we leverage the blockage modeling procedures specified to derive an approximate empirical model for the probability of LOS in the outdoor Urban Microcell-Street Canyon (UMi-SC) scenario. However, obtaining the LOS probability alone is not sufficient to model the small scale fading characteristics of the channel. To model small scale fading in a tractable manner, we provide a stochastic blockage model that not only gives the probability of LOS but also gives the approximate average signal attenuation as a soft metric that quantifies the extent of the blockage.

To model the blockage effect, we utilize the 2D homogeneous Poisson Point Process inside a circular spatial geometry. Blocker presence in a circular geometry can be directly applied to an environment where blockers are randomly placed around the receiver in all directions. Such an environment is commonly found in application scenarios that fall under the 3GPP use cases of massive Machine Type Communication (mMTC) and direct device-to-device (D2D) communication for 5G NR. Examples are public safety networks, warehouse and industrial robotics, wearable technology, and tactical networks. Due to the scalable nature of the circular geometry, our approach also lends itself to the modeling of reflections in the environment of operation. The loss due to a blocker is approximated using a double knife edge diffraction (DKED) method. The accuracy of the approximate and tractable analytical model is confirmed with the help of Monte Carlo simulations for real-world blocker placement in the environment.

The model is applied to analyze the impact of blockages on two Hybrid Automatic Repeat reQuest (HARQ) retransmission schemes, namely, Chase combining (CC) and Incremental Redundancy (IR). A trade-off between the beamforming accuracy (expressed in terms of beam misalignment) and the efficiency (expressed in terms of throughput) is presented. Thus providing insight into the choice of beamwidth as a function of the blockage effect for the environment in which the system is deployed.

Acknowledgements

To say that I am grateful for having Prof. Predrag Spasojevic as an advisor would be an understatement. I cannot thank him enough for his time and effort. Paying attention to detail and effectively communicating one's research are few of the many things that I could not have learned without him. His guidance, support, and encouragement went beyond academics. I will forever be indebted for his understanding and patience, especially in difficult times of my stay at Rutgers.

To the committee members, Prof. Emina Soljanin, Prof. Bo Yuan, and Dr. Ahsan Aziz, I am extremely thankful for your valuable time and advice. I could not have found a better committee for my dissertation. As an international graduate student and a teaching assistant, I would also like to thank Prof. Zoran Gajic and Prof. Yinying Chen for being an amazing graduate director. The value of their support for navigating through the complex web of administrative procedures cannot be overestimated.

Special thanks to Dr. Ahsan Aziz, Dr. Tai Ly, and Dr. Hojin Kee and the entire team at NI for the opportunity to work on exciting projects and for making my summer internships a truly rewarding experience.

I would like to express my gratitude to NI and the Department of Electrical and Computer Engineering at Rutgers University for their continual support to this work.

Many thanks to my colleagues and friends who made my experience at Rutgers a pleasant one. I have learned so much from you. Thanks to the LaTeX community online for providing quality software for ease of documentation.

This long and arduous journey would not have been possible without the unconditional love and motivation of my parents. I am very fortunate to have my sister Swati and my brother-in-law Ajay, for they have given me a home away from home. I cannot begin to describe in words the value of the encouragement and protection they've provided over the course of my study. I am thankful for my loving wife, Sneha. Her care and personal support has helped me get through stressful times during this journey.

Dedication

To my mother.

Nothing in this existence can fill the void in my heart. Wish you stayed longer.

&

To my father.

Your strength and sacrifice kept me going.

Table of Contents

List of Tables

List of Figures

Chapter 1

Introduction

A significant portion of the 5^{th} generation of wireless networks will operate in the mm-wave bands. One of the several challenges associated with mm-wave propagation is to overcome shadowing due to signal blockage caused by environmental objects. Particularly susceptible are nodes in a device-to-device network that typically operate at low power and in a blockage prone environment such as crowded open areas. Link outage due to the blockage effect can impact several mechanisms such as beam setup, beamtracking, adaptive modulation, and coding [1]. To see this, let us take a look into the functioning of beam management in 5G NR.

Factors such as the environment of deployment of the radio systems, the hardware capability in terms of the number of antennas on the equipment, the time budget (latency restrictions) of the application, and the carrier frequency range (FR) ($< 6\,\text{GHz}$ for *FR1* and $> 6\,\text{GHz}$ for *FR2*) dictate the beam operation procedures in 5G NR. Beamforming in is supported in both uplink (UL) and downlink (DL) [3]. Each of the physical data and control channels namely, the physical uplink shared channel (PUSCH), the physical uplink control channel (PUCCH), the physical downlink shared channel (PDSCH), and the physical downlink control channel (PDCCH) can have a requirement-specific beam. For instance, during the initial acquisition process wider beams can be used on the PDCCH and the PUCCH. Whereas, finer beams with higher gain can be used for data transfer on the PDSCH and PUSCH.

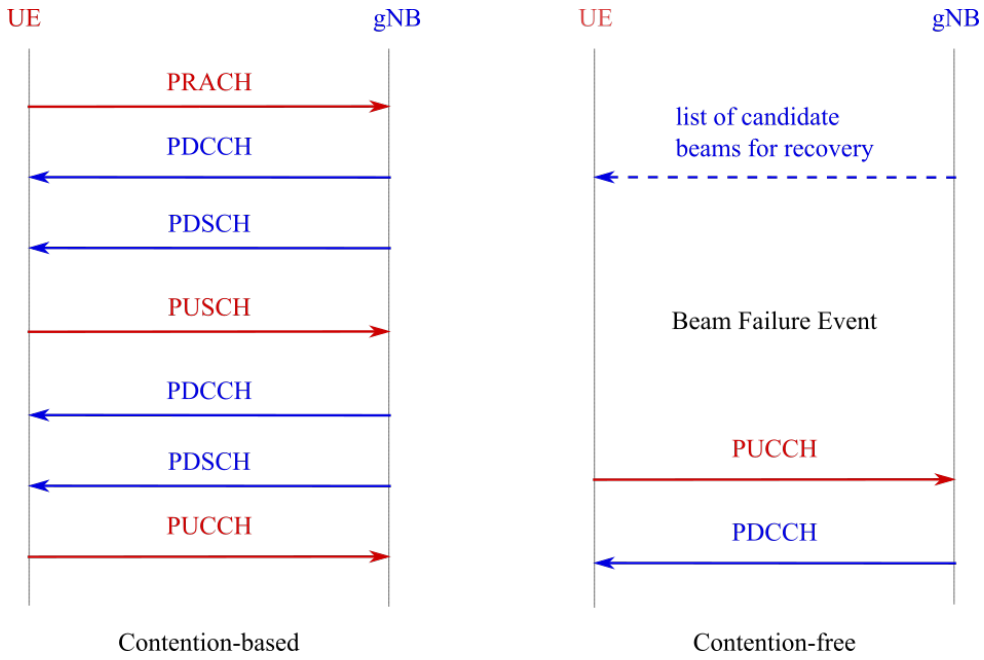

Figure 1.1: Simplified view of a typical UL/DL message exchange in the 5G NR RACH procedure.

In the event of shadowing due to environmental obstacles, the 5G NR UE handles beam failure at the PHY and MAC layer [4], [5]. This is to reduce the latency to recover from the failure as higher layers are not involved. The onus of detecting the failure is on the UE. It does so by evaluating the received signal quality measured by the block error-rate (BLER) on the specified PDCCH occasions. Once this value drops below a threshold, the PHY layer indicates the failure to the MAC layer. Depending on a radio resource control (RRC) configuration termed as *BeamFailureRecoveryConfig*, the MAC layer declares a beam failure only if a specified number of failures are indicated by the PHY layer within sufficiently quick successions of each other. Upon confirmation of beam failure, the UE begins recovery by initiating the random access procedure (RACH). 5G NR specifies two types of RACH procedures, contention-based (CB) which involves more steps - thus longer - and contention-free (CF) which is a shorter and hence a faster procedure. Fig. 1.1 shows

a simplified view of the exchange of UL and DL messages that typically takes place for the two RACH procedures. The reduced number of steps in the CF RACH procedure is due to the provision of dedicated physical RACH (PRACH) resources by the gNB to the UE in advance, in the event that a beam failure occurs. From a practical viewpoint it is clear that, it may take anywhere from a fraction of a millisecond to several milliseconds for the PHY-MAC beam recovery process to complete.

Since environmental obstacles can severely affect the quality of service, modeling blockages is a crucial step in the design of mm-wave communication systems. From a broader perspective, studies to model blockages can be based on real world measurements (e.g. [6]), ray tracing simulations (e.g. [7]), and stochastic methods (applied in this work). Recent notable works that have developed stochastic models for blocker placement in the environment of operation are [8], [9]. In [8], authors use random shape theory to model the effect of randomly placed blockers in the environment. The line-of-sight (LOS) probability is derived and it is concluded that, by increasing the base station density the adverse effects of blockages can be alleviated. A detailed and insightful model for randomly distributed human presence around the receiver is provided in [9]. Authors propose a tractable model for human blockage and show that the blockage probability increases with the blocker population density and with the transmitter-receiver distance.

The presence of blockers around the receiver directly depends on the spatial geometry of the environment. For instance, human blockers may be found at random locations in a park. Whereas in the case of modeling blockages due to a street, humans are restricted to the sidewalk. It is not hard to see that a generic blockage model that can be applied to any environment is unrealizable. In this analysis, we focus on a scenario where blockers are randomly placed around the receiver in an *open area* [1] environment. Such an environment is commonly found in application scenarios that fall under the 3GPP use case of massive Machine Type Communication (mMTC) [10] and direct device-to-device (D2D)

communication [11], [12], [13] envisioned for 5G. Examples of such deployments are public safety networks (for LTE [14]), warehouse and industrial robotics, wearable technology, and tactical networks.

While most work in the area of modeling blockages focuses on determining the probability of LOS, we obtain a soft metric for the signal attenuation in the presence of blockages. We derive a tractable analytical upper bound on the signal attenuation due to blockages as a function of model parameters, namely, the spatial geometry, the blocker population, and the penetration loss due to the blocker. To obtain this we leverage a simple stochastic geometry process: the two-dimensional homogeneous Poisson Point Process (PPP). The probability of link failure is derived based on the blockage model to provide modulation and coding design insights for operation in typical deployment scenarios.

The dissertation is organized as follows. The stochastic blockage model is described in Chapter 2. Chapter 4 gives an overview of the spatial channel model generation procedure specified for 5G NR. Along with the overview it also comments on the conclusion reached by investigating the results for the Urban Microcell-Street Canyon (UMi-SC) scenario. The extension of this work to provide an empirical model for the probability of blockage for the UMi-SC scenario is the subject of Chapter 5. A brief overview of our previous work on high-throughput FPGA architecture is provided in Appendix F. Conclusion of this segment of the work and potential future directions is presented in Chapter 6.

Throughout the dissertation, random variables are denoted by upper case letters and the corresponding realizations are denoted by their lower case counterparts. $P_B(b)$ denotes the probability mass function (PMF) of the discrete random variable B. The cumulative distribution function (CDF) and the probability distribution function (PDF) of the continuous random variable X is denoted by $F_X(x)$ and $f_X(x)$, respectively. $\mathcal{LN}(\mu, \sigma^2)$ denotes the lognormal distribution with μ and σ as the logarithmic mean and standard deviation. $\mathcal{NG}(\nu, \Sigma)$ denotes the Nakagami distribution with the fading parameter ν and the average

power Σ. $\mathcal{G}(\alpha, \beta)$ denotes the gamma distribution with the shape parameter α and the scale parameter β. $\mathcal{U}(a, b)$ denotes the uniform distribution over the interval $[a, b]$. $\phi(\cdot)$ denotes the PDF of the standard normal distribution, and $\Phi(\cdot)$ denotes its CDF. $\Gamma(\cdot)$ and $\gamma(\cdot, \cdot)$ denote the gamma function and the lower incomplete gamma function, respectively. $\mathbb{E}(\cdot)$ and $\mathbb{V}(\cdot)$ is the expectation and the variance operator, respectively.

Chapter 2

A Stochastic Blockage Model for the Open Area Mm-wave Environment

The presence of environmental obstacles that have the potential to shadow a mm-wave link is primarily dependent on the geometry of the environment surrounding the link. For example, these obstacles could be restricted to particular regions of the environment such as vehicles on a street or pedestrians on the sidewalk. In such environments, blockers may not be randomly spread around the link but may impact the link from one or more directions. An example of such a setup is the subject of Chapter 5. It may not be practicable to model blocker presence that could work for all types of environments. Nevertheless, modeling of blockers around the receiver or a transmitter of the link in a random fashion lends itself to several applications. For example device-to-device (D2D) communication by humans in parks, open malls, and atria or robotic communication inside an industrial warehouse. This type of an environment is defined as a scenario of interest in the 3GPP specification [1] as *D2D Access in Open Area*. Note that, we do not assume either the receiver or the transmitter to be at a vantage point with respect to potential blockers such as that on a rooftop. Similar application scenarios fall under the 3GPP use case of mMTC [10] and direct D2D communication [11], [12], [13].

In this chapter we present a stochastic blockage model for the D2D open area deployment use cases. We choose the stochastic approach as it relatively easily lends itself to a larger parameter space i.e. an ensemble of environmental instances. For instance, the size

of the obstacles can be varied to observe the impact of blockages without requiring significant changes to the assumed geometry. This is relative to a deterministic ray-tracing type method that imposes restrictions on the parameters as it relies on modeling as closely as possible a specific instance of the physical environment. We derive a tractable analytical upper bound on the signal attenuation due to blockages as a function of model parameters, namely, the spatial geometry, the blocker population, and the penetration loss of the blocker. To obtain this we leverage a simple stochastic geometry process: the two-dimensional homogeneous Poisson Point Process (PPP).

This chapter is organized as follows. The spatial setup for modeling the blockage effect is described in Section 2.1. Derivation of the soft measure: the expected attenuation due to blockages is provided in Section 2.2. In Section 3.2, the theoretical and simulated performance is presented.

2.1 Spatial Setup

To gauge the impact of blockage on a mm-wave link, we consider the open area D2D environment. An illustrative scenario that is typically found at town squares, transportation terminals, shopping malls, and parks, is shown in Fig. 2.1.

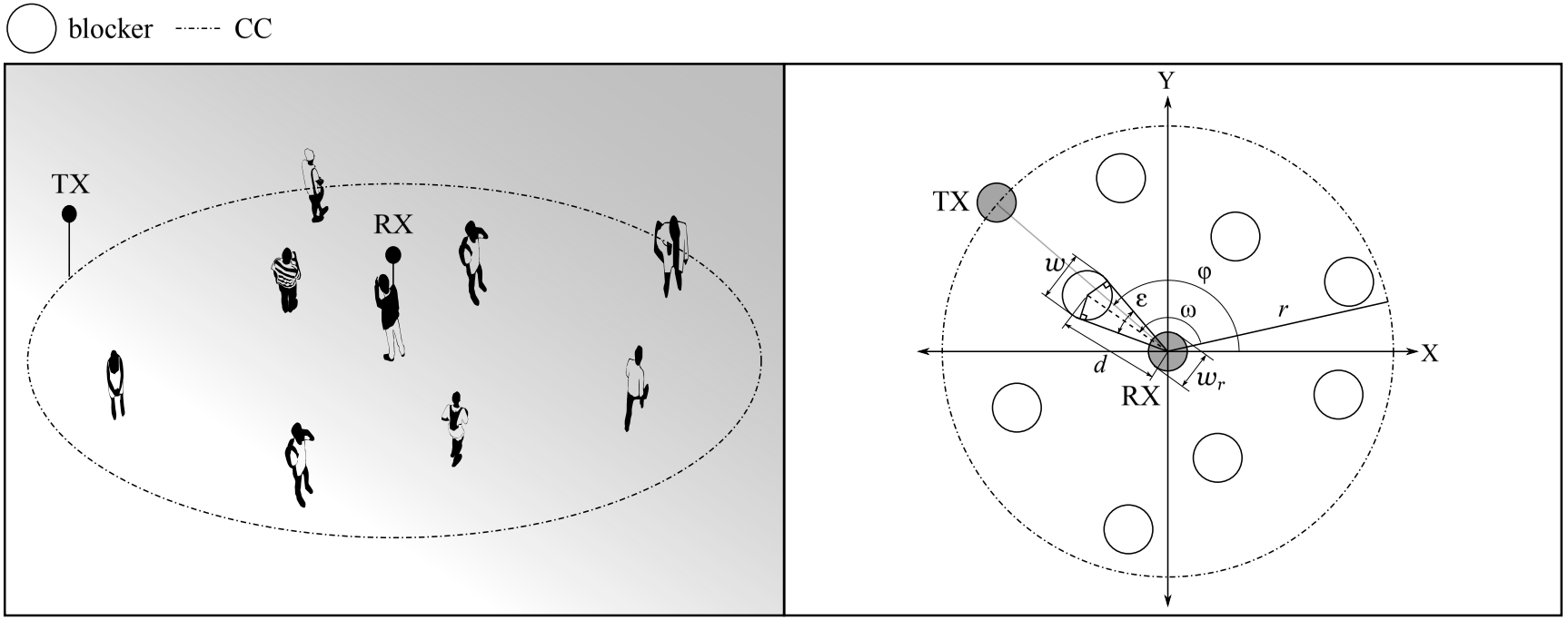

Figure 2.1: (Left) An example D2D scenario where the receiver (human with a mobile phone) associated with a transmitter (kiosk, sensor, or another mobile phone) is surrounded by human blockers. (Right) Azimuth plane geometry of the scenario on the left. Cylindrical blockers are randomly found inside the communication circle (CC) around the receiver which is located at the center of the CC. The receiver is blocked by a blocker along the direction ϕ.

Assumption 1 (Single User Downlink)**.** The 5G radio access network (RAN) will support time division duplexing (TDD) [15], [16]. Thus, for our analysis we focus on the signal reception for a receiver in a single user downlink scenario.

Assumption 2. The size of the geometry under consideration is defined by the communication range of the receiver. This can be expressed by a circle of radius r referred to as the communication circle (CC). As shown in Fig. 2.1 (right) the receiver is at the center of the CC and the transmitter at its edge.

To model the blockage effect we consider only those objects in the environment that can block the received signal in any direction. Such objects are termed as *blockers*. Note that once the receiver is blocked in an arbitrary direction, it is assumed that it is fully blocked in the zenith. Thus, the height of the blocker is not modeled in the analysis that follows. We model blockers as cylinders [17], [18] of diameter w. Let w_r denote the diameter of the cylindrical receiver and $s \geq \frac{w+w_r}{2}$ denote the distance of the nearest blocker from the receiver. The location of a blocker is defined by the polar coordinates $(d, \omega) \in [s, r] \times (0, 2\pi]$. From [19] we know that for a homogeneous PPP inside the annular region $[s, r] \times (0, 2\pi]$,

$$F_{D|R}(d \mid r) = \frac{d^2 - s^2}{r^2 - s^2} \quad d \in [s, r] \tag{2.1}$$

and $\Omega \sim \mathcal{U}(0, 2\pi)$. The location of blockers in the environment is modeled by placing the blockers inside the CC around the receiver as per a two-dimensional homogeneous PPP [20], [19]. Whereas the blocker population is modeled with the intensity of the PPP ρ which is the expected number of blockers per unit area.

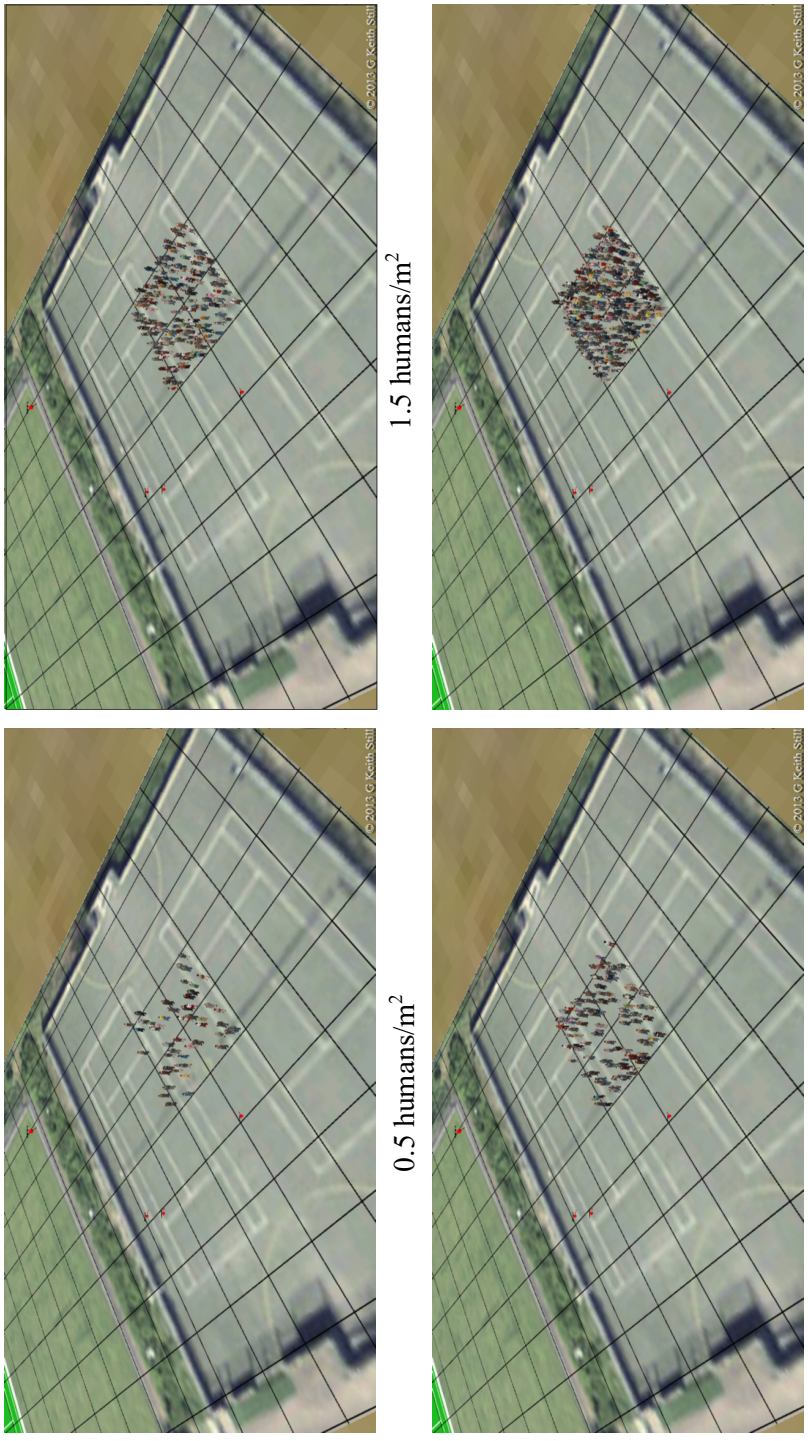

Figure 2.2: Crowd density visualization. Courtesy of Prof. G Keith Still, www.gkstill.com

An example visualizing blocker population density is depicted in Fig. 2.2. Thus, the average number of blockers within the CC is $\overline{\rho}(r) = \rho \times \pi r^2$. Also, the probability of having $M = m$ blockers around the receiver inside the CC is

$$P_{M|R}(m \mid r) = \frac{\overline{\rho}^m(r)}{m!} e^{-\overline{\rho}(r)}, \quad m = 0, 1, \ldots, \infty \tag{2.2}$$

2.2 Attenuation due to Blockages

The extent to which a mm-wave signal is blocked largely depends on the penetration loss of the blocker material. For example, tinted glass can cause a penetration loss of 10.55 dB per cm [21]. However, diffraction around the edges of the blocker may aid in reducing the loss due to the blockage. Note that, even if diffraction is reduced at mm-wave frequencies, introducing this improves the accuracy of modeling the loss due to blockages. A popular method to measure such diffraction around the edges is using the knife-edge diffraction (KED) model. KED-based methods to model the loss due to blockages have also been specified in standards such as ITU-R [22] and METIS [23]. An example of such a model is [6] where, the loss due to human blockage measured at 73 GHz ranges from 20 dB to 40 dB. In this work we model the attenuation due to a blocker as per the double knife-edge diffraction (DKED) model specified in the ITU-R standard. In the following we derive a closed form expression for the approximate average attenuation along a given direction.

We begin by analyzing the extent of blockage caused by a single blocker. From the geometry shown in Fig. 2.3 a blocker subtends angle $E = 2\arcsin(w/2D)$ as seen by the receiver at a distance D. This leads us to the following lemma.

Lemma 1. *For* $2\arcsin(w/2r) \leq \varepsilon \leq 2\arcsin(w/2s)$,

$$f_{E|R}(\varepsilon \mid r) = \frac{w^2}{4(r^2 - s^2)} \frac{\cos(\varepsilon/2)}{\sin^3(\varepsilon/2)}. \tag{2.3}$$

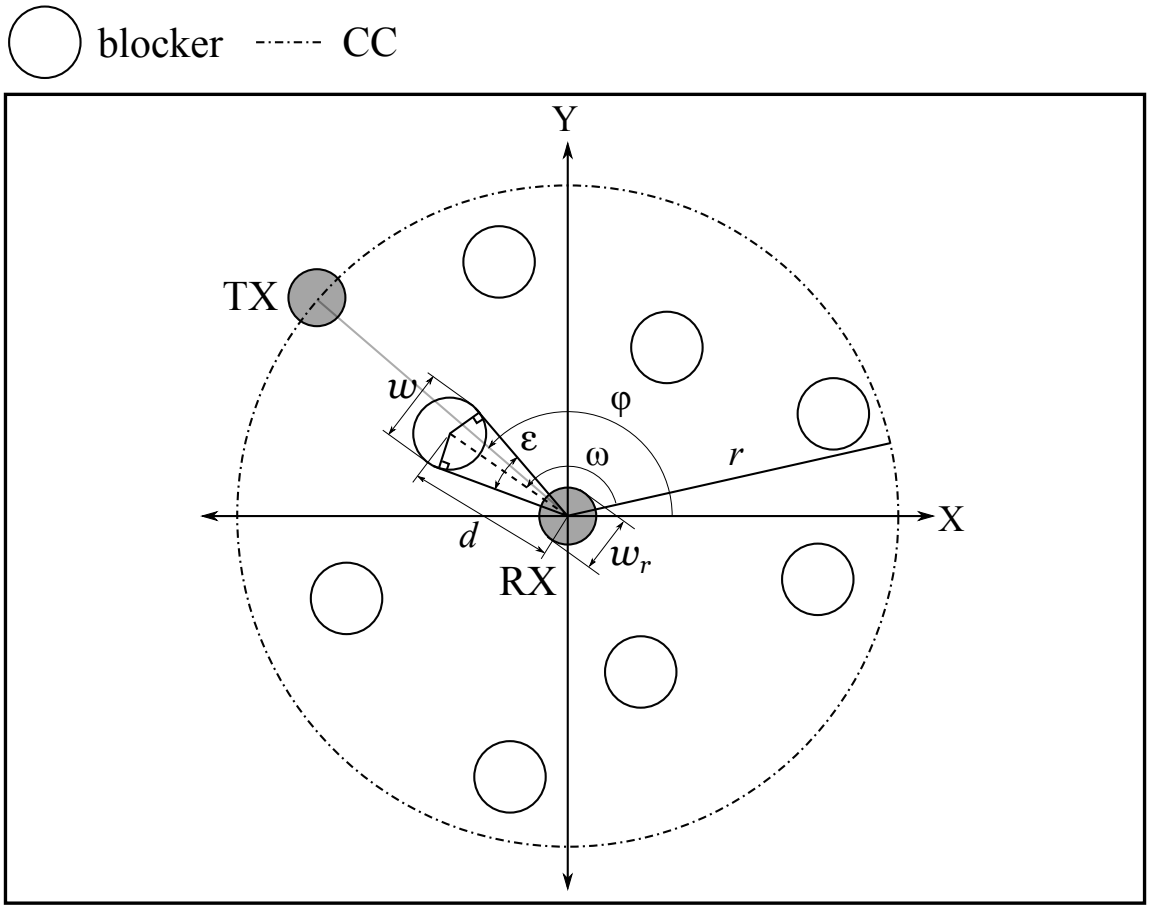

Figure 2.3: Azimuth plane geometry of the assumed scenario. Cylindrical blockers are randomly found inside the communication circle (CC) around the receiver which is located at the center of the CC. The receiver is blocked by a blocker along the direction ϕ.

Proof. Since $E = 2\arcsin(\frac{w}{2D})$,

$$\begin{aligned} F_{E|R}(\varepsilon \mid r) &= \Pr\left\{2\arcsin\left(\frac{w}{2D}\right) \le \varepsilon \;\middle|\; R \le r\right\} \\ &= 1 - F_{D|R}\left(\frac{w}{2\tan(\varepsilon/2)} \;\middle|\; r\right) \\ &\overset{(a)}{=} 1 - \frac{(w/2 \cdot s \cdot \sin(\varepsilon/2))^2 - 1}{(r/s)^2 - 1} \end{aligned}$$

where, in (a) we used (2.1) and the above holds when $2\arcsin(w/2r) \le \varepsilon \le 2\arcsin(w/2s)$. Differentiating with respect to ε proves the lemma. □

Definition 1 (Cover)**.** The receiver is said to have a cover in the direction $\phi \in (0, 2\pi]$ if there exists a blocker located at (d, ω) such that $\omega - \varepsilon/2 \le \phi \le \omega + \varepsilon/2$, where $\varepsilon = 2\arcsin(w/2d)$.

2.2.1 Probability of a Blockage

Consider that a blocker is located at (d, ω) in the CC of radius r. The probability that it blocks the received signal arriving from the direction ϕ is given by

$$\begin{aligned} h(r, \varepsilon) &= \Pr\{\Omega - E/2 \le \phi \le \Omega + E/2 \mid E = \varepsilon\} \\ &\overset{(a)}{=} \Pr\{-E/2 \le \Omega \le E/2 \mid E = \varepsilon\} \\ &= F_\Omega(\varepsilon/2) - F_\Omega(-\varepsilon/2) \\ &\overset{(b)}{=} \varepsilon/2\pi \end{aligned} \tag{2.4}$$

where, in (a) we have assumed $\phi = 0^\circ$ since, the event $\{\Omega - E/2 \le \phi \le \Omega + E/2\}$ is independent of ϕ. Also, in (b) we have used the fact that $\Omega \sim \mathcal{U}(0, 2\pi)$. Let $k_r := w/2r$ and $k_s := w/2s$. Then, the overall probability of a blocker in the CC of radius r causing a

cover along an arbitrary direction is

$$\begin{aligned} g(r) &= \int_{2\arcsin(k_r)}^{2\arcsin(k_s)} h(r,\varepsilon) f_{E|R}(\varepsilon \mid r)\,\mathrm{d}\varepsilon \\ &\overset{\text{(a)}}{=} \frac{1}{2\pi}\int_{2\arcsin(k_r)}^{2\arcsin(k_s)} \varepsilon f_{E|R}(\varepsilon \mid r)\,\mathrm{d}\varepsilon \\ &\overset{\text{(b)}}{=} \frac{w^2}{8\pi(r^2-s^2)}\left[\frac{2\arcsin(k_r)}{k_r^2} + 2\left(\frac{1}{k_r^2}-1\right)^{1/2}\right. \\ &\quad \left. -\frac{2\arcsin(k_s)}{k_s^2} - 2\left(\frac{1}{k_s^2}-1\right)^{1/2}\right]. \end{aligned} \tag{2.5}$$

where, in (a) we have used (2.4) and in (b) we have used (2.3). In the following theorem we provide the average attenuation caused to the received signal along ϕ due to multiple covers.

2.2.2 Expected Attenuation

Supposing that there are $M = m$ blockers in the CC, let $N = n \in [0, m]$ be the number of covers along the direction ϕ. Based on the fact that the blocker locations (D, Ω) are i.i.d. for all the m blockers we have,

$$P_{N|M,R}(n \mid m, r) = \binom{m}{n} g^n(r)\,[1-g(r)]^{m-n}\,. \tag{2.6}$$

Let $A(r)$ denote the attenuation of the received signal along ϕ. Then, $A(r) = \zeta^N(r)$ where, $\zeta(r)$ is the attenuation due to a blocker inside the CC of radius r. Based on the DKED model, from Appendix A,

$$\zeta(r) \approx \frac{1}{2a}\sqrt{\frac{\lambda}{w}}\left[1 + \frac{\pi}{2}\sqrt{\frac{r}{w}}\right]. \tag{2.7}$$

where, λ is the carrier wavelength in m and a is an approximation constant.

Theorem 1 (Expected Attenuation)**.** *Let the receiver be placed at the center of the CC of radius r. Let cylindrical blockers of diameter w be placed around the receiver according*

to a two-dimensional homogeneous PPP with a sufficiently large intensity ρ. Then, the expected attenuation of a received signal arriving from the direction $\phi \in (0, 2\pi]$ is given as

$$\overline{A}(r) := \mathbb{E}\left[A \mid R = r\right] \approx e^{-\overline{\rho}(r)\left(1-e^{-g(r)(1-\zeta(r))}\right)}$$

where, $\overline{\rho}(r) = \rho \times \pi r^2$ is the expected number of blockers inside the CC and $g(r)$ is the probability of a blocker causing a cover in the direction ϕ.

Proof. The expected attenuation due to m blockers inside the CC is given by,

$$\mathbb{E}\left[A \,\middle|\, M = m, R = r\right] = \sum_{n=0}^{m} P_{N|M,R}(n \mid m, r)\zeta^n(r). \tag{2.8}$$

Applying the law of total probability we get,

$$\begin{aligned}
\overline{A}(r) &= \sum_{m=0}^{\infty}\sum_{n=0}^{m} P_{N|M,R}(n \mid m, r)\zeta^n(r)P_{M|R}(m \mid r) \\
&\overset{\text{(b)}}{=} \sum_{m=0}^{\infty}\sum_{n=0}^{m} \binom{m}{n} g^n(r)\left(1-g(r)\right)^{m-n}\zeta^n(r)\frac{\overline{\rho}^m(r)}{m!}e^{-\overline{\rho}(r)} \\
&\overset{\text{(c)}}{\approx} \sum_{m=0}^{\infty}\sum_{n=0}^{m} \frac{\left(mg(r)\right)^n}{n!}e^{-mg(r)}\zeta^n(r)\frac{\overline{\rho}^m(r)}{m!}e^{-\overline{\rho}(r)} \\
&= \sum_{m=0}^{\infty} e^{-mg(r)}\sum_{n=0}^{m} \frac{\left(\zeta(r)mg(r)\right)^n}{n!}\frac{\overline{\rho}^m(r)}{m!}e^{-\overline{\rho}(r)} \\
&\overset{\text{(d)}}{\approx} \sum_{m=0}^{\infty} e^{-mg(r)(1-\zeta(r))}\frac{\overline{\rho}^m(r)}{m!}e^{-\overline{\rho}(r)} \\
&= \sum_{m=0}^{\infty} \frac{\left(\overline{\rho}(r)e^{-g(r)(1-\zeta(r))}\right)^m}{m!}e^{-\overline{\rho}(r)} \\
&= e^{\left(\overline{\rho}(r)e^{-g(r)(1-\zeta(r))}\right)}e^{-\overline{\rho}(r)} \\
&= e^{-\overline{\rho}(r)\left(1-e^{-g(r)(1-\zeta(r))}\right)}
\end{aligned} \tag{2.9}$$

where, in (b) we have used (2.2) and (2.6). In (c) we apply the Poisson limit theorem [24] assuming sufficiently large values of ρ (and consequently m) and sufficiently small values of $g(r)$ giving $\binom{m}{n}g^n(r)[1-g(r)]^{m-n} \approx \frac{[mg(r)]^n}{n!}e^{-mg(r)}$. In (d) as a consequence of

assuming sufficiently large values of m, we apply the Taylor series approximation to get $\sum_{n=0}^{m} \frac{[\zeta(r)mg(r)]^n}{n!} \approx e^{\zeta(r)mg(r)}$. □

2.3 Numerical Results and Discussion

Numerical results validating the blockage model are presented. Further, the effect of mobility on the intensity, duration, and frequency of blockages is evaluated.

2.3.1 Expected Attenuation

The expected attenuation model is validated by means of a 10^5 Monte Carlo simulation per blocker density (ρ) value. Fig. 2.4 shows the results for various blocker and circular geometry (CC) sizes. Figures 2.4a and 2.4b demonstrate the blockage effect for two carrier frequencies of 28 GHz and 76 GHz, respectively. Solid lines represent the theoretical result (Theorem 1) and dashed lines represent their simulated counterparts. In each simulation trial, blockers are dropped as per the 2D homogeneous PPP and the resulting cover around the receiver is calculated. To model realistic placement of blockers rejection sampling is used to ensure that no blocker overlaps another blocker.

The DKED-based attenuation $\zeta(r)$ ranges from 6.4 dB for $(w, r) = (0.35, 75)$ to 19.62 dB for $(w, r) = (1, 0.25)$ m (Fig. A.2 in Appendix A). Note that, from (2.7), attenuation numerically decreases faster with an increase in w than with an increase in r. It is observed that the theoretical approximation for the attenuation due to random blockages closely follows the simulation results. As expected, attenuation worsens as the blocker population increases. The geometry size r dominates the waterfall or slope of the attenuation. This is due to the quadratic dependence of attenuation on r. Moreover, for a fixed circular geometry size r, the attenuation worsens with an increase in the blocker size w. It is worthwhile to note that, the attenuation profile depends on the combination of the blocker

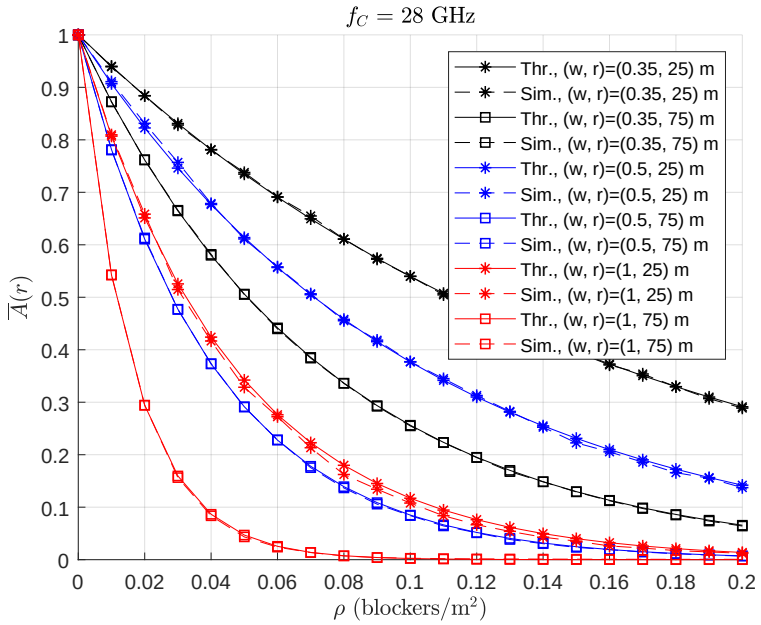

(a) 28 GHz

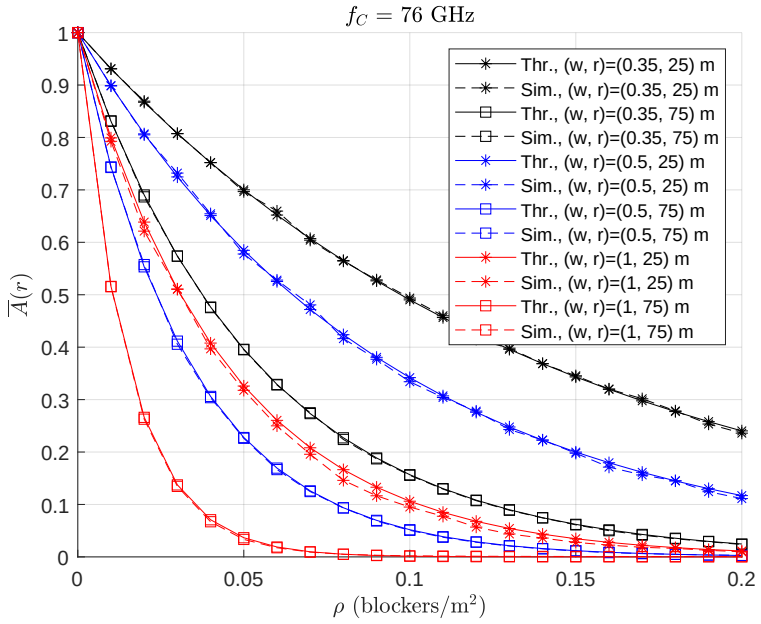

(b) 76 GHz

Figure 2.4: Theoretical and simulated attenuation due to blockages for various blocker sizes (w) and various circular geometry sizes (r).

size (w) and the CC size (r). This is evident from the cases of $(w, r) = (0.5, 75)$ m (relatively small blockers) and $(w, r) = (1, 25)$ m (relatively large blockers) as the two cases result in more or less similar attenuation values. This is inspite of the fact that $\zeta(r) = 19.62\,\text{dB}$ for $(w, r) = (1, 25)$ m and $\zeta(r) = 9.43\,\text{dB}$ for $(w, r) = (0.5, 75)$ m. The latter case results in a worse attenuation profile as the blocker population is much higher than that in the former case.

2.3.2 Effect of Blocker Mobility

In the above we evaluated the impact of blockages when the environmental blockers are stationary in the 2D space. To evaluate the dynamic nature of the attenuation due to moving blockers, we perform the following experiment.

Setup: Blockers are placed inside the circular geometry shown in Fig. 2.3 as per a 2D homogeneous PPP at time $t = 0$. All blockers are assumed to be moving at a velocity of v miles per hour (mph). An arbitrary blocker can move along any direction in a near-random fashion. This style of motion is chosen over a purely random walk to mimic practically observed movements such as that of humans walking or the motion of industrial machines. An example is shown in Fig. 2.5 where blockers are represented by circles. A change in color depicts a change in the blocker's position (time step $t = 0$ is shown in black). The instantaneous attenuation due to blockers is then computed for an arbitrary direction.

Fig. 2.6 and Fig. 2.7 show the results for a carrier frequency of 28 GHz, whereas, Fig. 2.8 shows them for 76 GHz. From all the cases, we can see that the attenuation level is dominated by the blocker size w. Whereas, the duration of the shadowing due to blockage(s) for an arbitrary direction mainly depends on the velocity of the blockers and their size. Moreover, as seen in Fig. 2.6b (relative to Fig. 2.6a) the frequency of blockage events increases as the blocker population density increases. This dependence is

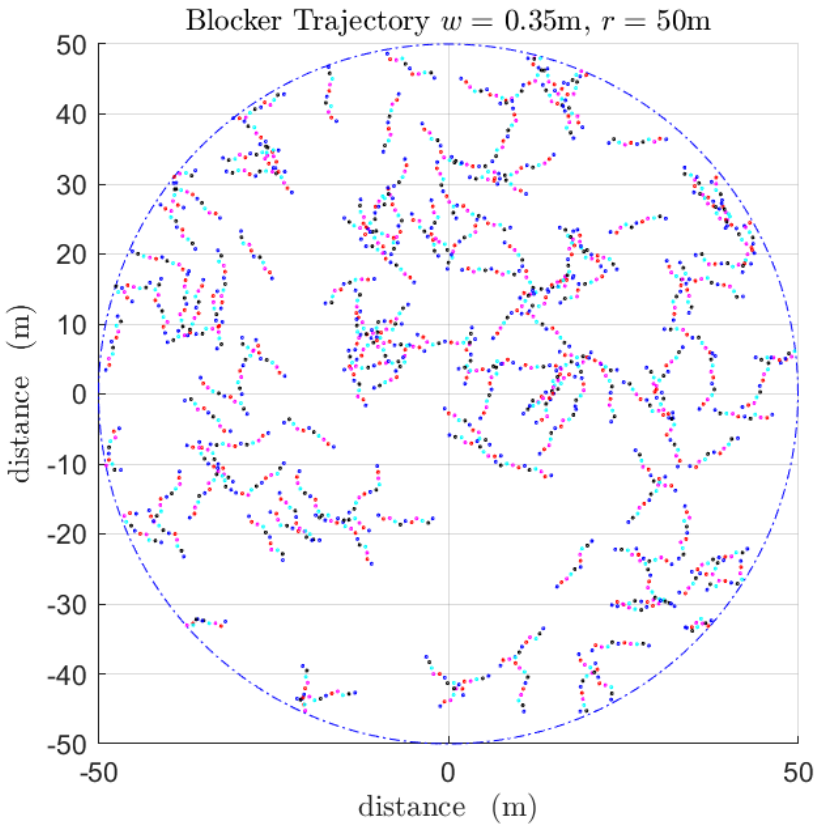

Figure 2.5: Schematic showing a sample set of blocker trajectories. Blockers are represented by circles. Blockers are moving at 20 mph for 1 s with a blocker population density of 0.02 blockers per square meter. A change in color depicts a change in the blocker's position (time step $t = 0$ is shown in black).

also observed in the case of the increased blocker velocity of 55 mph (Fig. 2.7) and in the case of the increased carrier frequency 76 GHz (Fig. 2.8). The results clearly show that upwards of 70 dB attenuation due to blockages lasting for tens or even hundreds of milliseconds is possible.

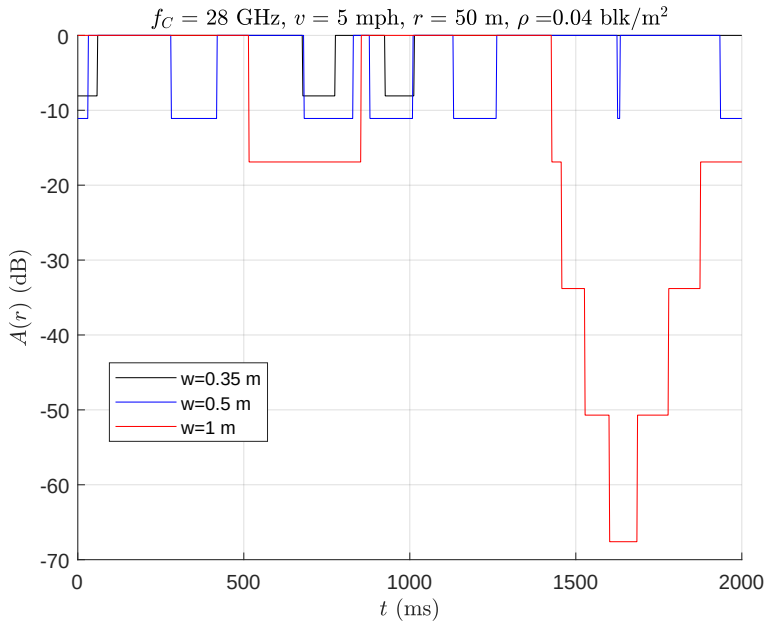

(a)

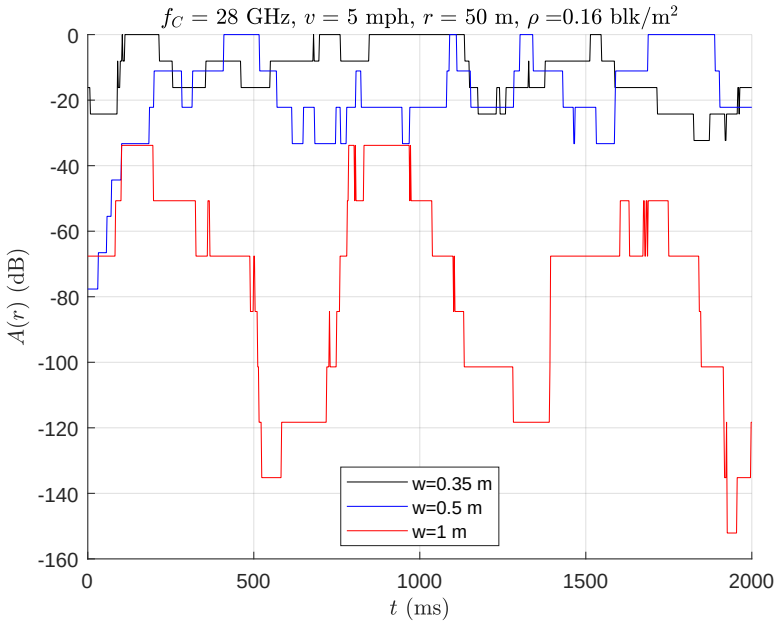

(b)

Figure 2.6: Blockage effect as a function of time at a carrier frequency of 28 GHz and a blocker velocity of 5 mph.

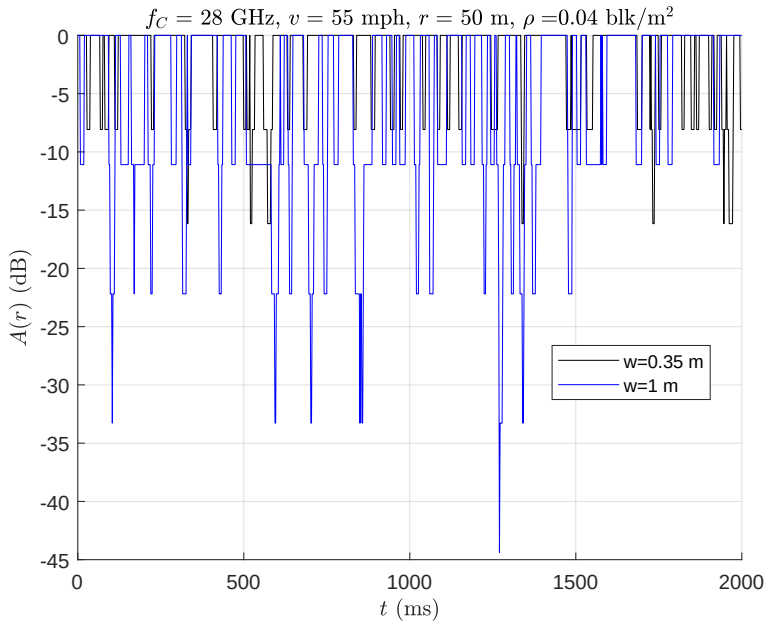

(a)

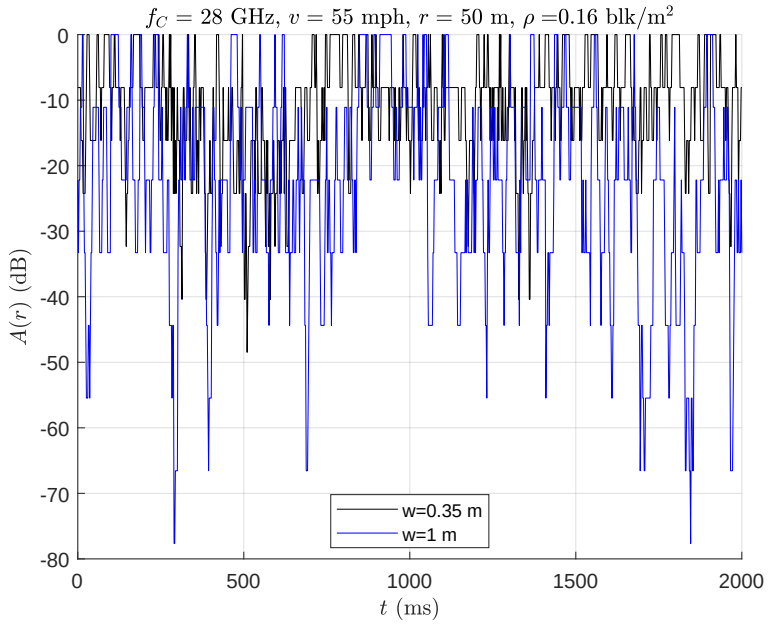

(b)

Figure 2.7: Blockage effect as a function of time at a carrier frequency of 28 GHz and a blocker velocity of 55 mph.

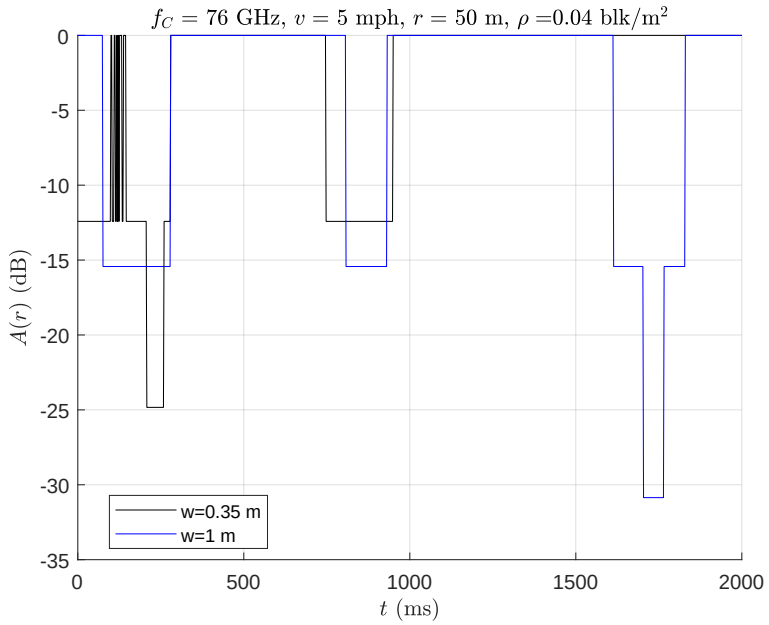

(a)

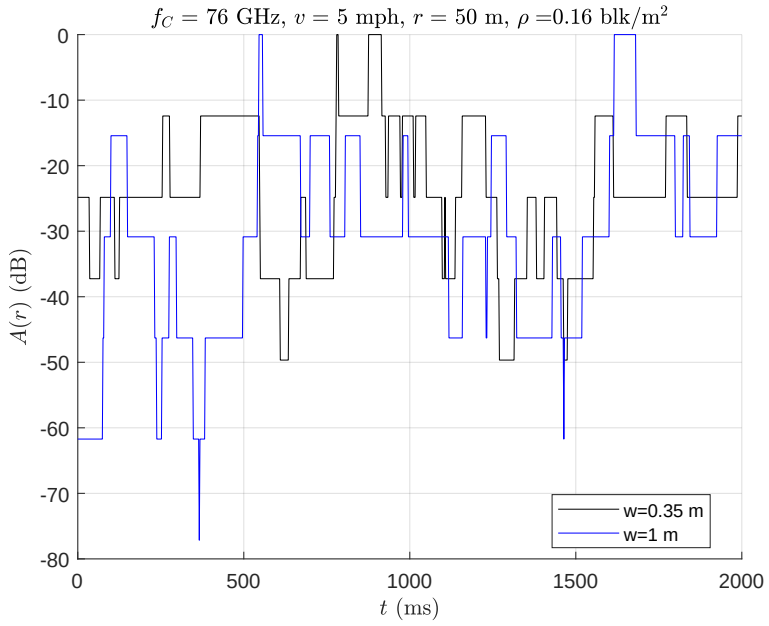

(b)

Figure 2.8: Blockage effect as a function of time at a carrier frequency of 76 GHz and a blocker velocity of 5 mph.

Chapter 3

Efficiency of Retransmission Schemes in 3GPP 5G NR

To begin the analysis we first discuss the system model considered for deriving the LOS and NLOS link SNR.

3.1 System Model

3.1.1 Receiver Architecture

The transmitter and the receiver are assumed to have a total of N_t and N_r antenna elements, respectively and is able to beamform simultaneously in $(L+1)$ azimuthal directions (hybrid beamforming capability). Further, we assume that the receiver is equipped with $L+1$ uniform linear arrays (ULA). The architecture of each branch of the receiver is as shown in Fig. 3.1. The transmitter is capable of beamforming in one direction at a time (analog beamforming capability). Having a simpler (in terms of hardware complexity) transmitter architecture applies to a large number of D2D network use cases. An example

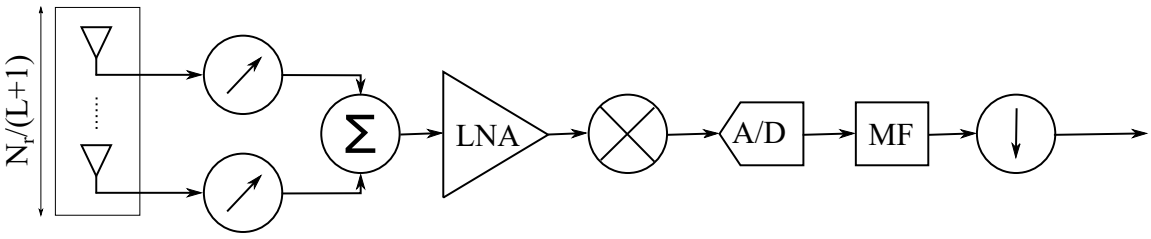

Figure 3.1: Receiver architecture of the ℓ^{th} link, $0 \leq \ell \leq L$. LNA: Low Noise Amplifier, A/D: Analog to Digital Conversion, MF: Matched Filter.

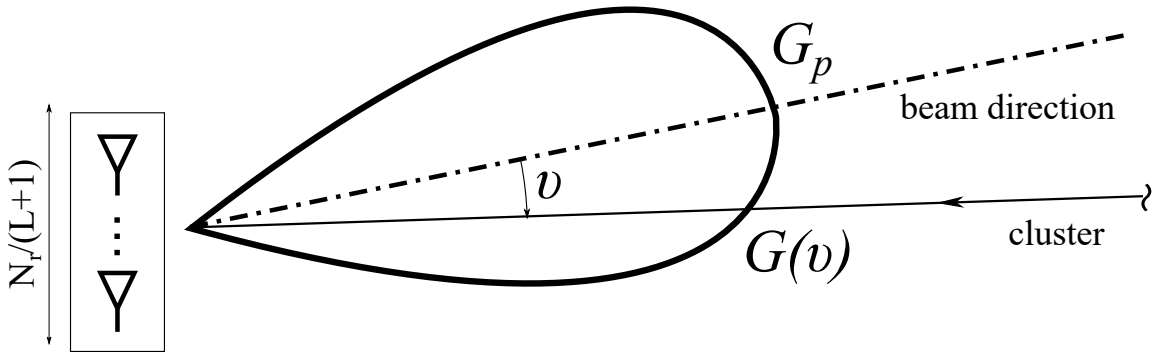

Figure 3.2: Schematic showing misalignment υ.

use case is the cost-efficient deployment of sensors transmit information such as location data to relatively advanced receivers.

Environmental objects considered in this work are composed of lossy dielectric materials (for example, humans or warehouse robots). Such objects will essentially absorb, propagate, and reflect the energy incident on their surface [25]. In this work, we assume mm-wave propagation in the form of clusters [21]. Thus, a cluster when incident on an object surrounding the link will be attenuated and reflected. As shown in Fig. 3.4, a link between the transmitter and the receiver is composed of one or more clusters that eventually reaches the receiver.

Definition 2 (Cluster)**.** The 3GPP SCM [1] assumes that a link can be resolved to rays propagating in the environment. A cluster as shown in Fig. 4.2 is defined as a group of rays that are closely propagating together in space.

3.1.2 Beam Gain Model

Practical beamforming methods are subject to error in terms of aligning the beam in the desired direction. One such issue is the angular offset between the beam direction and the cluster angle of arrival (AoA) also termed as beam misalignment. This is illustrated in

Fig. 3.2. This error can be caused during the initial stage of beamforming i.e. during the setup or after the beam has been established. This could be due to environmental factors such as obstacles in the beam or due to mobility. As a consequence, as shown in Fig. 3.2 the actual gain $G(\upsilon)$ may be lower than the (expected) peak gain G_p.

To quantify the effect of beam misalignment we assume that misalignment follows the model specified in the [26] specification. Here, the beam gain roll-off is modeled as a circularly symmetric Gaussian gain function. Applying this function to the azimuthal gain $G(\upsilon)$ we get,

$$G(\upsilon) = G_p e^{-\alpha \upsilon^2} \tag{3.1}$$

where, $\alpha = 4 \ln 2/\theta_{3dB}^2$. Here, θ_{3dB} denotes the half-power beamwidth. For a ULA with N antenna elements [27], $\theta_{3dB} \approx 101.5°/N$ and $G_p \approx N$ thus,

$$G(\upsilon) = N e^{-cN^2\upsilon^2} \tag{3.2}$$

where, $c = 4 \ln 2/101.5^2$. The beam gain as a function of misalignment is shown for various values of the number of antenna elements N is shown in Fig. 3.3. Note that, the beam gain denoted by G_ℓ in Section 3.1.4 is the effective beam gain after the misalignment model has been applied.

3.1.3 Spatial Setup

The retransmission scheme is assumed to operate on a beamformed mm-wave link as shown in Fig. 3.4. The transmitter-receiver pair is separated by a distance of r_{tr}. Blockers are placed around the link as per the 2D homogeneous PPP described in Section 2.1.

Assumption 3. In the analysis to follow, it is assumed that the receiver and the environmental objects surrounding it are of the same size i.e. $w_r = w$, implying that $s = w$.

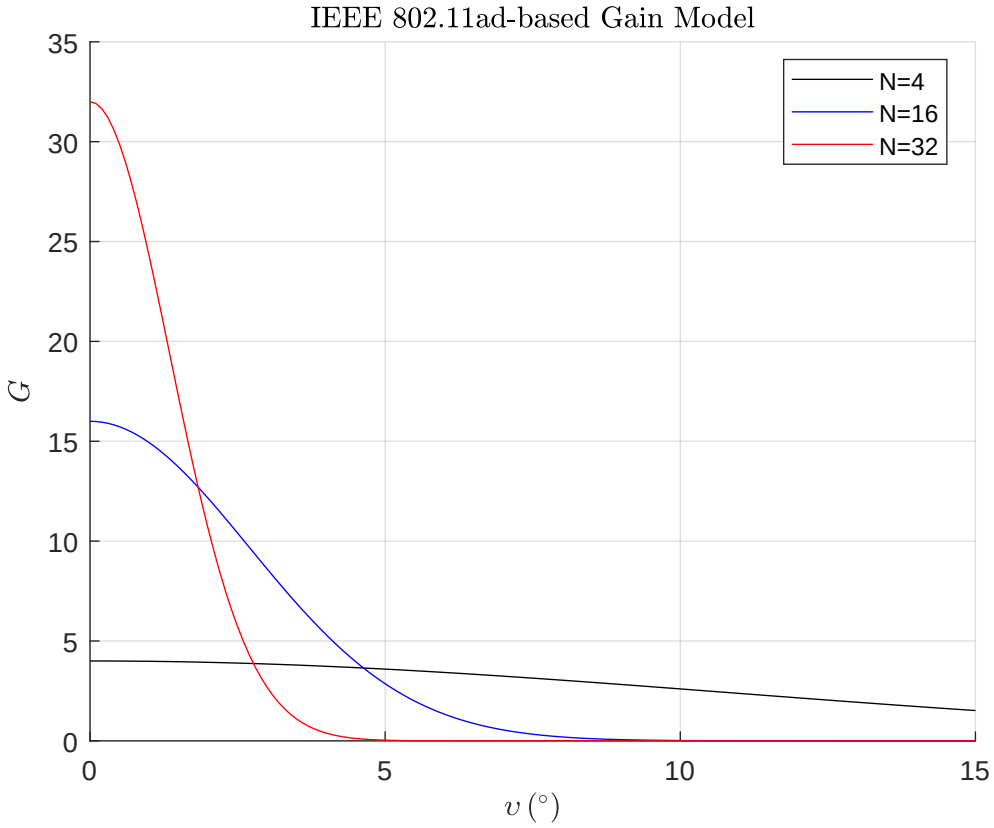

Figure 3.3: Beam gain as a function of misalignment v.

Here, we consider the finite rectangular region of area $W_X \times W_Y$ meters. Depending on the environment, this region may comprise of several subregions as shown in Fig. 3.4 (left). Each subregion is characterized by its blocker population intensity. Examples of subregions i.e. regions with the same blocker population density are shown in Fig. 3.4.

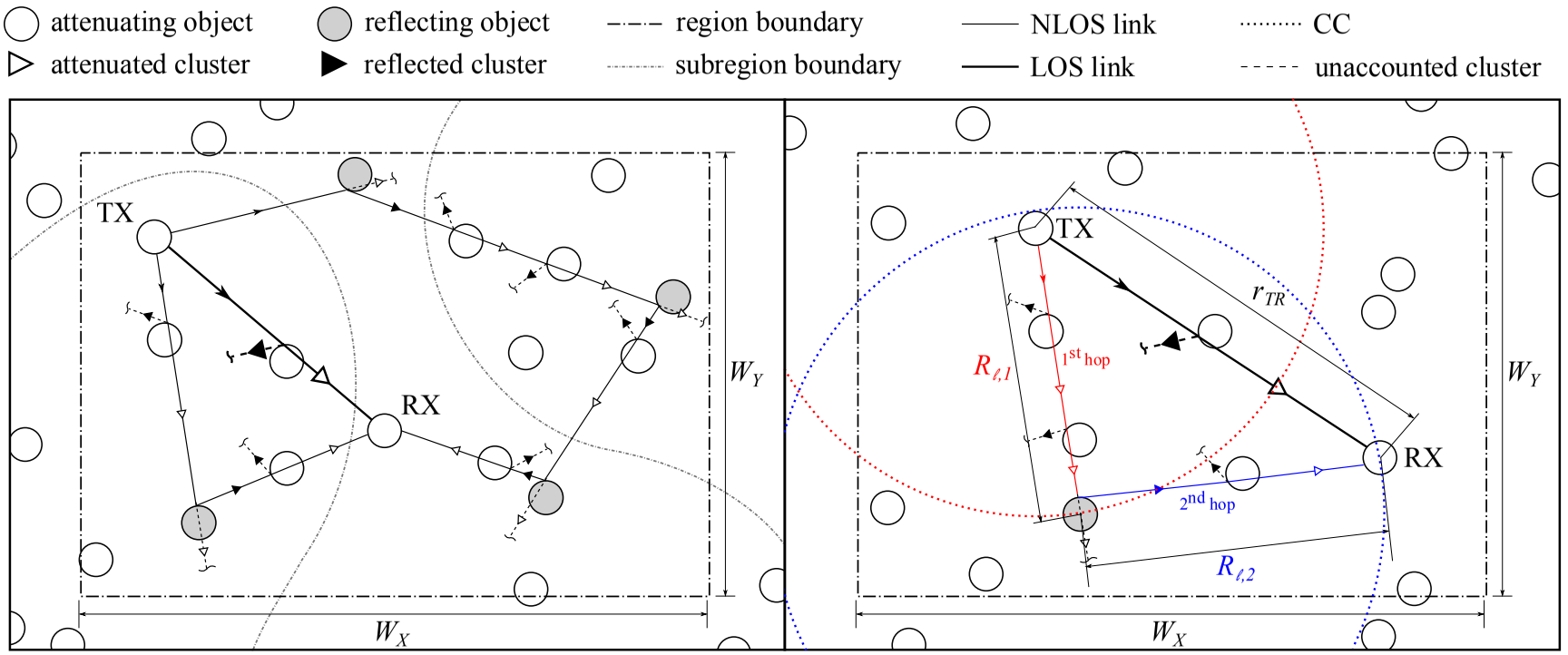

Figure 3.4: (Left) Overall system model assumed for the analysis. The case of $L = 2$ is shown. (Right) Illustration of the decomposition of a single link into hops. Also indicated is the rectangular region assumed to determine the hop length distribution (Appendix B).

In the following, the cluster arriving at the receiver without undergoing any reflection is termed as the LOS link. Whereas, a cluster arriving at the receiver after undergoing reflection is termed as the NLOS link. Owing to the receiver's capability of beamforming in $L+1$ directions, $L+1$ links (1 LOS and L NLOS) can be established between the transmitter and receiver. An example case with $L=2$ is depicted in Fig. 3.4 (left).

Assumption 4. Let q_ℓ denote the number of reflection that the ℓ^{th} link undergoes. Any link in the environment can undergo at most $q_m - 1$ reflections. Thus, $2 \leq q_\ell \leq q_m$. Let Q_ℓ denote a random variable whose realizations are q_ℓ. The number of hops along the ℓ^{th} link are uniformly distributed, thus giving the following.

$$P_{Q_\ell}(q_\ell) = \begin{cases} \frac{1}{q_m - 1} & 2 \leq q_\ell \leq q_m \\ 0 & \text{otherwise.} \end{cases} \tag{3.3}$$

Further, by definition, a NLOS link can be decomposed into *hops*. This is depicted in Fig. 3.4 (right) for the ℓ^{th} link, $1 \leq \ell \leq L$ that undergoes a $(q_\ell - 1)^{\text{th}}$ order reflection. Consequently, it is composed of q_ℓ hops.

Assumption 5. Let $R_{\ell,i}$ denote the length of the i^{th} hop of the ℓ^{th} link, $1 \leq i \leq Q_\ell$. Then by definition, $w < r_{\ell,i} \leq W_d$, where $W_d = \sqrt{W_X^2 + W_Y^2}$ is the length of the diagonal of the rectangular region under consideration. From Appendix B, the empirical distribution of $R_{\ell,i}$ is approximately shown to be the truncated Lognormal distribution. Thus, $R_{\ell,i} \sim \mathcal{LN}(\mu_R, \sigma_R^2)$ where, μ_R and δ_R are a function of the spatial geometry considered for the analysis and are provided in Appendix B.

Note 1. The blocker population intensity that an arbitrary link is subjected to is a function of the intensities of the subregions that the link traverses through. As shown in Fig. 3.5 the LOS link (in red) traverses through two subregions with intensities $\rho^{(1)}$ and $\rho^{(2)}$. In this analysis, we assume that this link is subjected to an *effective* blocker intensity of ρ_0. The determination of this effective intensity per link is beyond the scope of this work.

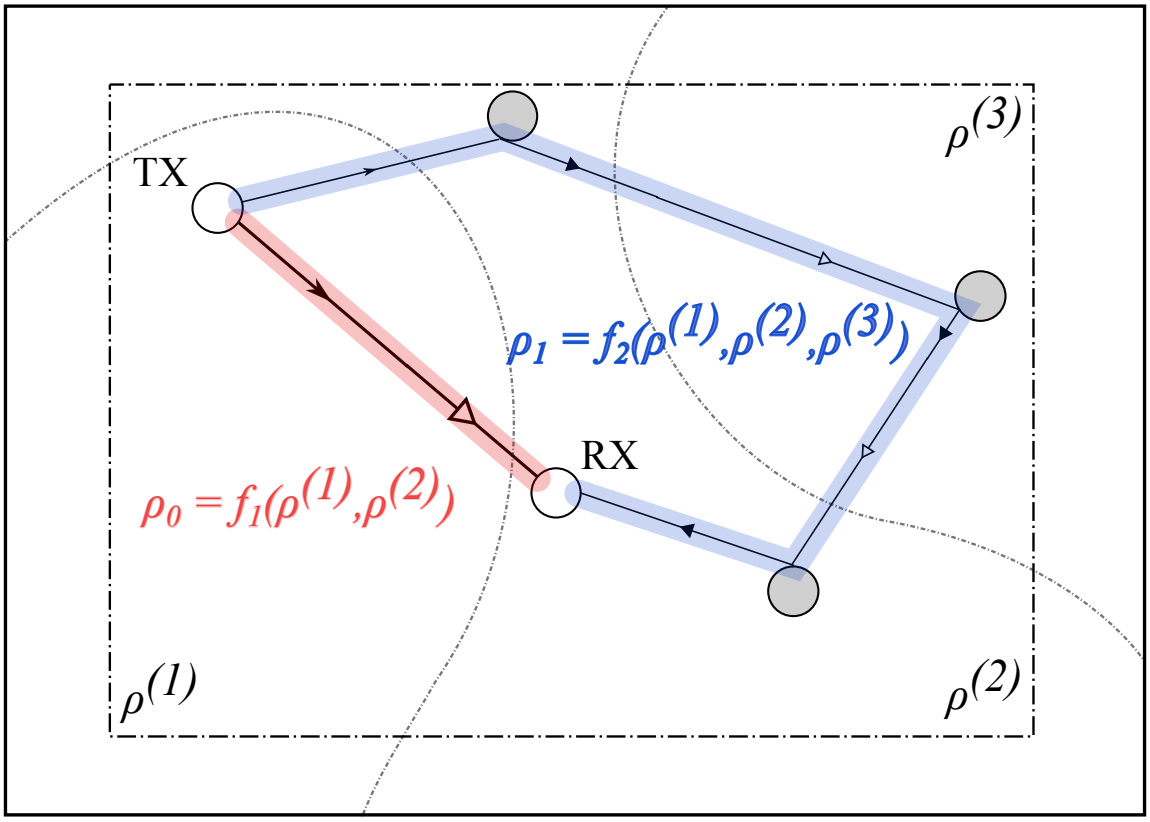

Figure 3.5: Example showing the blocker population intensity that a link is subjected to.

3.1.4 Link SNR

The capacity of the communication network under consideration is a function of the signal-to-noise ratio (SNR) on each link. In this section we derive the expression for the SNR on the LOS and NLOS links.

NLOS SNR

To formulate the attenuation due to blockages on a NLOS link, we first consider the attenuation on each hop of the link. The ℓ^{th} NLOS link that undergoes a $(q_\ell - 1)^{\text{th}}$ order reflection, can be decomposed into q_ℓ hops, $1 \leq \ell \leq L$. Let ρ_ℓ denote the effective blocker

intensity on the ℓ^{th} NLOS link (see Note 1). Let the random variable $R_{\ell,i}$ denote the length of the i^{th} hop of the ℓ^{th} link. Let $A(R_{\ell,i})$ denote the attenuation due to blockages on the i^{th} hop of the ℓ^{th} link. Note that, $A(R_{\ell,i})$ is a random variable whose realizations are $\overline{A}(r)$. Thus, from Theorem 1,

$$\begin{aligned} A(R_{\ell,i}) &= e^{-\overline{\rho}_\ell(R_{\ell,i})\left(1-e^{-g(R_{\ell,i})(1-\zeta(R_{\ell,i}))}\right)} \\ &= e^{-\rho_\ell \pi R_{\ell,i}^2\left(1-e^{-g(R_{\ell,i})(1-\zeta(R_{\ell,i}))}\right)} \end{aligned} \tag{3.4}$$

Since $g(R_{\ell,i})(1-\zeta(R_{\ell,i}))$ is sufficiently small, we have $1-e^{-g(R_{\ell,i})(1-\zeta(R_{\ell,i}))} \approx g(R_{\ell,i})(1-\zeta(R_{\ell,i}))$. From Appendix C, we have

$$\overline{A}(R_{\ell,i}) \approx e^{-\rho_\ell\left(c_1 R_{\ell,i}^{1/2}+c_2 R_{\ell,i}+b\right)} \tag{3.5}$$

where, $c_1 := \left(\frac{2+\sqrt{3}}{16}\right)\frac{\pi w\sqrt{\lambda}}{a}$, $c_2 := w - \frac{\sqrt{\lambda w}}{2a}$, and $b := \left(\frac{2+\sqrt{3}}{4}\right) w^{3/2}\left(\frac{\sqrt{\lambda}}{2a} - \sqrt{w}\right)$. Thus, the expected attenuation due to blockages on the ℓ^{th} NLOS link is given by

$$\begin{aligned} \overline{A}(Q_\ell) &= \prod_{i=1}^{Q_\ell} \overline{A}(R_{\ell,i}) \\ &\approx e^{-\rho_\ell\left\{c_1 \sum_{i=1}^{Q_\ell} R_{\ell,i}^{1/2}+c_2 R(Q_\ell)+bQ_\ell\right\}} \end{aligned} \tag{3.6}$$

where, $R(Q_\ell) := \sum_{i=1}^{Q_\ell} R_{\ell,i}$ is the length of the link with Q_ℓ hops. Let $H(Q_\ell)$ denote the path loss on the ℓ^{th} NLOS link with Q_ℓ hops. Then,

$$H(Q_\ell) = h_{fs}(r_0) r_0^{-\eta} R^\eta(Q_\ell) \tag{3.7}$$

where, η is the NLOS path loss coefficient and $h_{fs}(r_0) = 4\pi r_0/\lambda$ is the free space path loss at a reference distance of r_0 meters. Thus, the received power on the ℓ^{th} NLOS link with

Q_ℓ hops is given by

$$\begin{aligned} S(Q_\ell) &:= G_\ell \beta^{Q_\ell - 1} P_t \frac{\overline{A}(Q_\ell)}{H(Q_\ell)} \\ &\overset{(a)}{=} G_\ell \beta^{Q_\ell - 1} P_t \frac{e^{-\rho_\ell \left\{ c_1 \sum_{i=1}^{Q_\ell} R_{\ell,i}^{1/2} + c_2 R(Q_\ell) + b Q_\ell \right\}}}{h_{fs}(r_0) r_0^{-\eta} R^{\eta}(Q_\ell)} \\ &:= \frac{G_\ell \beta^{Q_\ell - 1} P_t}{h_{fs}(r_0) r_0^{-\eta}} e^{-\rho_\ell c_1 \sum_{i=1}^{Q_\ell} R_{\ell,i}^{1/2}} \times R^{-\eta}(Q_\ell) e^{-\rho_\ell [c_2 R(Q_\ell) + b Q_\ell]} \end{aligned}$$

where, in (a) we have substituted (3.6) and (3.7). G_ℓ is the beamforming gain on the ℓ^{th} NLOS link. β is the reflection loss due to a reflector in the system and is modeled as the expected power reflection coefficient of the reflector material, the details of which are provided in Appendix E. P_t is the transmit power in Watts. Note that, determining the mean received power becomes unwieldy due to the term: $e^{-\rho_\ell c_1 \sum_{i=1}^{Q_\ell} R_{\ell,i}^{1/2}}$. To get an approximate yet tractable expression for the mean received power we apply the central limit theorem (CLT) [24] to the above sum, as follows.

Let $Y = e^{sX}$ where, $X = \sum_{i=1}^{Q_\ell} R_{\ell,i}^{1/2}$ and $s = -\rho_\ell c_1$. Applying the CLT, $X \sim \mathcal{N}(\mu_X, \sigma_X^2)$ where, $\mu_X = Q_\ell \mathbb{E}\left[R_{\ell,i}^{1/2}\right] = Q_\ell \mu_R/2$, $\sigma_X^2 = Q_\ell \mathbb{V}\left[R_{\ell,i}^{1/2}\right] = Q_\ell \sigma_R^2/4$. Thus, $\mathbb{E}[Y] = e^{s\mu_X + s^2\sigma_X^2/2} = e^{\frac{sQ_\ell\mu_R}{2} + \frac{s^2 Q_\ell \sigma_R^2}{8}}$. Thus,

$$S(Q_\ell) \approx c(Q_\ell) R^{-\eta}(Q_\ell) e^{a_\ell R(Q_\ell) + b_\ell Q_\ell}$$

where, $c(Q_\ell) := \frac{G_\ell \beta^{Q_\ell - 1} P_t}{h_{fs}(r_0) r_0^{-\eta}} \mathbb{E}[Y]$, $a_\ell := -\rho_\ell c_2$, $b_\ell := -\rho_\ell b$.

Letting $S(q_\ell)$ denote the received power when $Q_\ell = q_\ell$ we have,

$$\begin{aligned}
&F_{S(q_\ell)}(z) \\
&= Pr\left\{c(Q_\ell)\, R^{-\eta}(Q_\ell) e^{a_\ell R(Q_\ell)+Q_\ell b_\ell} \leq z \mid Q_\ell = q_\ell\right\} \\
&= Pr\left\{\frac{-a_\ell R(q_\ell)}{\eta} e^{-a_\ell \frac{R(q_\ell)}{\eta}} \leq -\frac{a_\ell}{\eta}\left(\frac{z}{c(q_\ell)}\right)^{-1/\eta} e^{\frac{q_\ell b_\ell}{\eta}}\right\} \\
&= Pr\left\{\frac{-a_\ell R(q_\ell)}{\eta} \leq W\left(-\frac{a_\ell}{\eta}\left(\frac{z}{c(q_\ell)}\right)^{-1/\eta} e^{\frac{q_\ell b_\ell}{\eta}}\right)\right\} \\
&= Pr\left\{R(q_\ell) \geq \underbrace{-\frac{\eta}{a_\ell} W\left(-\frac{a_\ell}{\eta}\left(\frac{z}{c(q_\ell)}\right)^{-1/\eta} e^{\frac{q_\ell b_\ell}{\eta}}\right)}_{:=f(z)}\right\} \\
&= 1 - F_{R(q_\ell)}\left(f(z)\right)
\end{aligned} \tag{3.8}$$

where, $W(\cdot)$ denotes the Lambert W function. Let U_ℓ denote the envelope of the received signal on the ℓ^{th} NLOS link, $1 \leq \ell \leq L$. We assume that the ℓ^{th} link undergoes Ricean fading with K-factor K_ℓ. This can be modeled by assuming $U_\ell \sim \mathcal{NG}(\nu_\ell, \theta_S(q_\ell))$ where, $\nu_\ell = \frac{(K_\ell+1)^2}{2K_\ell+1}$ and

$$\begin{aligned}
\theta_S(q_\ell) &:= \mathbb{E}\left[S(Q_\ell) \mid Q_\ell = q_\ell\right] \\
&= \int_{z^-}^{z^+} \left(1 - F_{S(q_\ell)}(z)\right)\, \mathrm{d}z \\
&= \int_{z^-}^{z^+} F_{R(q_\ell)}\left(f(z)\right)\, \mathrm{d}z
\end{aligned} \tag{3.9}$$

where, $z^- = c(q_\ell)(wq_\ell)^{-\eta} e^{a_\ell w q_\ell + b(q_\ell)}$ and $z^+ = c(q_\ell)(W_d q_\ell)^{-\eta} e^{a_\ell W_d q_\ell + b(q_\ell)}$. Note that, the above holds because $R(q_\ell) \in (wq_\ell, W_d q_\ell]$ is a non-negative random variable. From Appendix D we know that $R(Q_\ell) \sim \mathcal{LN}(\mu_R(q_\ell), \sigma_R^2(q_\ell))$. Thus, from (3.9) we have

$$\theta_S(q_\ell) = \int_{z^-}^{z^+} \Phi\left[\frac{\ln(f(z)) - \mu_R(q_\ell)}{\sigma_R(q_\ell)}\right] \mathrm{d}z \tag{3.10}$$

Thus, the SNR on the ℓ^{th} NLOS link is given by

$$\Lambda_\ell = \frac{{U_\ell}^2}{N_\ell}. \tag{3.11}$$

In the above, $N_\ell = G_\ell \kappa T N_f W \times 10^3$ is the noise power on the ℓ^{th} NLOS link in mW where, κ denotes the Boltzmann constant in J/K, T denotes the temperature of the receiver in K, and N_f denotes the noise figure of the receiver. W is the system bandwidth in Hz.

Fact 1 (Scaling Gamma Distribution)**.** If $Y \sim \mathcal{G}(\alpha, \beta)$ where $\alpha\,(>0)$ and $\beta\,(>0)$ are the shape and scale parameters, respectively, then for $c > 0$, $cY \sim \mathcal{G}\,(\alpha, c\beta)$.

Since, $U_\ell \sim \mathcal{NG}(\nu_\ell, \theta_S(q_\ell))$, ${U_\ell}^2 \sim \mathcal{G}(\nu_\ell, \theta_S(q_\ell)/\nu_\ell)$. Applying the scaling property of gamma distribution in Fact (1) to (3.11), we have $\Lambda_\ell \sim \mathcal{G}(\nu_\ell, \theta_S(q_\ell)/N_\ell\nu_\ell)$.

LOS SNR

Let V denote the envelope of the received signal on the LOS link. Assuming that the LOS link undergoes Ricean fading with K-factor K_0, we model the small-scale fading on the LOS link as Nakagami-ν_0 with $\nu_0 = \frac{(K_0+1)^2}{2K_0+1}$ and the average received signal power

$$\theta_0 = \frac{G_0 P_t}{h_0} \overline{A}(r_{tr})\big|_{\rho=\rho_0}. \tag{3.12}$$

Here, G_0 is the gain on the LOS link, ρ_0 is the blocker density seen by the LOS link, $h_0 = h_{fs}(r_0)\left(\frac{r_{tr}}{r_0}\right)^{\eta_0}$ with η_0 as the LOS path loss exponent. The SNR on the LOS link is thus given by $\Lambda_0 = V^2/N_0$ where, $N_0 = G_0 \kappa T N_f W \times 10^3$ is the noise power on the LOS link in mW. Following the analysis for the NLOS case in Section 3.1.4, we have $\Lambda_0 \sim \mathcal{G}(\nu_0, \theta_0/N_0\nu_0)$.

3.1.5 Retransmission Process

The retransmission process shown in Fig. is two-dimensional with space (direction) and time being the two dimensions. Beams are formed for the LOS and the L NLOS ULAs of the

receiver with gains that are subject to change in both the spatial and temporal dimensions. Note that, the spatial dimension is indexed by ℓ, $0 \leq \ell \leq L$ and the temporal dimension by i, $1 \leq i \leq t$. The ℓ^{th} beam is assumed to experience blockage with a blocker population density ρ_ℓ. The density ρ_ℓ remains constant over all retransmissions. Whereas, the beam gains are sampled from a distribution. This distribution is an evaluation parameter and is described in Section 3.1.5.

Let T denote the random variable whose realizations are the number of retransmissions (t) taken for successful decoding and ρ_ℓ denote the blocker intensity seen by the ℓ^{th} link. Note that the $\ell = 0$ corresponds to the LOS link. Let $G_\ell^{(i)} \in \mathcal{G}$ denote the beam gain on the ℓ^{th} NLOS link at the i^{th} transmission. Finally, let $\mathcal{G} = \{\alpha_1, \alpha_2, \ldots, \alpha_K\}$ be the set of gains that can be provided by the ULAs at the receiver.

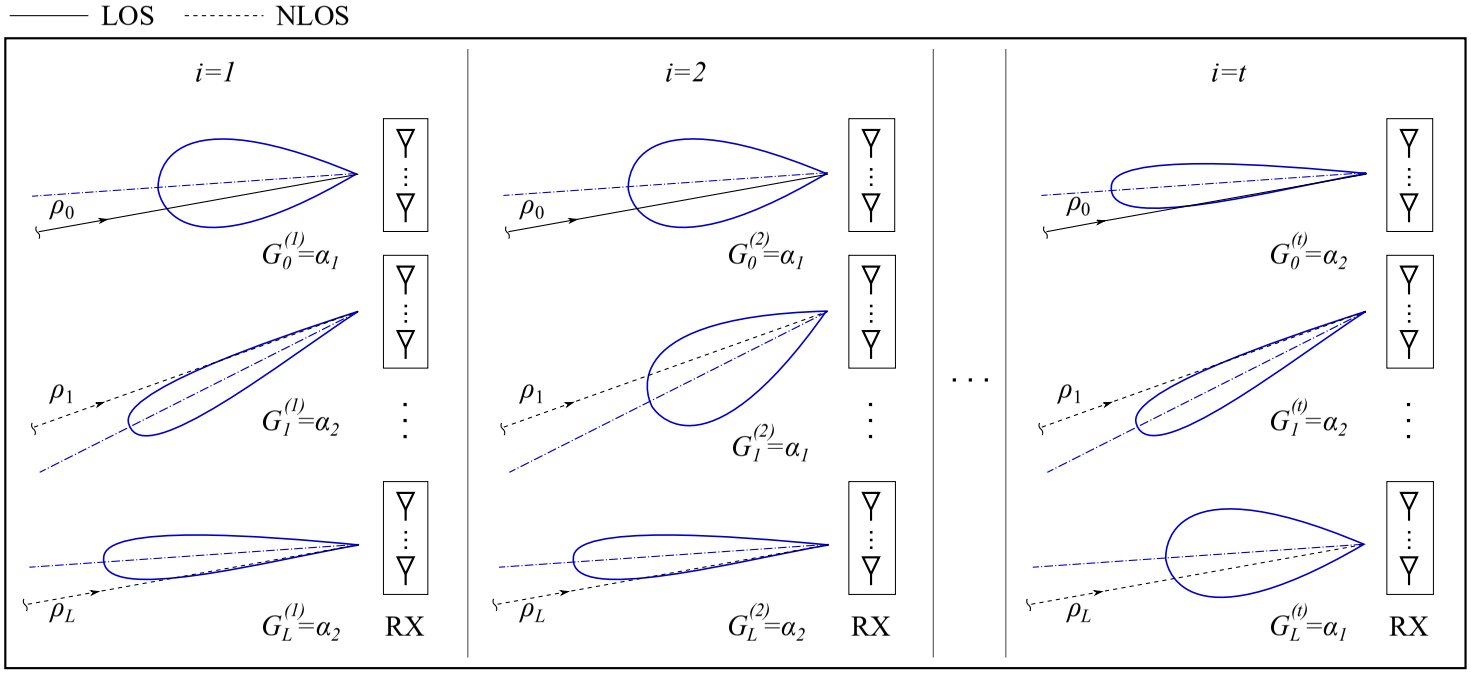

Figure 3.6: Gain of the arriving beam and the corresponding blocker intensity assignment at each step of the retransmission process. Beam lobe patterns are shown for ease of illustration, they are not representative of the actual values chosen. In the above example, $\mathcal{G} = \{\alpha_1, \alpha_2\}$ with $\alpha_1 < \alpha_2$.

System Efficiency

We evaluate the performance of the retransmission schemes in terms of the throughput and number of retransmissions required to achieve decoding success. We begin by formulating the probability of decoding failure. Let $P_f(t) = \Pr\left\{\text{decoding failure at the } t^{\text{th}} \text{ transmission}\right\}$ and let $\mathbf{G}^{(i)} = \left[G_0^{(i)}, G_1^{(i)}, \ldots, G_L^{(i)}\right]^{\mathsf{T}}$, $1 \le i \le t$.

$$P_f(t) = \sum_{\mathcal{G}^{t(L+1)}} \Pr\left\{\mathbf{G}^{(1)} = \mathbf{g}_1, \ldots, \mathbf{G}^{(t)} = \mathbf{g}_t\right\} \tag{3.13}$$

$$\times \Pr\left\{C\left(t; \mathbf{g}_1, \ldots, \mathbf{g}_t\right) < R_{se} \mid C\left(t-1; \mathbf{g}_1, \ldots, \mathbf{g}_{(t-1)}\right) < R_{se}\right\}$$

$$\overset{\text{(a)}}{=} \sum_{\mathcal{G}^{t(L+1)}} \Pr\left\{\mathbf{G}^{(1)} = \mathbf{g}_1, \ldots, \mathbf{G}^{(t)} = \mathbf{g}_t\right\} \times \frac{\Pr\left\{C\left(t; \mathbf{g}_1, \ldots, \mathbf{g}_t\right) < R_{se}\right\}}{\Pr\left\{C\left(t-1; \mathbf{g}_1, \ldots, \mathbf{g}_{(t-1)}\right) < R_{se}\right\}}$$

$$\overset{\text{(b)}}{=} \sum_{\mathcal{G}^{t(L+1)}} \left(\prod_{\ell=1}^{L+1} P_{G_\ell}\left(g_\ell\right)\right)^t \times \frac{\Pr\left\{C\left(t; \mathbf{g}_1, \ldots, \mathbf{g}_t\right) < R_{se}\right\}}{\Pr\left\{C\left(t-1; \mathbf{g}_1, \ldots, \mathbf{g}_{(t-1)}\right) < R_{se}\right\}} \tag{3.14}$$

Then the probability of decoding failure can be expressed by equation Step (a) in (3.14). In (3.14) Step (a), $\mathcal{G}^{t(L+1)}$ denotes the set of $t(L+1)$-tuples of $\mathcal{G}$ and $C\left(t; \mathbf{g}_1, \ldots, \mathbf{g}_t\right)$ denotes the capacity at the t^{th} transmission given beam gains $\mathbf{G}^{(i)} = \mathbf{g}_i$ at the i^{th} transmission, $1 \le i \le t$. R_{se} is the target rate in bps/Hz. Step (a) is due to the following.

$$\Pr\left\{C\left(t; \mathbf{g}_1, \ldots, \mathbf{g}_t\right) < R_{se}, C\left(t-1; \mathbf{g}_1, \ldots, \mathbf{g}_{(t-1)}\right) < R_{se}\right\}$$

$$= \Pr\left\{C\left(t; \mathbf{g}_1, \ldots, \mathbf{g}_t\right) < R_{se}\right\},$$

Further, if we assume that $G_\ell^{(i)} = G_\ell$, $1 \leq i \leq t$, $0 \leq \ell \leq L$, then, the probability of decoding failure is given by (3.14) where,

$$\begin{aligned}
&\Pr\left\{\mathbf{G}^{(1)} = \mathbf{g}_1, \ldots, \mathbf{G}^{(t)} = \mathbf{g}_t\right\} \\
&= \prod_{i=1}^{t} \Pr\left\{\mathbf{G} = \mathbf{g}\right\} \\
&= \left(\Pr\left\{(\mathbf{G}_1, \ldots, \mathbf{G}_{L+1}) = (\mathbf{g}_1, \ldots, \mathbf{g}_{L+1})\right\}\right)^t \\
&= \left(\prod_{\ell=1}^{L+1} P_{G_\ell}\left(g_\ell\right)\right)^t . \qquad (3.15)
\end{aligned}$$

where,

$$P_{G_\ell}(g_\ell) = \begin{cases} p_k^{(\ell)} & g_\ell = \alpha_k, 1 \leq k \leq K \\ 0 & \text{otherwise.} \end{cases}$$

Note that, the above distribution is a system parameter. It represents the bias that the system has towards a particular beam gain from the set $\mathcal{G}$.

Outage Probability at the t^{th} Transmission

The probability of outage at the t^{th} transmission $\Pr\left\{C\left(t; \mathbf{g}_1, \ldots, \mathbf{g}_t\right) < R_{se}\right\}$ in (3.14) is derived as follows. Let Q_ℓ be the random variable denoting the number of hops on the ℓ^{th} NLOS link and let $\mathbf{Q} = [Q_1, Q_2, \ldots, Q_L]$. Then, the capacity at the t^{th} transmission with $\mathbf{Q} = \mathbf{q}$ hops is:

$$\begin{aligned}
C\left(t; \mathbf{g}_1, \ldots, \mathbf{g}_t, \mathbf{q}\right) &= \sum_{i=1}^{t} \log_2\left(1 + \Lambda^{(i)}(\mathbf{q})\right) \\
&\leq t \log_2\left(1 + \frac{1}{t}\sum_{i=1}^{t} \Lambda^{(i)}(\mathbf{q})\right) \\
&= t \log_2\left(1 + \frac{1}{t}\Lambda_e^{(t)}(\mathbf{q})\right) \qquad (3.16)
\end{aligned}$$

Let $\Lambda_e^{(t)}(\mathbf{q}) := \sum_{i=1}^{t} \Lambda^{(i)}(\mathbf{q})$. Note that $\tilde{\mathbf{Q}}_t \in \mathcal{Q}$ where, $\mathcal{Q}$ is the set of $\sum_{i=1}^{t} \ell_i$-tuples of $\{2, 3, \ldots, q_m\}$. Thus,

$$\begin{aligned}
&\Pr\left\{C\left(t; \mathbf{g}_1, \ldots, \mathbf{g}_t, \mathbf{q}\right) < R_{se}\right\} \\
&= \Pr\left\{t \log_2\left(1 + \frac{1}{t}\Lambda_e^{(t)}(\mathbf{q})\right) < R_{se}\right\} \\
&= \Pr\left\{\Lambda_e^{(t)}(\mathbf{q}) < t(2^{R_{se}/t} - 1)\right\} \\
&= F_{\Lambda_e^{(t)}(\mathbf{q})}\left[t(2^{R_{se}/t} - 1)\right] \qquad (3.17)
\end{aligned}$$

Thus,

$$\begin{aligned}
&\Pr\left\{C\left(t; \mathbf{g}_1, \ldots, \mathbf{g}_t\right) < R_{se}\right\} \\
&= \sum_{\mathbf{q} \in \mathcal{Q}^L} F_{\Lambda_e^{(t)}(\mathbf{q})}\left[t(2^{R_{se}/t} - 1)\right] P_{\mathbf{Q}}(\mathbf{q}) \\
&\overset{(a)}{=} \frac{1}{(q_m - 1)^L} \sum_{\mathbf{q} \in \mathcal{Q}^L} F_{\Lambda_e^{(t)}(\mathbf{q})}\left[t(2^{R_{se}/t} - 1)\right] \\
&= \frac{1}{(q_m - 1)^L} \sum_{\mathbf{q} \in \mathcal{Q}^L} \frac{\gamma\left(\nu_{e,t}(\mathbf{q}), \frac{t(2^{R_{se}/t} - 1)}{\theta_{e,t}(\mathbf{q})}\right)}{\Gamma\left(\nu_{e,t}(\mathbf{q})\right)} \qquad (3.18)
\end{aligned}$$

where in (a) we have used (3.3) to give,

$$P_{\mathbf{Q}}(\mathbf{q}) = \prod_{\ell=1}^{L} P_{Q_\ell}(q_\ell) = \prod_{\ell=1}^{L} \frac{1}{(q_m - 1)} = \frac{1}{(q_m - 1)^L} \qquad (3.19)$$

Expected Throughput

The expected throughput $\overline{R}$ of the retransmission scheme can be considered as a measure of efficiency of the scheme. Using the relation between the throughput and the total number of transmissions taken to achieve decoding success we have,

$$\overline{R} = \frac{R_{se}}{\mathbb{E}[T]} \text{bps/Hz} \qquad (3.20)$$

Symbol	Parameter Description	Value
f_C	carrier frequency	28 GHz
W	system bandwidth	0.5 GHz
T	receiver temperature	298.15 K
N_f	receiver noise figure	6 dB
r_0	close-in reference distance	5 m
η_0	LOS path loss exponent	2.55
η	NLOS path loss exponent	5.76
P_t	transmit power	1 dBm
N_t	number of transmit antennas	4
N_r	number of receive antennas	16
(W_X, W_Y)	geography size	(100,80) m
r_{TR}	distance between the transmitter and the receiver	40 m
w	diameter of a blocker	0.35 m
w_r	diameter of the receiver	0.35 m
s	distance of the nearest blocker from the receiver	0.35 m
β	expected power reflection coefficient	0.3407

Table 3.1: Simulation parameters used to evaluate the retransmission efficiency shown in Fig. 3.7.

where, $\mathbb{E}[T]$ is the expected number of total transmissions taken for successful decoding. It is given as

$$\begin{aligned}\mathbb{E}[T] &= \sum_{t=1}^{\infty} t P_T(t) \\ &= \sum_{t=1}^{\infty} t\left[1 - P_f(t)\right] \prod_{i=1}^{t-1} P_f(i)\end{aligned} \tag{3.21}$$

3.2 Numerical Results and Discussion

The efficiency of the retransmission scheme in 3.20 is evaluated for various values of the blocker density. Note that, various values of the expected power reflection coefficient β are given in Table E.1 from Appendix E. For our simulation, we chose $\beta = 0.3407$ which corresponds to the human skin model measurements provided in [28]. Table 3.1 lists the

parameters and their values used in the simulation and the corresponding results are shown in Fig. 3.7.

The set of beam gains provided by the ULAs $\mathcal{G} = \{N_t N_r/4, N_t N_r\}$. The results in Fig. 3.7 are provided for four configurations. Each configuration is defined by the following. The probability of selecting a beam gain is denoted by the matrix $\mathbf{P}_i = \left[p_k^{(\ell)}\right] \in \mathbb{R}^{(L+1)\times K}$, $i = \{1, 2\}, K = |\mathcal{G}|$. Results in Fig. 3.7 and 3.8 use the values $p_1^{(\ell)} = 0.9$ for the case of broad beams (BB) and $p_1^{(\ell)} = 0.1$ for narrow beams (NB). The blocker population density on the NLOS links (relative to that on the LOS link) is denoted by the vector $\boldsymbol{\rho} = [\rho_\ell] \in \mathbb{R}^{1\times L}$. From the results we see that, the throughput loss gap (function of ρ_0) widens as the misalignment increases. The system that favors narrow beams outperforms the broad beam (BB) system when there is no misalignment. However, as the misalignment increases, the performance of NB systems degrades significantly. Such a loss in the system efficiency is significant for bandwidths of upto 100 MHz (for FR1), 400 MHz (for FR2), and 800 MHz (for the case of aggregated bands).

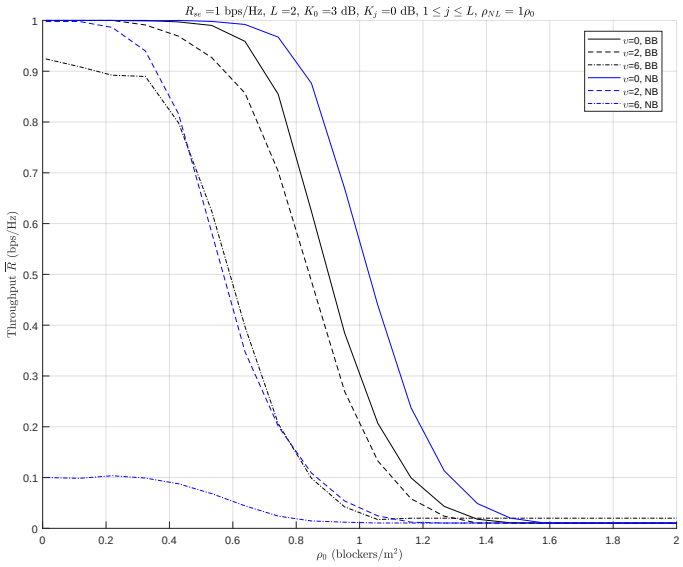

(a)

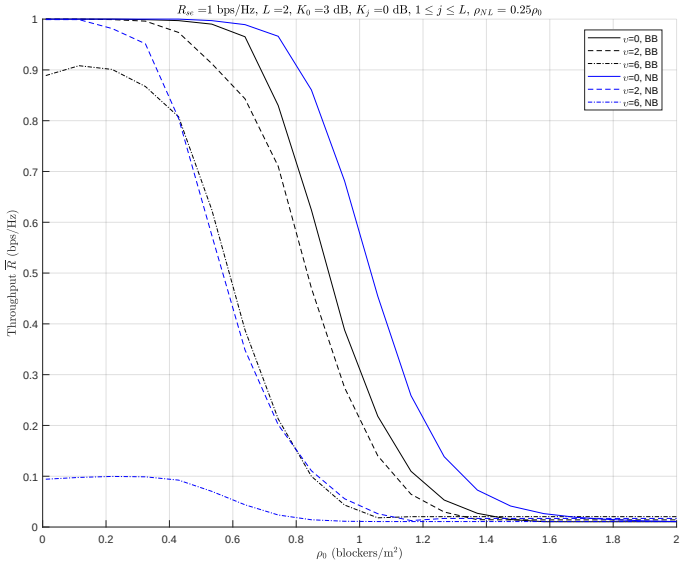

(b)

Figure 3.7: Retransmission efficiency as a function of the blocker density ρ_0 on the LOS link for various values of misalignment.

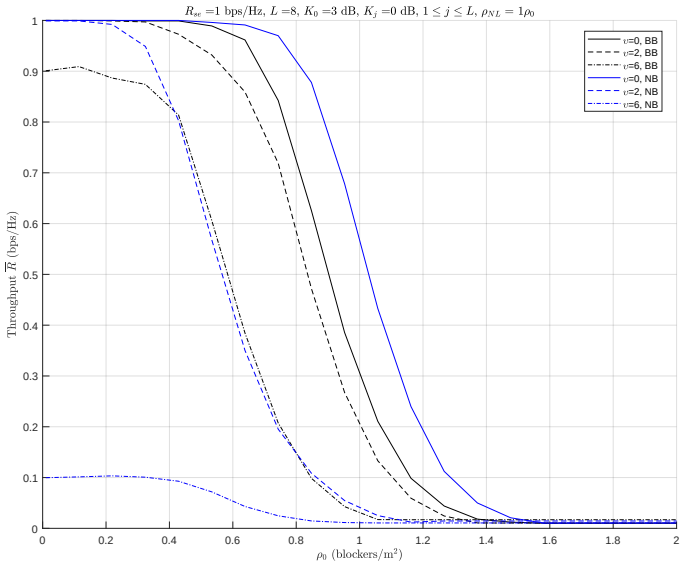

(a)

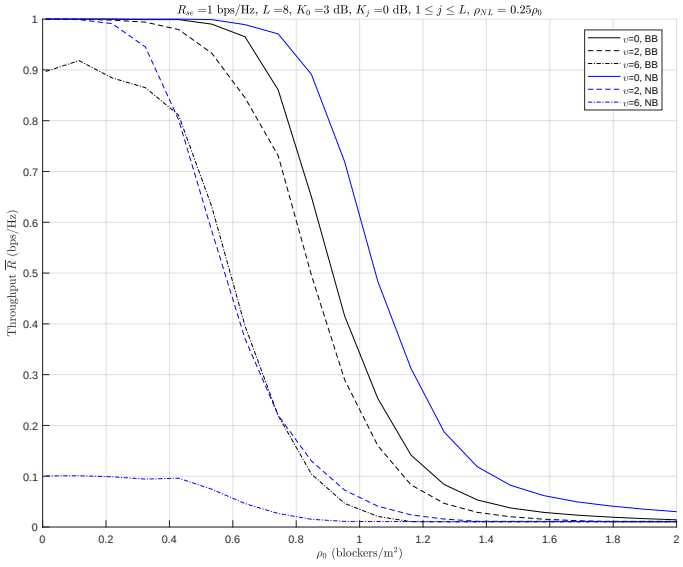

(b)

Figure 3.8: Retransmission efficiency as a function of the blocker density ρ_0 on the LOS link for various values of misalignment (continued from Fig. 3.7).

Chapter 4

The 3GPP mm-wave Urban Microcell Channel

The accurate representation of the communication channel is at the very foundation of communication system design. As the development of communication and signal processing algorithms is based on the channel model, its accuracy can directly impact key system performance metrics such as the data rate, power consumption, receiver complexity, and so on. This can further impact the cost and time for commercial deployment and eventually widespread technology adoption.

The Urban Microcell (UMi) scenario will likely be one of the key drivers of commercial success for 5G cellular networks due to its characteristically high data traffic demand. Unsurprisingly, this scenario is found in several channel modeling projects being proposed. In this chapter we provide an overview of generating the UMi channel in one such model: the 3GPP study item technical report (TR) 38.901 [1]. The intent is to summarize the core channel generation procedure with illustrative results, particularly useful for readers unfamiliar with the presentation style typical to standard documents. Mm-wave signals are susceptible to penetration losses due to stationary objects in the environment, for example, losses upwards of 150 dB due to building materials such as concrete and bricks [29]. They can also be attenuated by mobile objects, such as humans resulting in up to 25-30 dB loss [21]. From the results in Chapter 2, Fig. 2.6 and Fig. 2.7, it is not hard to see that a link blockage can last for several seconds and result in a significant loss of throughput. To measure the effect of this phenomenon, the 3GPP study item

recommends two blockage models. An implementation of these can become a valuable tool for a researcher engaged in developing techniques to combat blockages. However, as of today, open access implementations are few. A notable work that implements the earlier version of the TR 38.901 channel model on the ns-3 platform is described in [30]. Authors in [30] have presented an implementation of the 3GPP channel model for the 6 GHz to 100 GHz band in ns-3. To facilitate the study of the 3GPP UMi mm-wave channel for 5G systems, in this work, we have made available an open access implementation [31] in LabVIEW Communications System Design Suite 2.0 of the main channel generation procedure with the optional features of spatial consistency and blockage modeling.

To being with, we contrast the main aspects of the 3GPP model some noteworthy mm-wave channel models that are being developed by standard bodies around the world. Further, an overview of the basic channel generation procedure is provided. Continuing in the same vein, implementation results for the blockage modeling procedures in the 3GPP standard are presented for a representative Urban Microcell-Street Canyon (UMi-SC) scenario.

4.1 5G mm-wave Channel Modeling

Analytical channel models are based on mathematical analysis to characterize the channel response. Whereas, physical models are built upon the electromagnetic propagation of the signal. These can largely be put into two categories: statistical and deterministic. As the name suggests, in the statistical methodology channel parameters follow probability distributions modeled on actual measurement data gathered from various real-world environments. In the deterministic methodology, the impact of the environment on signal propagation is typically precisely determined by ray tracing simulation techniques. This is

especially useful when measurement data is unavailable. It is not hard to see that, deterministic models are more computationally intensive than their statistical counterparts and may become impracticable for an environment with a large number of scatterers, transmitters, and receivers, for instance. A survey of models for 5G mm-wave is beyond the scope of this article, the interested reader is referred to an insightful survey of physical channel models in [6]. Nevertheless, 4.1 contrasts the main aspects of the 3GPP model with some popular standard-based channel modeling projects.

The method for modeling blockages varies with the standard. Probability of line of sight (LOS) models have been specified in the ITU-R [7] and the METIS [8] models. The METIS channel model also provides simulation results for the UMi and D2D scenarios in the presence of objects in the environment. It also provides a body blockage (or self-blockage) model for 60 GHz. The probability of LOS for the ITU-R and the METIS channel models in the outdoor UMi scenario is shown in Fig. 1. The MiWEBA [9] model being quasi-deterministic (statistical ray tracing) in nature, estimates the ray blockage probability from measurement results for the Open Area and Street Canyon scenarios. The 3GPP model not only utilizes the probability of LOS model in Fig. 1 to determine the NLOS/LOS state of the link, but also specifies dedicated procedures to model the presence of objects such as humans and vehicles and the attenuation in the signal caused by such objects. The procedures and their simulation results are described in the following sections.

Project/ Standard	**Document**	**Carrier Frequency**	**Type**	**Scenarios**
ITU-R	Report ITU-R M.2135-1 (12/2009) [22]	Scenario based	Geometric Stochastic	Indoor Hotspot (3.4 GHz) UMi (2.5 GHz) Suburban UMa (2 GHz) RMa (800 MHz)
MiWEBA	Deliverable FP7-ICT 368721/D5.1 Channel Modeling & Charac. [32]	60 GHz	Hybrid/ Quasi-det. Statistical Ray Tracing	*Access*: Open Area, Street Canyon, Hotel Lobby *Backhaul/Fronthaul*: Above Roof Top, Street Canyon *Device to Device (D2D)*: Open Area, Street Canyon, Hotel Lobby
METIS	Deliverable ICT-317669 -METIS/D1.4 METIS Channel Models [23]	Model type dependent	Geometric Stochastic ($>$ 60 GHz) Map-based ($<$ 100 GHz) Hybrid	*Access*: UMi O2O & O2I, UMa O2O & O2I, RMa O2O & O2I, Office I2I, Shopping Mall I2I Highway, Open Air Festival O2O, Stadium O2O

3GPP	3GPP Rel 14 TR 38.901 V14.1.1 (2017-07) [33]	0.5 GHz to 100 GHz	Geometric Stochastic	*Access*: UMi-Street -Canyon O2O & O2I, Open Area O2O & O2I UMa-O2O & O2I Indoor-Office, Shopping Mall Stadium (open-roof) Gym (close-roof) *Backhaul/Fronthaul*: Outdoor Above Roof Top Street Canyon *Device to Device (D2D)*: Open Area, Street Canyon, Hotel Lobby

Table 4.1: Main aspects of examples of channel modelling projects. UMi: Urban Microcell, UMa: Urban Macrocell, RMa: Rural Macrocell, O2O; Outdoor to Outdoor, O2I: Outdoor to Indoor, I2O: Indoor to Outdoor, I2I: Indoor to Indoor, ITU-R: International Telecommunication Union-Radiocommunication Sector, MiWEBA: Millimeter-Wave Evolution for Back-haul and Access, METIS: Mobile and wireless communication Enablers for the Twenty-twenty Information Society, 3GPP: 3rd Generation Partnership Project.

4.2 Generating the Spatial Channel Model

The 3GPP SCM for mm-wave is developed for the frequency range of 6-100 GHz with support for bandwidths upto 10% of the carrier frequency with an upper limit of 2 GHz. Mm-wave specific requirements such as the modeling of atmospheric absorption and blockages is also considered, although, as an additional component to the basic model. The model supports mobility at one end of the link, typically the user terminal (UT) of up to 500 km/h.

Several environments for the operation of the radios have been identified and specified in the technical report. These are, the Urban Microcellular (UMi) -Street Canyon (SC) and -open area, the Urban Macrocellular (UMa) -Outdoor-to-Outdoor (O2O) and -Outdoor-to-Indoor (O2I), the Indoor, the Backhaul, the Device-to-Device (D2D)/Vehicle-to-Vehicle (V2V), and other scenarios such as Stadium (open-roof) and Gym (close-roof). In this work, we focus on the outdoor UMi-SC scenario where the BSs are below the rooftop levels of buildings surrounding the street and the UTs are on the ground level, modeling realistic scenarios such as the dense urban localities in New York City.

The overall procedure of generating the channel (basic procedure with the optional blockage modeling) is shown in Fig. 4.1. The following sections summarize the process and the associated results. A detailed description of the procedure is given in [1].

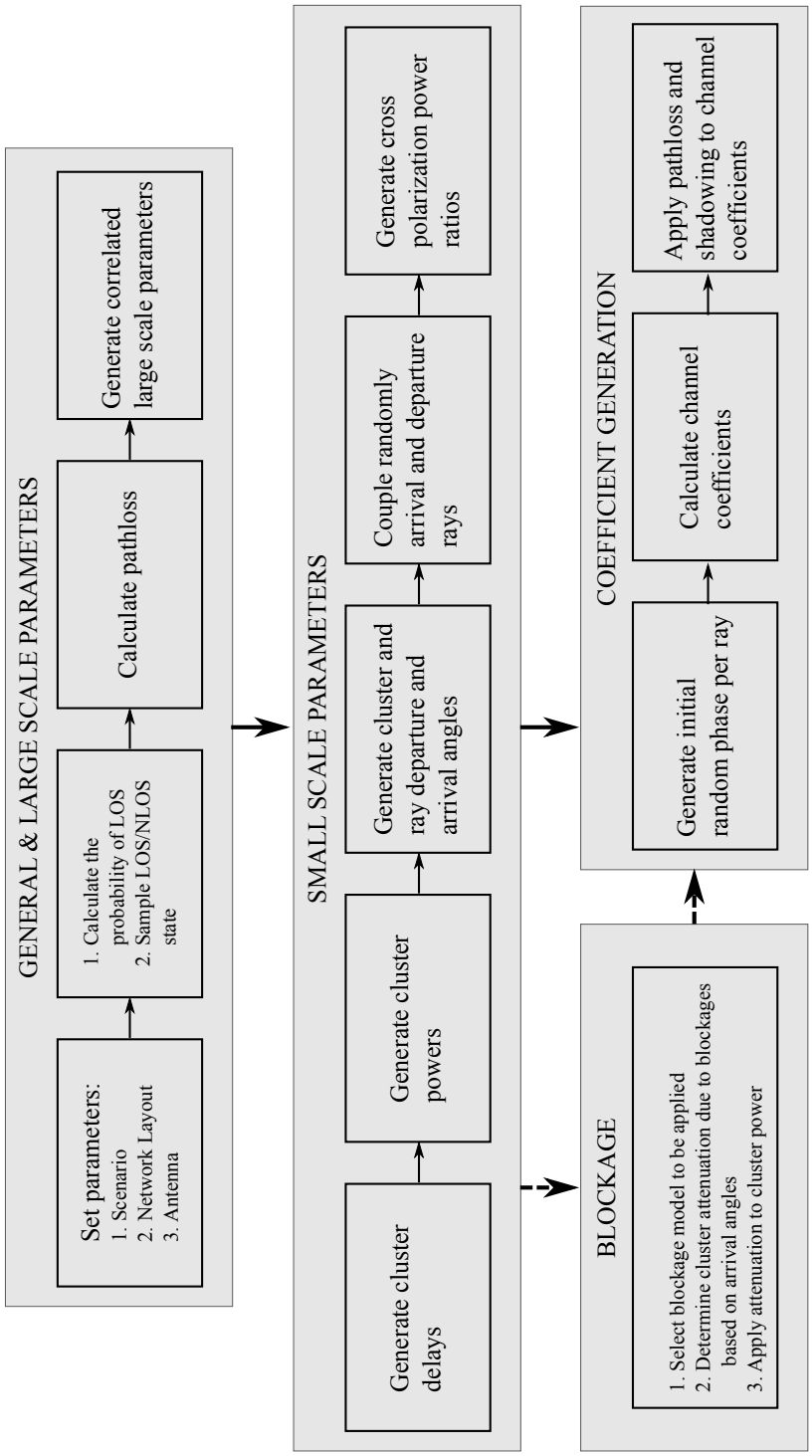

Figure 4.1: Block schematic detailing the channel coefficient generation procedure specified for the channel model.

Fig. 4.2 summarizes the notation while depicting the propagation mechanism assumed in the technical report. Note that the notation used is the same as that given in [1] for the sake of consistency.

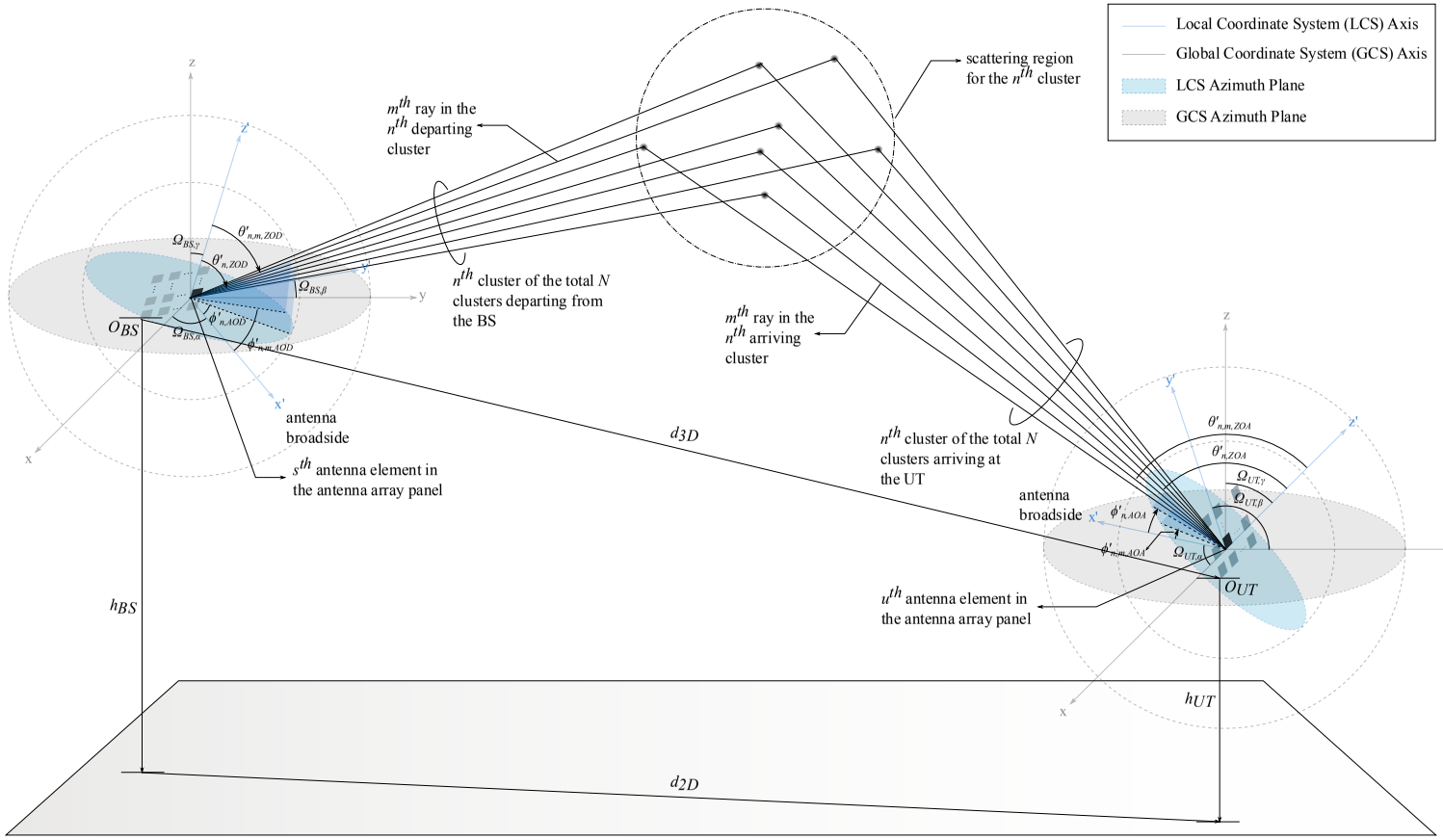

Figure 4.2: Schematic depicting the scattering of rays as modeled in the spatial channel model. Notation used is the same as that given in the TR 38.901 [1].

4.2.1 Pathloss and LOS Probability

The pathloss in the channel model is a function of the carrier frequency, the distance between the base station (BS) and UT (both 2D and 3D distance), and the LOS state of the BS-UT link. Tab. 7.4.1-1 in [1] specifies the pathloss model of each scenario. The pathloss of the UMi-SC scenario for some representative carrier frequencies in 3GPP 5G NR FR1 and FR2 is shown in Figure 4.3. As expected, the pathloss in FR2 is significantly higher than that at in FR1. Before the pathloss is computed, the probability of LOS (Pr_{LOS}) of the link is calculated. Tab. 7.4.2-1 in [1] lists the probability of LOS models for every scenario. This probability is a function of the horizontal plane distance (2D distance) with the antenna height fixed to a constant value per scenario. In our implementation, the LOS state is sampled from a Bern (Pr_{LOS}) distribution.

4.2.2 Antenna Model

The 3GPP channel model specifies beamforming in the azimuth and elevation. To perform such 3D beamforming, the antenna model is specified to be a uniform rectangular panel array (Sec. 7.3 in [1]). Compared to the antenna model for 3GPP LTE [34], which also specifies 3D (elevation) beamforming, there is additional flexibility to set the inter-panel distances in this model. The geometry of the antenna array and the related notation is shown in Fig. 4.5. All distances shown are normalized to the wavelength. In the implementation, a single antenna array is utilized per BS and UT. The antenna array is placed in the Y-Z plane as shown in Fig. 4.2. As a result, the distance vector for each antenna element is calculated as follows. The ℓ^{th} antenna element in the rectangular antenna panel array is located at (x_ℓ, y_ℓ, z_ℓ) where, $x_\ell = 0$, $y_\ell = d_H\left(\ell \bmod C - J\right) + Jd_{g,H}$, and $z_\ell = d_v\left(\left\lfloor \frac{\ell}{C} \right\rfloor - K\right) + Kd_{g,V}$. Here, $C = N_g N$, $J = \left\lfloor \frac{\ell}{N} \right\rfloor \bmod N_g$ and $K = \left\lfloor \frac{\ell}{NMN_g} \right\rfloor$. Distance vector $\mathbf{d}'_\ell$ in the LCS (w.r.t. the origin O) of the ℓ^{th} antenna element is given as,

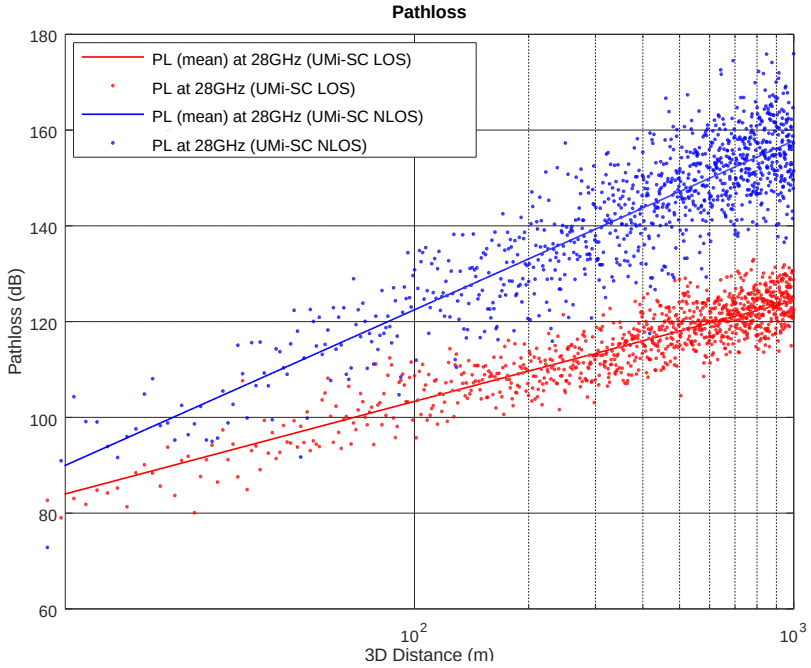

(a) 28 GHz

(b) 76 GHz

Figure 4.3: Pathloss for the Urban Micro-Street Canyon (UMi-SC) LOS and NLOS scenarios.

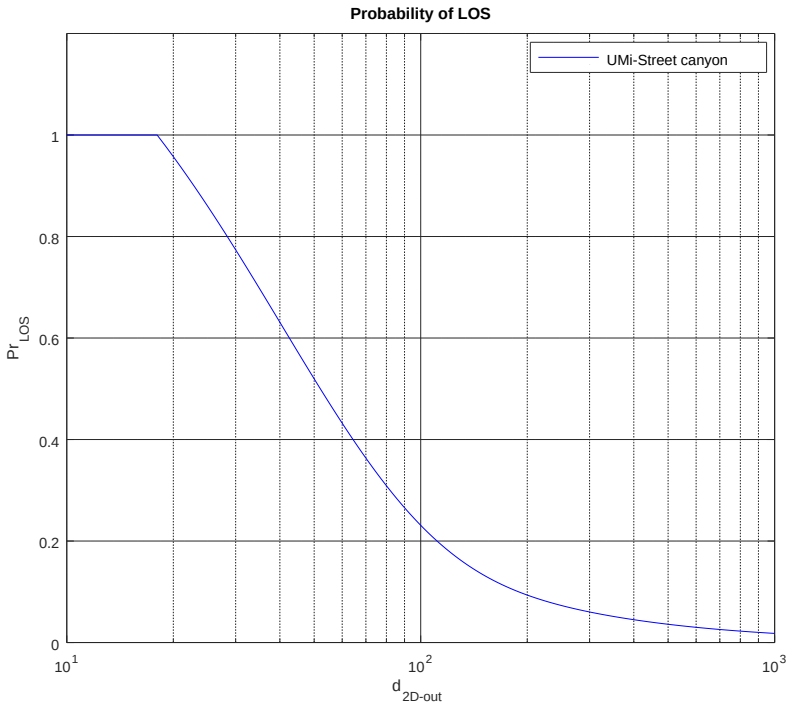

Figure 4.4: Probability of LOS for the UMi-SC scenario.

$\mathbf{d}_\ell = (x_\ell \hat{x}' + y_\ell \hat{y}' + z_\ell \hat{z}')$, where, $(\hat{x}', \hat{y}', \hat{z}')$ are the Cartesian unit vectors in the LCS. Using the above procedure, $\mathbf{d}'_{tx,s}$ and $\mathbf{d}'_{rx,u}$ are calculated for the s^{th} element at the transmit antenna and for the u^{th} element at the receive antenna, respectively.

The antenna element radiation pattern is shown in Fig. 4.6. To provide coverage in both the azimuth and the zenith, for a hexagonal cell with three sectors, the 3 dB beamwidth is set to 65°.

4.2.3 Large Scale Parameters

The fast fading or small scale parameters (SSPs) are all generated randomly for each BS and UT in the network, with their second moments as the large scale parameters (LSPs). The LSPs for the channel are the delay spread (DS), the Ricean factor (K), and the angular

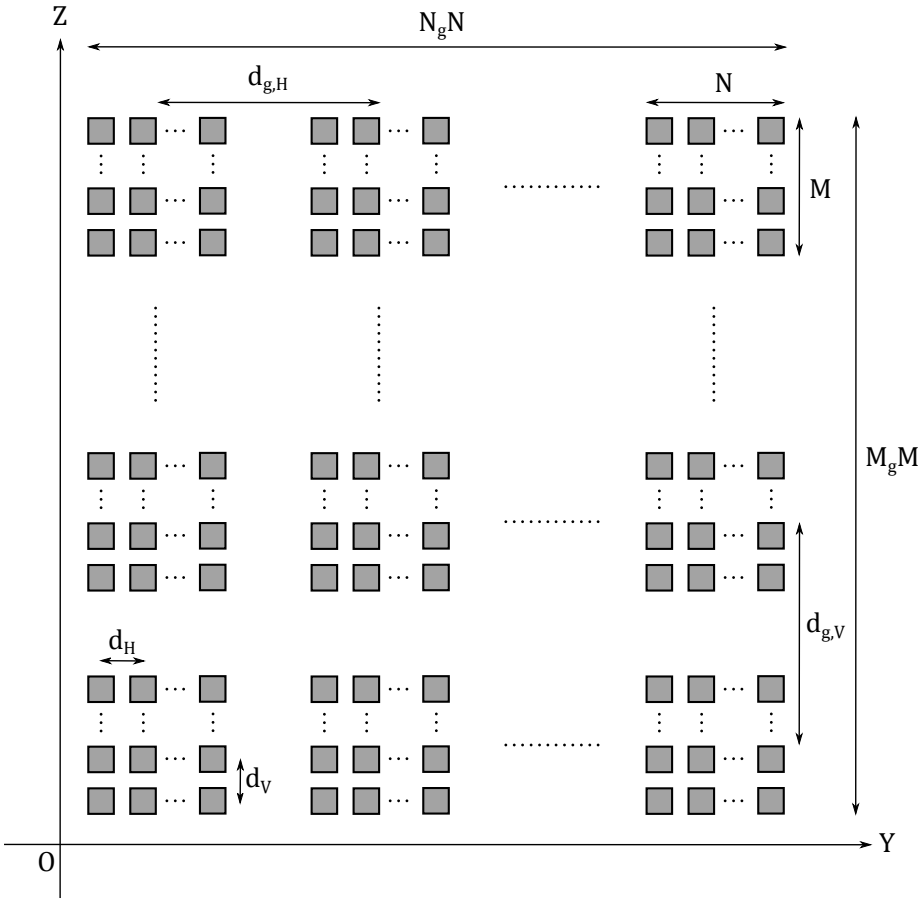

Figure 4.5: Uniform rectangular antenna array model (M_g, N_g, M, N, P). The solid black squares represent an antenna element and each smaller group of elements represents an antenna panel.

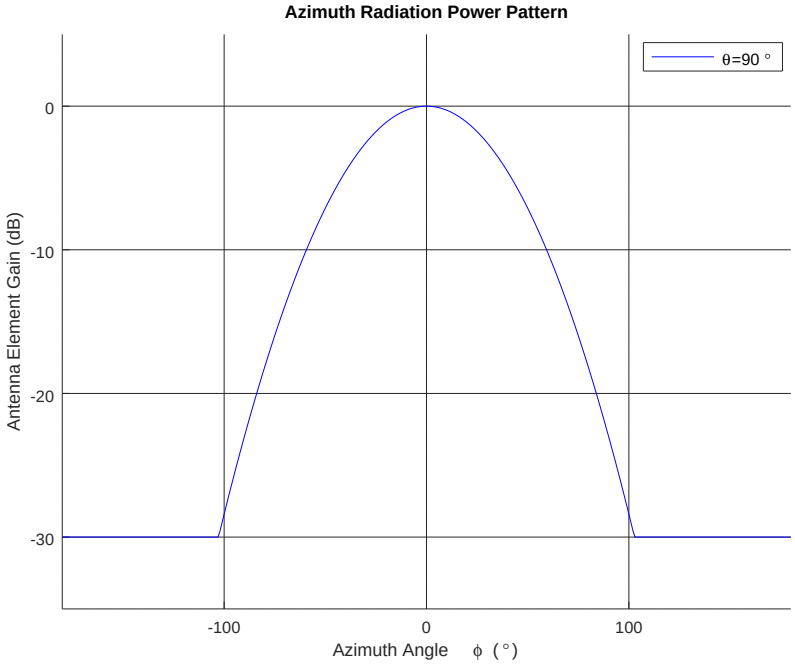

(a) Azimuth

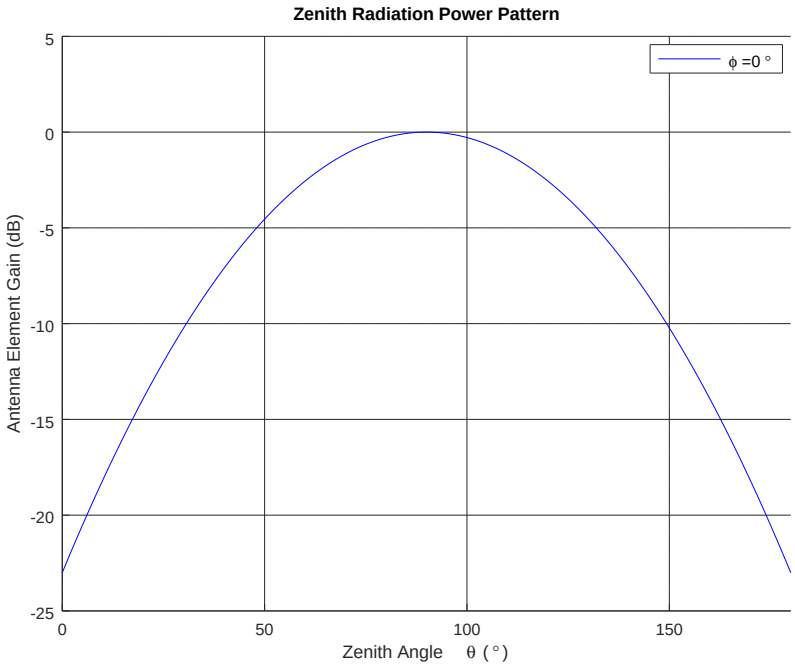

(b) Zenith

Figure 4.6: Antenna element radiation pattern.

spread of clusters in the azimuth and zenith for both departure and arrival; namely, azimuth spread of departure (ASD), azimuth spread of arrival (ASA), zenith spread of departure (ZSD), and zenith spread of arrival (ZSA). While generating SSPs based on the location of the UT is more accurate, it comes with a significant increase in complexity as these change with distances that are of the order of a wavelength. To bridge the gap between accuracy and ease of implementation, each LSP is generated randomly and is correlated in distance (2D or horizontal plane) to model the slow fading nature (changes over tens of wavelengths). The procedure to generate LSPs in Step 4 of Sec. 7.5 in [1] is based on that prescribed in the WINNER-II model (Sec. 3 in [35]).

To summarize the procedure, generation of the m^{th} LSP ($1 \leq m \leq M$) begins with creating a 2D grid (horizontal plane distance) of standard normal random variables, where the grid size is chosen such that it covers all the UTs in the network layout in addition to twice the correlation distance for that LSP. These random variables are correlated using a distance-decorrelation filter with an impulse response [35] that is given by:

$$h_m(d) = e^{-\frac{d}{\Delta_m}} \tag{4.1}$$

where, d is the distance between two locations of the UT and Δ_m is the correlation distance, both in meters. The value of Δ_m is found from measurement results, it depends on the scenario and is specified in Tab. 7.5-6 of [1]. The M LSP values for a location extracted from their respective grids are not necessarily independent, for instance, it is atypical to have a large DS and a large K at the same location. To model this relationship between the M LSPs, the location values are cross-correlated with each other. The corresponding correlation matrix is derived from the measurement results and is specified in Tab. 7.5-6 of [1]. Due to the slow fading nature of LSPs, it is more meaningful to observe the behavior over an area rather than a particular location. With this in view, an example dataset of LSPs per location is shown in Fig. 4.7. As mentioned earlier, the negative correlation

between DS and K is observed in the simulation results as expected.

In the following we provide the theoretical probability distributions of each LSP. A comparison of the theoretical and the empirical distribution is shown in Fig. 4.8. Let X denote the SF and K in dB units. Then, $X_{dB} = 10log_{10}(X) \sim \mathcal{N}(\mu_{X_{dB}}, \sigma_{X_{dB}})$ where, $\mu_{K_{dB}}$ and $\sigma_{K_{dB}}$ values are specified in Table 7.5.6 of [1]. The CDF is thus given by,

$$F_X(x) = 1 - Q\left(\frac{10log_{10}(x) - \mu_{X_{dB}}}{\sigma_{X_{dB}}}\right)$$

Fig. 4.8 shows the CDF for the UMi-SC-LOS scenario for SF and K where, $\mu_{SF_{dB}} = 0$ dB, $\sigma_{SF_{dB}} = 4$ dB, $\mu_{K_{dB}} = 9$ dB, and $\sigma_{K_{dB}} = 5$ dB.

Let Y denote the following LSPs: DS, ASD, ZSD, ASA, and ZSA in logarithmic units. Then, $lgY = log_{10}(Y) \sim \mathcal{N}(ln(10)\mu_{lgY}, ln(10)\sigma_{lgY})$ where, μ_{lgY} and σ_{lgY} values are specified in Table 7.5.6 of [1]. The CDF is thus given by,

$$F_Y(y) = 1 - Q\left(\frac{log_{10}(y) - \mu_{lgY}}{\sigma_{lgY}}\right)$$

Fig. 4.9 shows the CDF for the UMi-SC-LOS scenario where $\mu_{lgDS} = -2.4log_{10}(1 + f_C) - 7.14$, $\sigma_{lgDS} = 0.38$, $\mu_{lgASD} = -0.05log_{10}(1 + f_C) + 1.21$, $\sigma_{lgASD} = 0.41$, $\mu_{lgZSD} = max\left[-0.21, -14.8(\frac{d_{2D}}{1000}) + 0.01|h_{UT} - h_{BS}| + 0.83\right]$, $\sigma_{lgZSD} = 0.35$, $\mu_{lgASA} = -0.08log_{10}(1+ f_C) + 1.73$, $\sigma_{lgASA} = 0.014log_{10}(1 + f_C) + 0.28$, $\mu_{lgZSA} = -0.1log_{10}(1 + f_C) + 0.73$, $\sigma_{lgZSA} = -0.04log_{10}(1+f_C)+0.34$, and $f_C = 28$ GHz. As seen in the figure, the simulation results are largely in agreement with the values specified in the model.

4.2.4 Small Scale Parameters

Modeling small scale fading for a BS-UT link amounts to modeling the delay, the power, and the angular profile of several clusters that form the wireless link. For a given location in the set geography, the outcome of this statistical model is governed by the LSPs sampled at that location in the previous stage. This is the subject of Steps 5-9 in Sec. 7.5 of [1].

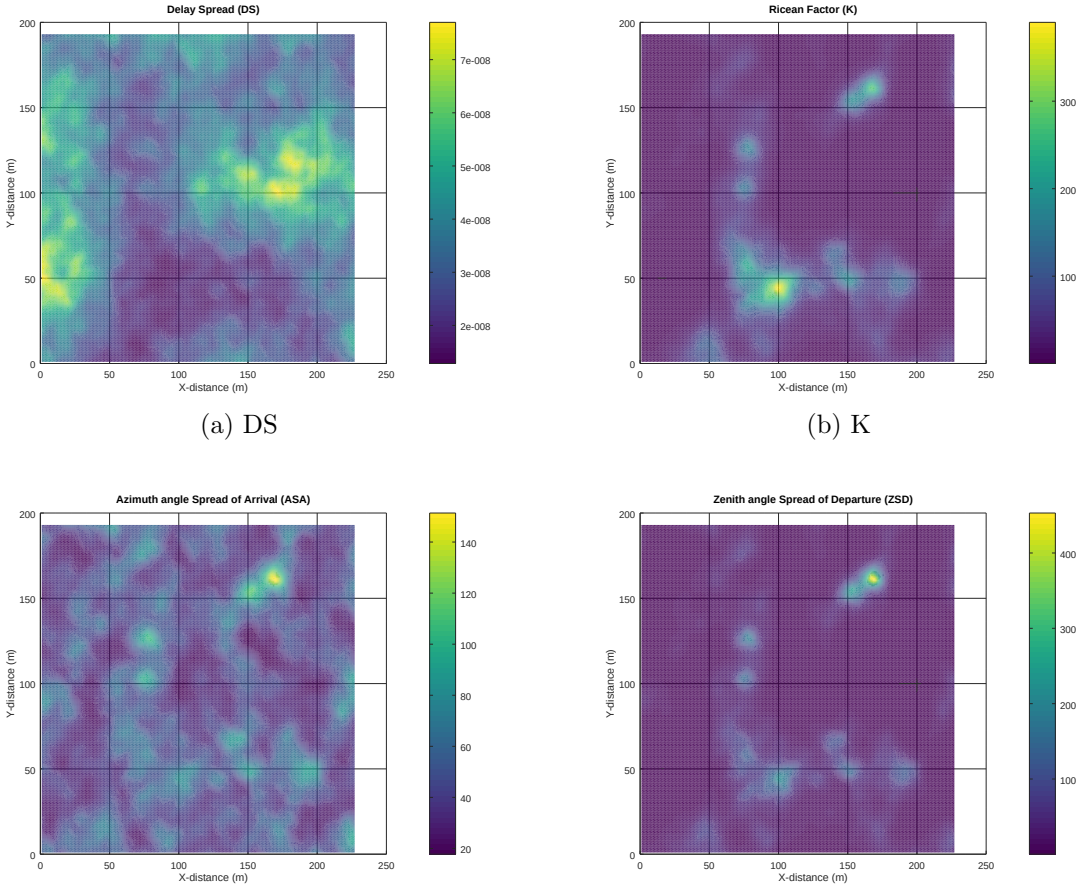

(a) DS (b) K

(c) ASA (d) ZSD

Figure 4.7: Location-based intensity plots of some LSPs for the UMi-SC scenario at $f_C = 28$ GHz.

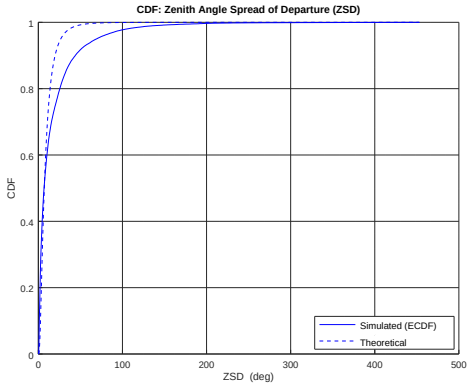

(a) ZSD

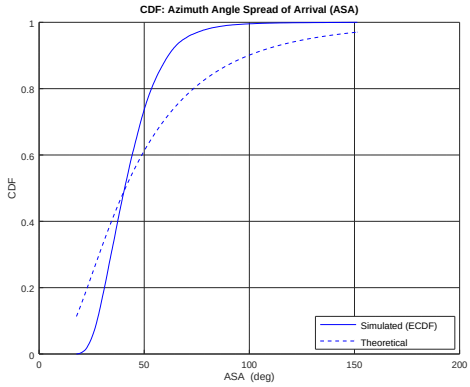

(b) ASA

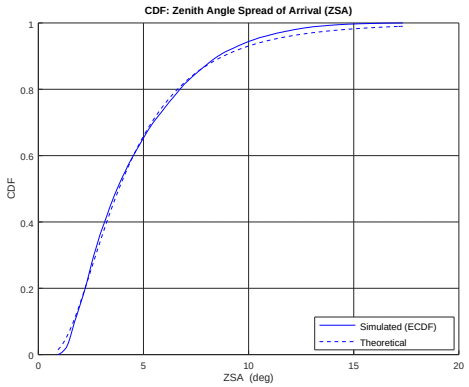

(c) ZSA

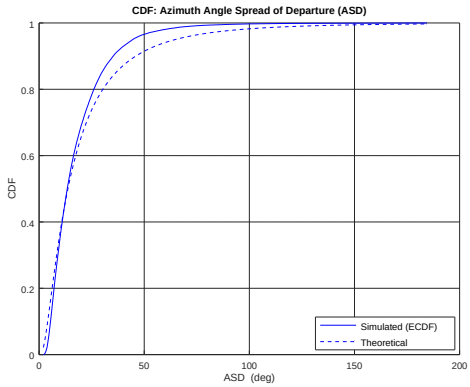

(d) ASD

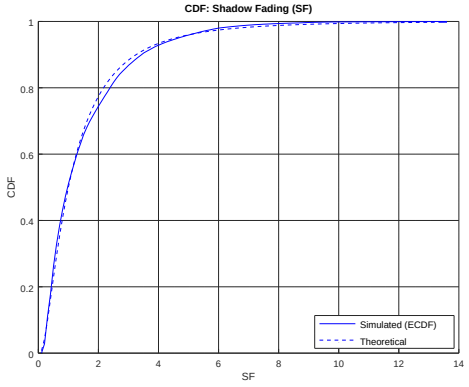

(e) SF

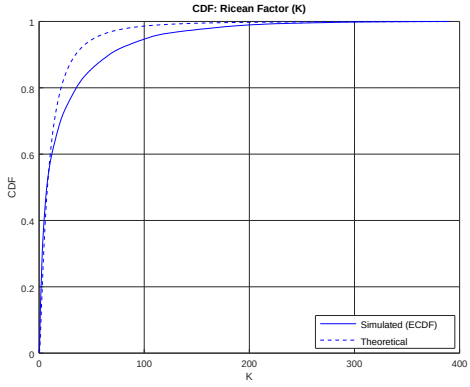

(f) K

Figure 4.8: Empirical and Theoretical CDFs of the LSPs for the UMi-SC-LOS scenario.

A link is comprised of N clusters, where N depends on the scenario. Modeling for the n^{th} cluster ($1 \leq n \leq N$) begins with sampling the cluster delay (τ_n) from an exponential distribution that is a function of DS. The power assignment (P_n) to each cluster depends on the cluster delay sampled above and is calculated assuming a single slope exponential power delay profile. In case the link is sampled as a LOS link, an additional specular component (set to $\frac{K}{K+1}$) is added to the first cluster. Also, clusters with less than -25 dB power relative to the maximum of all cluster powers are removed. Note that this final value of N is used for subsequent processing. The simulated results shown in Fig. 4.9 agree with the exponential distribution of τ_n and P_n.

The cluster angles are generated by applying the inverse Gaussian function in the azimuth case and the inverse Laplacian function in the zenith case with input parameter P_n and the respective LSP specifying the angular spread (ASD for AOD, ZSD for ZOD, ASA for AOA, and ZSA for ZOA). Positive or negative sign is assigned to the cluster angle randomly and Gaussian noise variation is added along with the LOS direction. Angles for each ray (set to 20 rays per cluster) of each cluster are generated; ray angle offsets are scenario dependent. In our simulation, ray angles are wrapped and mirrored to the front side of the antenna array. Consequently, azimuth angles are in the interval $[-180°, 180°]$ and zenith angles in the interval $[0°, 180°]$. The empirical CDFs for the cluster angles generated in the simulation for the UMi-SC scenario are shown in Fig. 4.9. The arrival and departure rays for both azimuth and zenith are randomly coupled with each other per cluster to model the effect of random scattering in the environment. Finally, cross polarization power ratios for each ray are sampled from a Lognormal distribution.

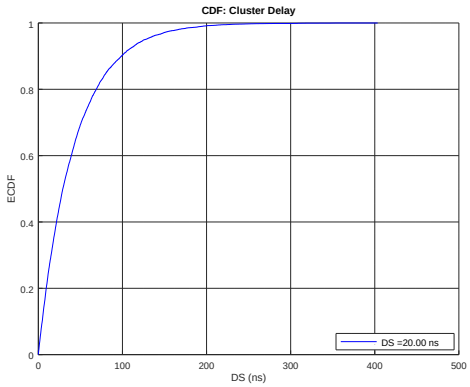

(a) τ_n

(b) P_n

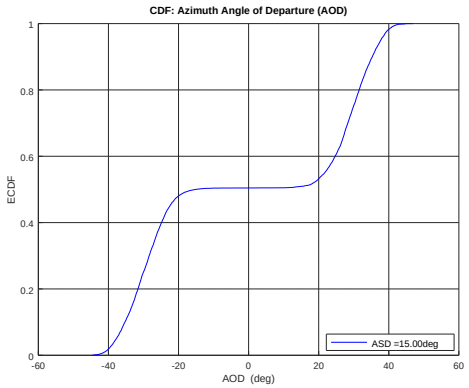

(c) AOD

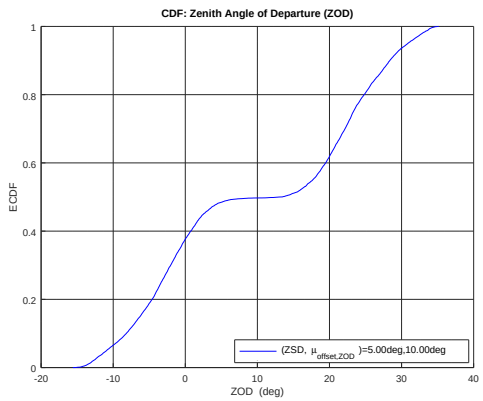

(d) ZOD

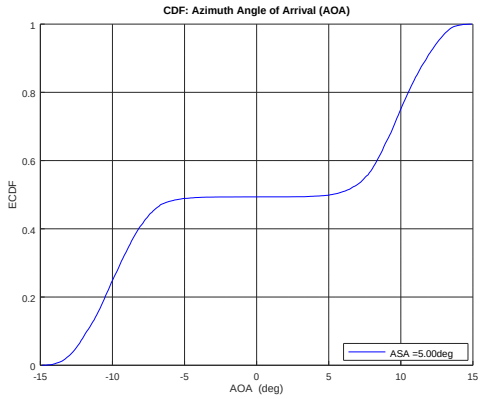

(e) AOA

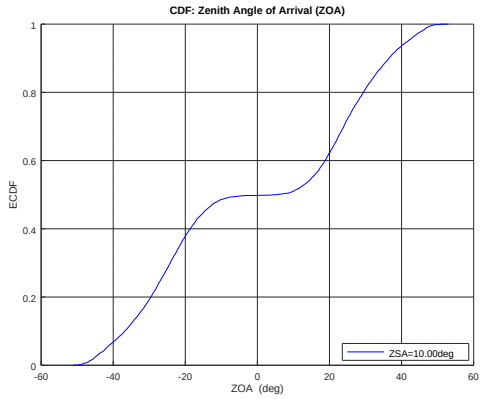

(f) ZOA

Figure 4.9: Empirical CDFs of the SSPs for the UMi-SC scenario.

4.2.5 Coefficient Generation

In the final stage of the SCM, initial phase ($\Phi_{n,m}$) for every ray of every cluster is drawn from a uniform distribution over the range $[-\pi, \pi]$ for every polarization combination: $(\theta\theta, \theta\phi, \phi\theta, \phi\phi)$. Next, the channel coefficient for each cluster and each receive and transmit antenna element pair (u, s) is computed as per Equations (7.5-28) & (7.5-29) in [1]. Here, $\mathbf{f}_{rx,u}^{NLOS}$ is the radiation field pattern for the arriving ray at the receiver with the azimuth angle $\phi_{n,m,AOA}$ and the zenith angle $\theta_{n,m,ZOA}$, similarly, $\mathbf{f}_{tx,s}^{NLOS}$ is the radiation field pattern for the departing ray at the transmitter with the azimuth angle $\phi_{n,m,AOD}$ and the zenith angle $\theta_{n,m,ZOD}$. The matrix $\mathbf{X}^{NLOS}$ accounts for the effect of the random initial phases $\Phi_{n,m}$ and polarization $\kappa_{n,m}$. The factors p_u^{NLOS}, p_s^{NLOS}, and $p_r x^{NLOS}(t)$ account for the phase shifts due to the receiver antenna element u, the transmit antenna element s, and Doppler due to UT mobility, respectively. Next, the coefficients are scaled with the pathloss and shadowing. Thus, the MIMO channel matrix at time t per cluster $\mathbf{H}_{u,s,n}(t)$ is obtained. The final MIMO channel matrix $\mathbf{H}_{u,s}(t) = \sum_n \mathbf{H}_{u,s,n}(t)$ with each entry as the channel coefficient for the receiver and transmitter antenna element pair (u, s).

4.2.6 Optional Components

The steps described in this section so far are essential to the generation of the channel matrix $\mathbf{H}_{u,s}(t)$ for a basic simulation. To support advanced simulations, specific models that can be integrated in the larger procedure are specified in the 3GPP technical report (Sec. 7.6 of [1]). To name a few, subprocedures to model the effect of: oxygen absorption, large bandwidth, spatially consistent mobility, and blockages are specified. In our implementation, we have implemented the *spatial consistency* and *blockage* components as UT mobility in the presence of blockages is at the center of our research work. The spatial consistency procedure is described in this Section and the blockage model is discussed in

Section 5.1.

Spatial Consistency: In the channel generation procedure described in the Sections 4.2.1 to 4.2.5, SSPs are sampled from distributions which have the LSPs (averages over several wavelengths) as input parameters. Although, the LSPs are not a function of the distance, they are correlated in distance to model the changes over several wavelengths. SSPs are independently generated per UT location and this may not be accurate enough for simulations requiring UT mobility. To ensure that channel coefficients are correlated in space (and time due to mobility), the technical report provides a method to update the SSPs (and hence the coefficients) at the current location of the UT based on the previous location. We implement spatial consistency using *Procedure A* in Sec. 7.6.3 of [1]. Here, cluster and ray specific random variables are correlated using the distance-decorrelation filter in eq. (4.1). These correlated values are used to generate the *initial* (at the first position of the UT i.e. $t = 0$) cluster delays, power contributions, and angular profiles. And, given the initial values, throughout the simulation, values at time t_k are updated based on those at time t_{k-1}.

Chapter 5

Parameterized Model for the 3GPP UMi-SC Link Blockage

Directionality at mm-wave can be realized in a smaller footprint, thanks to the shrinking antenna sizes at these frequencies. The downside however is the susceptibility of the beam to blockages due to objects in the surroundings. Advanced beamtracking measures may be able to preemptively prevent blockages, they may come at a great expense in terms of the overall latency and cost of processing. Broadly speaking, loss in the link quality due to such dynamic fading directly impacts several mechanisms such as beam setup, beamtracking, adaptive modulation, and coding [21]. Restoring the link quality may become prohibitively expensive, especially in applications that fall under the 3GPP use cases: ultra Reliable Low-Latency (uRLLc) and the massive Machine Type Communication (mMTC) [10].

The study and modeling of the mm-wave blockage phenomenon gained impetus during the development of the 60 GHz short range wireless standards of IEEE 802.15.3c [36] and IEEE 802.11ad [26]. One of the earlier studies in [37] shows that the frequency of link outages increases with an increase in the human density in an indoor setting. Today, real world measurements are being performed to quantify the effects of blockages for a larger range of the mm-wave spectrum in the indoor as well as the outdoor setting. For instance, in [38] it has been shown that at 15 GHz upto 10 dB of loss in link quality is observed due to passing vehicles on the street. The impact of human presence is assessed in [6]. Here, a blockage measurement at 73.5 GHz shows that a loss of over 40 dB is possible due to human presence around the transmitter and the receiver. Theoretical modeling of the blockage

phenomenon is done in [8], where random shape theory is employed to model the effect of randomly placed blockers in the environment. It is shown that the blockage effect can be mitigated by increasing the base station (BS) density. Several studies such as the ones listed above have contributed to the blockage modeling procedures specified in the 3GPP TR [1].

The blockage models in the 3GPP TR can be utilized to assess the instantaneous effect of blockages. This however comes with a significant simulation complexity as it requires the entire spatial channel model (SCM) to be implemented. In many studies, it is sufficient to have a simpler parameterized model that captures the effect of blockages. An example of such a study is found in [39]. Here, link quality is determined in the presence of blockages using a hierarchical blockage model. The link blockage probability is represented by a single model parameter.

To assess the link quality in a realistic setting, the model parameter p can be defined as the probability of link blockage in a certain direction. Such a parameter may be useful in case of a directional link that is modeled as a block fading channel, where the probability of a deep fade can be defined by the probability of link blockage in that direction. However, obtaining a realistic parameter that would hold for any environment is not possible. This is because, the blockage phenomenon heavily relies on the type of environment the link is operating in. Environmental features such as the layout geometry (streets, open areas), the location of the transmitter and the receiver, the number of potential blockers, their locations and their movement pattern cannot be consolidated under a single configuration.

The central contribution of this work is a simple model that captures the effect of the geometrically accurate Model B into a single parameter. Here, Model B is one of the (optional) blockage models specified in the the 3GPP TR [1] and is explained briefly in Section 5.1.2. Deriving such a parameter circumvents the complexity of simulating the entire SCM. The output parameter is a function of user input parameters such as

the dimensions of the street(s) in the UMi-SC layout, the blocker population, and the UT location. This is accomplished by obtaining an exponential fit based on extensive simulation for the empirical probability of blockage due humans and vehicles present on a street in the UMi-SC environment. The simulations are performed with modeling of blocker mobility for the UMi-SC scenario specified in the 3GPP TR [1]. The fit was calculated for a carrier frequency of 28 GHz and for a street that is 9 m wide and 170 m long. The proposed model holds for an ensemble of environments comprising of the street topologies described in Sections 5.2.3 and 5.2.4. We show that our parameterized model largely agrees with the simulation results.

This chapter is organized as follows. An overview of the blockage models specified in [1] is provided in Section 5.1 The proposed parameterized model of the probability of link blockage along with a procedure to calculate the same for an UMi-SC setting is presented in Section 5.2. The results are discussed in Section 5.3.

5.1 Blockage Modeling in 3GPP 38.901

The 3GPP TR 38.901 [1] describes a detailed procedure to generate a Multiple In Multiple Out (MIMO) spatial channel model for the frequency band of 0.5-100 GHz. The channel model is specified for bandwidths upto 10% of the carrier frequency with an upper limit of 2 GHz. A link comprises of one or more clusters, wherein a cluster is defined as a set of rays that are angularly close to each other in space. Mobility at one end of the link between the base station (BS) and the user terminal (UT) is supported.

The 3GPP study has identified blockages to be a potential source of channel degradation and has addressed this issue by specifying two procedures: Model A and Model B in Sec. 7.6.4 of [1]. These are optional add-on procedures that model the effect of blockages mainly due to humans and vehicles in the environment. Model A stochastically models the location

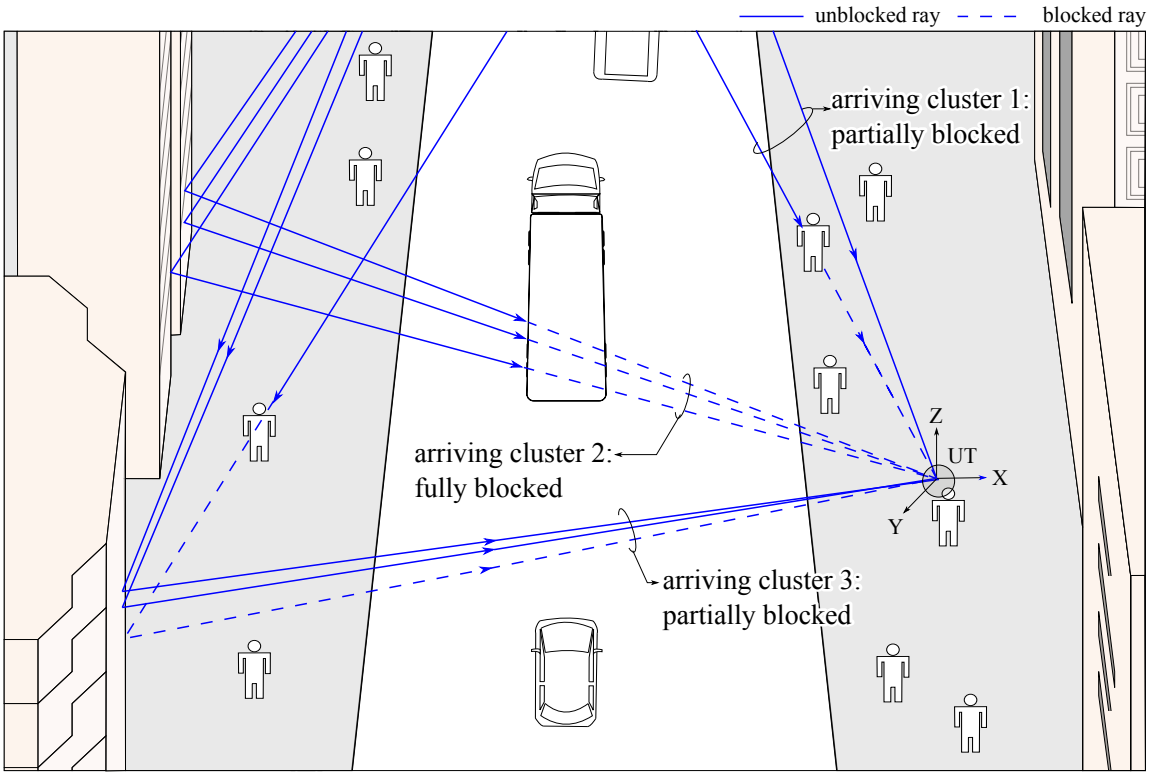

Figure 5.1: Schematic depicting the blockage phenomenon in the street canyon setting for the UMi-SC scenario.

of the blockers whereas Model B relies on the location of the blocker as set in the simulation. Both models focus on the arriving multipath components at the UT in both the azimuth (XY) and the zenith (ZY or ZX) plane. One of the deployment scenarios specified in the report is the UMi-SC scenario. An illustrative schematic of this scenario is shown in Fig. 5.1. Here, the BSs are typically installed below rooftop levels of the buildings and the UTs are found on the ground level. A street comprises of a sidewalk on each side with human traffic and a road with vehicular traffic. As shown, the UT (human carrying a cellphone) has established a link with three clusters arriving from a BS (not shown). Cluster 1 and 3 are partially blocked due to humans whereas cluster 2 is completely blocked by a vehicle. A detailed description of the blockage modeling procedures is beyond the scope of this work,

nevertheless, we briefly summarize the procedures, namely Model A and Model B in the following sections. The focus remains on Model B as it is used to model the approximate link blockage probability in this work.

5.1.1 Model A

Model A is a stochastic model that is suitable for use cases where the geography of the locality of the UT and the blockers is not considered. It assumes blockers that are randomly placed around the UT, but does not take into account the location of an arbitrary blocker while calculating the attenuation contribution to a cluster due to that blocker. On account of this assumption, the model is termed as generic and is thus computationally efficient relative to Model B which relies on geometric computation.

Central to the mechanism of this model is the probabilistic generation of angular blocking regions (in both the azimuth and the zenith plane) around the UT. If one or more arriving clusters fall into the blocking region, they are attenuated by an amount that depends on the type of the blockage. The model prescribes two types of blockages: self and non-self. As the name suggests, self-blocking (SB) is due to the human holding the UT and non-self-blocking (NSB) is due to humans and vehicles in the environment. There is a single SB region that attenuates the cluster by 30 dB if blocked. There can be multiple NSB regions, whose attenuation contribution is a function of the blocking region parameters (central angle and span), the carrier frequency, and the UT-blocker distance. In our implementation, if a cluster is found in multiple blocking regions, the attenuation contribution due to each is added in dB units. In this model, self-blocking type of blockages dominate as the angular span of the blocking region in this type is much larger than that in the non-self-blocking type. For example, for a UT held in the portrait mode under the UMi scenario assumption, the azimuth self-blocking region span is 120°, whereas the maximum

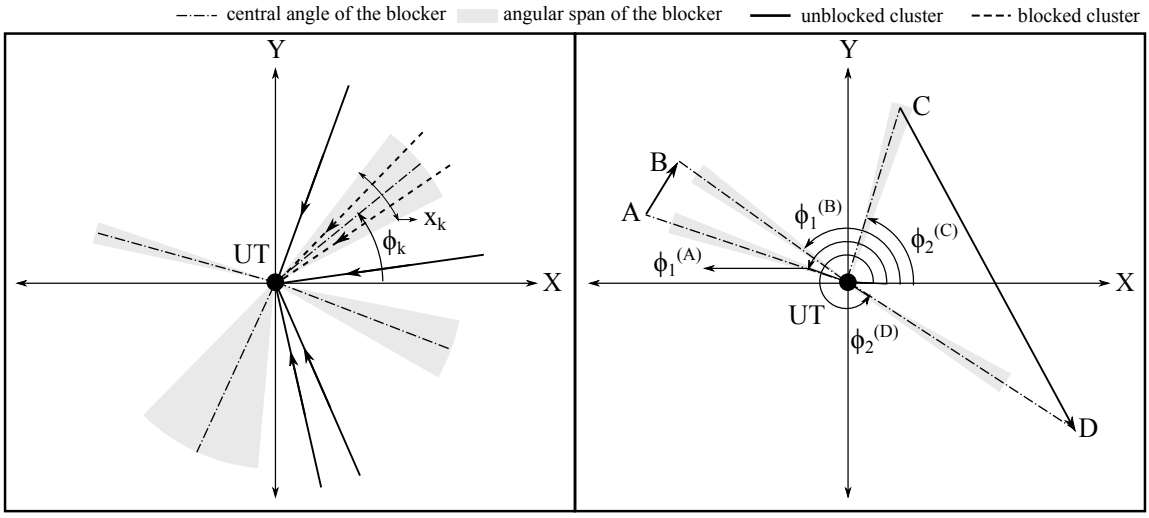

Figure 5.2: Diagram depicting the mechanism of Model A in the azimuth plane (top view). (a) general concept and (b) effect of blocker movement on the central angles.

span is 15° for the non-self-blocking region.

Remark 1. A change in the location of an arbitrary blocker must result in a proportional change in the central angle generated by the blocker at the two locations. One such example is shown in the diagram on the right in Fig. 5.2. Blocker 1 which moves over a smaller trajectory, namely, AB results in a smaller angular difference $|\phi_1^{(B)} - \phi_1^{(A)}|$. However, the difference is much larger in the case of Blocker 2. Thus, in a setting where blockers are mobile, sampling the central angles independent of the blocker's location may be inaccurate making the generation of angular regions spatially inconsistent. To make Model A spatially consistent, a subprocedure is specified in the 3GPP TR [1]. Here, the uniformly distributed blocking region central angles are correlated in space and time with the 2D autocorrelation function: $R(\Delta_x, \Delta_t) = e^{-\left(\frac{|\Delta_x|}{d_{corr}} + \frac{|\Delta_t|}{t_{corr}}\right)}$ where, d_{corr} is the correlation distance in meters and the correlation time $t_{corr} = (d_{corr}/v)$ seconds, with v being the blocker velocity in meters per second. It is worthwhile to note that due to the characterization by the velocity v of the blocker, blockers dropped in the simulation can be categorized by their velocity,

for example, humans moving at a walking speed of 4 km/h and vehicles moving at a speed of 25 km/h.

5.1.2 Model B

Model B is a deterministic geometric model. Here, the k^{th} $(1 \leq k \leq K)$ blocker is modeled as a rectangular screen with width w_k, height h_k, and center at coordinate (x_k, y_k, z_k). In contrast with Model A, where attenuation is computed per cluster, in Model B it is computed per ray of the cluster. A ray is blocked if it intersects the blocker screen in the azimuth or in the zenith plane. The attenuation due to a blocker is calculated using the double knife-edge diffraction (DKED) method [6]. The attenuation contribution due to a blocker is a function of the UT location (and BS location if the link is line of sight (LOS)), the carrier frequency, the blocker location and its dimensions. Due to its inherent dependence on the location of the blocker, this model is spatially and temporally consistent.

5.2 Link Blockage Probability: An Empirical Model

The main contribution of this work is the derivation of a model parameter that provides the approximate probability of blockage in a UMi-SC scenario. This parameter is a function of user input parameters such as the dimensions of the street(s) in the UMi-SC layout, the blocker population, and the UT location. The blockage mechanism is based on the procedure specified in Model B. The derivation is divided into two parts. In the first part, a geometric model that holds for a representative urban street canyon scenario is obtained. Specifically, an exponential fit for the empirical probability of blockage at a carrier frequency of 28 GHz and for a street that is 9 m wide and 170 m long is obtained. The second part extends this model to two topologies that are commonly found in an urban street canyon setting. We begin with the description of the experimental setup that

corresponds to the overall layout assumed. The exponential fit is then computed for a subset of this layout - a street.

5.2.1 Experimental Setup

To accurately model the blockage phenomenon, Model B relies on the location of the blocker, the dimensions of the blocker, and the location of the UT. A straightforward method to introduce blockers in the locality of the UT is to randomly place them throughout the chosen layout and randomly move them around the UT to model mobility. However, such an assumption may result into unrealistic cases of population distribution in the layout. For instance, in the case of two types of blockers: human and vehicular, vehicles and pedestrians may share the same location. This is especially true of the UMi-SC scenario that is characterized by automobile roads accompanied by sidewalks. As an example of the UMi-SC scenario, we select the Gramercy Park locality in New York City. Fig. 5.3 shows the map of the locality and its simulated counterpart. The placement and movement of blockers is designed to closely follow the layout. Blocker presence is constrained to the street and the park.

A schematic of an example of human and vehicular blocker placement for an arbitrary street in the setup is shown in Fig. 5.4. A street comprises of a road (one-way vehicular traffic) and a sidewalk on each side of the road (two-way human traffic on each sidewalk). The dimensions of the layout are considered to be simulation parameters. Human blockers are placed only on the sidewalk and vehicles are placed only on the road. Appropriate inter-blocker distances have been set to avoid overlapping in both the vertical and horizontal dimensions. Inter-blocker distances are shown in Fig. 5.4 as shaded rectangles around the blockers. Consequently, a sidewalk is divided into lanes, where the number of lanes depends on the inter-blocker distances and the width W_{sw} of the sidewalk. Irrespective

(a)

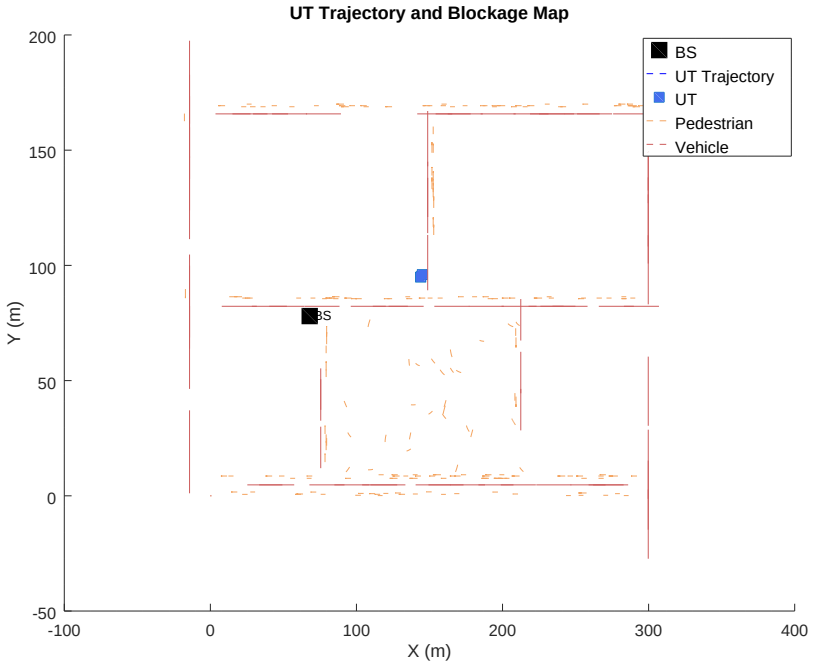

(b)

Figure 5.3: Representative layout for the UMi-SC scenario. (a) Map of the Gramercy Park locality in New York City (Courtesy of openstreetmap.org). (b) Example of the simulated blocker placement in the Gramercy Park locality.

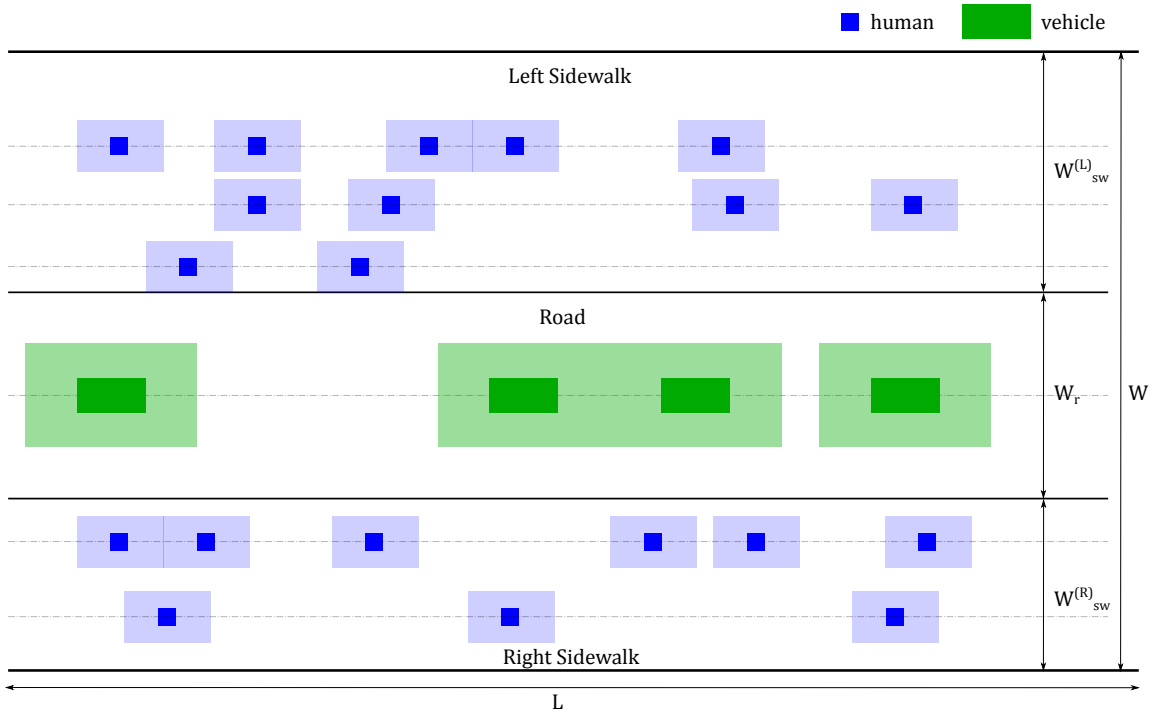

Figure 5.4: An example placement of human and vehicular blockers on the street. Solid rectangles in the simulated map represent the blocker and the shaded area around a rectangle is the space specified to avoid overlapping blockers.

of its width, a road is assumed to have a single lane along which vehicles travel. Blocker trajectories are modeled as random walks along the length with some deviation along the width. However, the deviation along the width is set to a value that does not result in a lane change for any blocker. The blocker population is controlled by the blocker density which is measured in the units of humans per unit area and vehicles per unit length of the street. Owing to the set dimensions of the layout and the constraints on overlapping blockers, the density values have an upper bound, making the blocker population metric realistic.

As the name *Street Canyon* suggests, a grid formed by streets that divide the geographical area into *blocks* is at the center of such an environmental layout. Accordingly, to

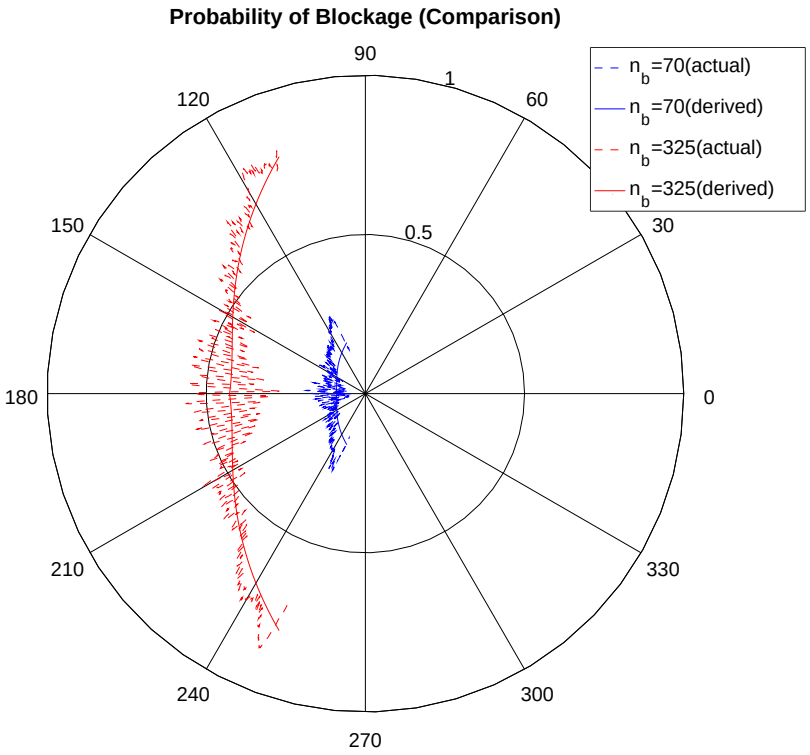

Figure 5.5: Empirical probability of blockage along Park Ave S for human and vehicular blockers. The effect of blockers that are beyond 50 m from the UT (in all directions) is ignored.

analyze the effect of blockages due to a street, we observe the empirical probability that an arriving ray is blocked in Fig. 5.5 for two values of the total blocker population n_b on a street. Here, the UT is placed at the coordinates $(0, 95)$ in the azimuth plane near Park Ave S (seen in Fig. 5.3) which is modeled as a one-way street with human and vehicular blockers. To assess the effect due to a single street, blockers are set to be present only on Park Ave S. Note that, as a consequence of having inter-blocker distances to avoid overlapping of blockers as described in Section 5.2.1, a street in the experimental setup is divided into several grids. As a consequence, blocker locations are spatially quantized. To eliminate the effect of quantization without loss of generality, the data in Fig. 5.5 is

filtered using a moving average filter with a length that is a function of the spatial grid resolution set for the experiment.

Remark 2. For the probability values seen in Fig. 5.5, blockers are present throughout the Gramercy Park locality. However, due to the proximity to the street under consideration, only blockers from the street have an influence on the channel quality of the UT.

In the following we propose a method to determine the approximate probability of link blockage for an arbitrary link set in the UMi-SC scenario, that complies with Model B. The modeling of the blockage effect in the UMi-SC scenario is accomplished in two steps: capturing the effect due to an arbitrary street in the neighborhood of the UT and extending the result to multiple streets that may introduce blockages for the UT.

5.2.2 Single-street Model

In the first step, we generalize the observation in Remark 2 to a model termed as the Single-street Model (SSM) as follows. Let d be the perpendicular distance from the UT to the street under consideration. Consider a sphere of radius d_I m centered at the UT location. As noted in Sec. 7.6.4.2 of [1], blocking effect diminishes with increasing distance. Thus, we assume that, at any given time, the effect of blockers outside the sphere is negligible and is ignored. To account for the contribution to the probability of blockage, we assume that rays arrive only from the direction of the street as seen by the UT. The number of rays reflected from the building structure close to the UT, arriving from the street side, is considered to be negligible. The azimuth plane geometry (2D) of the SSM is shown in Fig. 5.6. The azimuth angle extended by the center of the street as seen by the UT is denoted by δ. Similarly, the angles extended by the right and the left ends of the street onto the

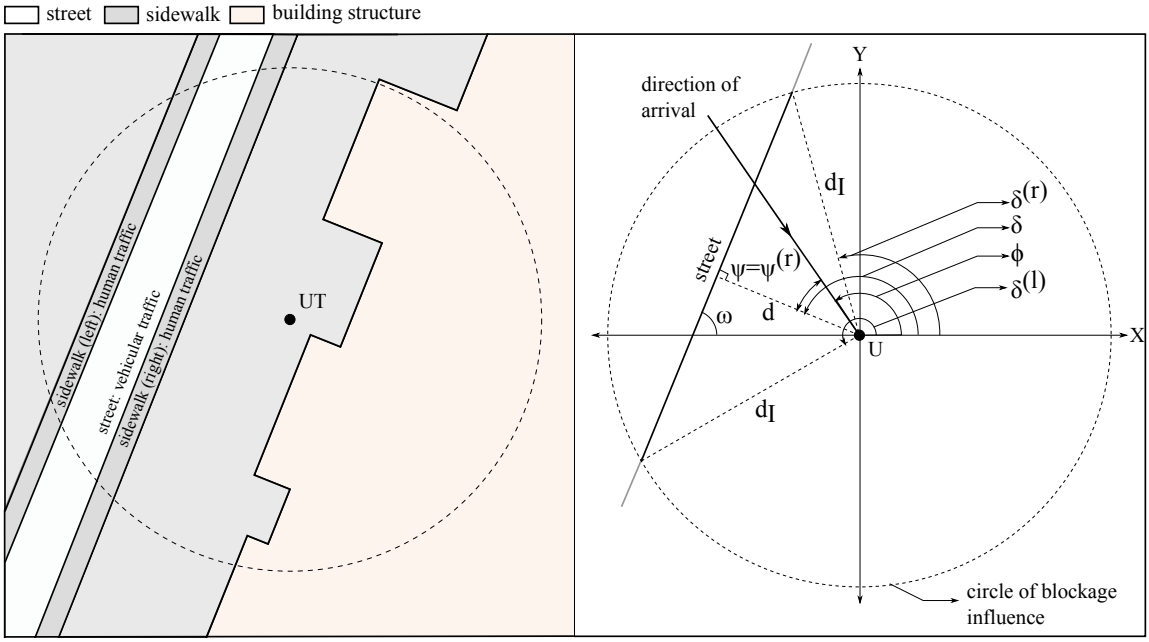

Figure 5.6: Schematic (left) and the corresponding geometrical diagram (right) of the SSM.

UT are denoted by $\delta^{(r)}$ and $\delta^{(\ell)}$, respectively. Thus, we have,

$$\psi = \begin{cases} \psi^{(r)} & \text{if } \delta^{(r)} \leq \phi < \delta \\ \psi^{(\ell)} & \text{if } \delta \leq \phi \leq \delta^{(\ell)} \end{cases} \tag{5.1}$$

where, $\psi^{(r)} = \delta - \phi$ and $\psi^{(\ell)} = \phi - \delta$ with ϕ being the direction of arrival. Let the values of ψ be the realization of the random variable Ψ. Then the probability of the blockage event B as a function of Ψ is given by,

$$Pr\{B|\Psi = \psi\} = \begin{cases} \left(c_1 e^{\alpha_1 \psi} + c_2 e^{\alpha_2 \psi}\right) n_b, & 0 \leq \psi \leq |\phi - \delta| \\ 0, & \text{o.w.} \end{cases} \tag{5.2}$$

where, $c_1, c_2, \alpha_1,$ and α_2 are the parameters that define the two-term exponential fit for the empirical probability of blockage. The blocker population $n_b = \left\lfloor \left[(\rho_h^{(L)} + \rho_h^{(R)}) W_{sw} + \rho_v \right] L \right\rfloor$ with $\rho_h^{(L(R))}$ being the human density per square meter on the left(right) sidewalk of the

street, ρ_v being the vehicular density per meter on the road, and L being the length in meters of the street in the UT's circle of blockage influence.

To derive the overall probability of blockage due to a street in the vicinity of the UT, we note that the directional probability given in (5.2) is symmetric around the center of the street visible from the UT. Let us consider the left-half of the street, for which we have, $\Psi^{(\ell)} = \Phi - \delta$. Here, the values of $\psi^{(\ell)}$ and ϕ are the realizations of the random variables $\Psi^{(\ell)}$ and Φ, respectively. Assuming that $\Phi \sim \text{Uniform}(\delta, \delta^{(\ell)})$,

$$F_{\Psi^{(\ell)}}(\psi) = \begin{cases} 0, & \psi < 0 \\ \frac{\psi}{\delta^{(\ell)} - \delta}, & 0 \leq \psi \leq \delta^{(\ell)} - \delta \\ 1, & \psi > \delta^{(\ell)} - \delta \end{cases} \tag{5.3}$$

Thus, the probability of blockage due to a street is,

$$\begin{aligned} P_{SSM} &= 2 \int_0^{\delta^{(\ell)} - \delta} Pr\{B | \Psi^{(\ell)} = \psi\} f_{\Psi^{(\ell)}}(\psi) \mathrm{d}\psi \\ &= \frac{2 n_b}{\delta^{(\ell)} - \delta} \left[\frac{c_1}{\alpha_1} \left(e^{\alpha_1 (\delta^{(\ell)} - \delta)} - 1 \right) \right. \\ &\qquad \left. + \frac{c_2}{\alpha_2} \left(e^{\alpha_2 (\delta^{(\ell)} - \delta)} - 1 \right) \right] \end{aligned} \tag{5.4}$$

5.2.3 Topology-I

The SSM model can be extended to a general case where the UT under consideration sees multiple streets inside its circle of blockage influence. One such scenario is depicted in Fig. 5.7. As the blocking phenomenon per street is independent of each other, the probability of blockage is computed separately for each street. Further, the overall probability of blockage for a particular direction of ray arrival can then be expressed as the probability of the union of blockage events on all streets in the direction of ray arrival.

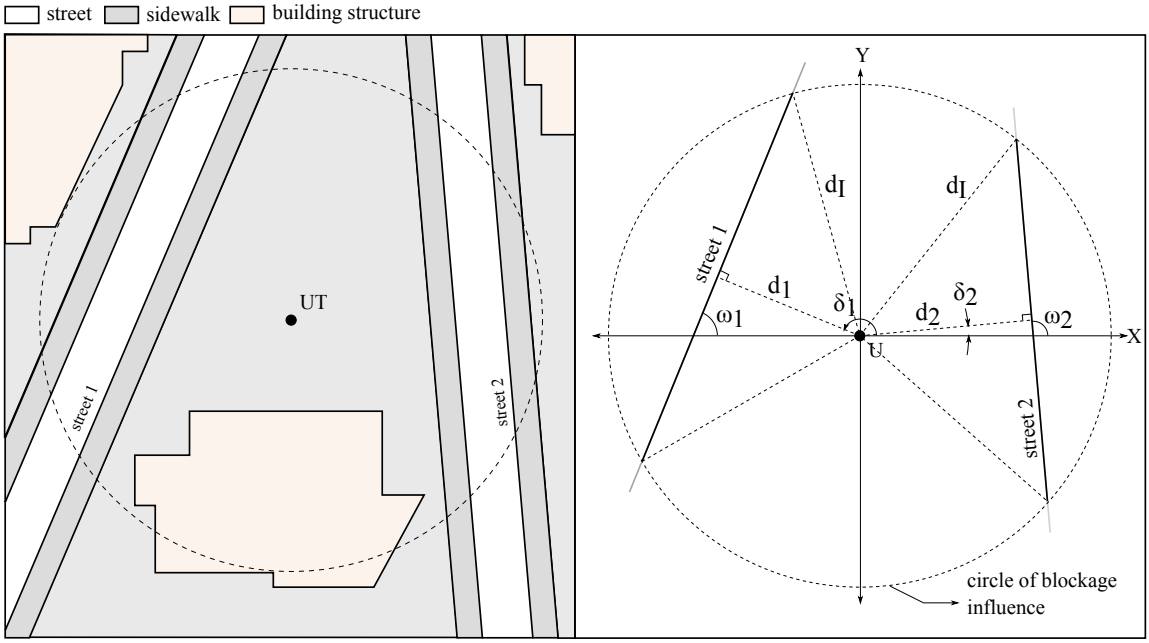

Figure 5.7: Schematic (left) and the corresponding geometrical diagram (right) of Topology-I.

5.2.4 Topology-II

The impact of the secondary street on the blockages caused to the UT can be quantified by the angles extended by the length of that street visible from the UT. Let us denote the angles as $\delta_{s,e}^{(1)}$ and $\delta_{s,e}^{(2)}$ as shown in Fig. 5.8. Then we have,

$$\delta_{s,e}^{(1)} = \delta_s - \arctan\left(\frac{d_s}{d_p}\right) \tag{5.5}$$

$$\delta_{s,e}^{(2)} = \delta_s - \arctan\left(\frac{d_s}{w_p + d_p}\right) \tag{5.6}$$

Thus, the probability of blockage due to a secondary street can be given as,

$$\begin{aligned} P_s &= \int_0^{\delta_{s,e}^{(1)}-\delta_{s,e}^{(2)}} Pr\{B|\Psi^{(\ell)}=\psi\} f_{\Psi^{(\ell)}}(\psi)\mathrm{d}\psi \\ &= \frac{n_b}{\delta_{s,e}^{(1)}-\delta_{s,e}^{(2)}} \left[\frac{c_1}{\alpha_1} \left(e^{\alpha_1(\delta_{s,e}^{(1)}-\delta_{s,e}^{(2)})} - 1 \right) \right. \\ &\qquad \left. + \frac{c_2}{\alpha_2} \left(e^{\alpha_2(\delta_{s,e}^{(1)}-\delta_{s,e}^{(2)})} - 1 \right) \right] \end{aligned} \tag{5.7}$$

The procedure to determine the union probability of blockage for an environment comprising of the topologies discussed above is summarized in Algorithm 1. The algorithm calculates the blockage probability due to primary and secondary streets. Here, $\mathcal{S}$ is the index set of streets in the chosen layout. For example, the Gramercy Park layout in Fig. 5.3, $\mathcal{S} = \{1, 2, 3, 4, 5, 6, 7\}$. And it is assumed that, the UT is dropped at the location U. Without loss of generality, let $W_{sw}^{(L)} = W_{sw}^{(R)} = W_{sw}$ thus we have, $W = W_r + 2W_{sw}$. Parameters for the i^{th} street are subscripted with the street index i.

5.3 Results and Discussion

5.3.1 Model B

To provide an insight into the workings of Model B, we simulate a representative power delay profile (PDP). Here, blockers placed in the Gramercy Park layout with Model B for the UMi-SC NLOS scenario.

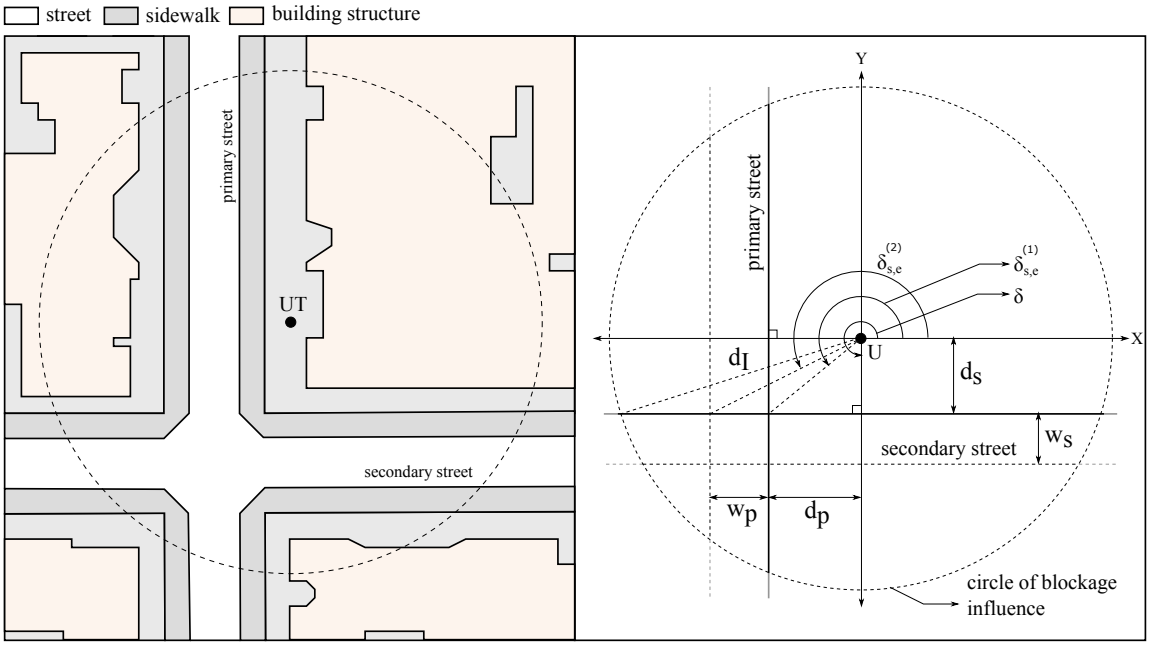

Figure 5.8: Schematic (left) and the corresponding geometrical diagram (right) of Topology-II.

Algorithm 1 Algorithm to find the probability of blockage.

procedure BLOCKAGE PROBABILITY($U, d_I, c_1, c_2, \alpha_1, \alpha_2, \mathcal{S}, \omega_i, \rho_{h,i}^{(L)}, \rho_{h,i}^{(R)}, \rho_{v,i}, W_{sw,i}, W_i$) ▷ $1 \le i \le |\mathcal{S}|$.
  $P_{sum} \leftarrow 0$
  $P_{prd} \leftarrow 1$
  for $i \in \mathcal{S}$ **do**
    $d_i \leftarrow$ perpendicular distance(U, street i)
    $L_i \leftarrow 2(d_I^2 - d_i^2)^{1/2}$
    if $d_i < d_I$ **then**
      $\delta_i \leftarrow \omega_i + \pi/2$
      $\delta_i^{(\ell)} \leftarrow cos^{-1}(d_i/d_I) + \delta_i$
      $n_{b,i} \leftarrow \left\lfloor \left[(\rho_{h,i}^{(L)} + \rho_{h,i}^{(R)}) W_{sw,i} + \rho_{v,i} \right] L_i \right\rfloor$
      $P_i \leftarrow \frac{2\, n_{b,i}}{\delta_i^{(\ell)} - \delta_i} \left[\frac{c_1}{\alpha_1} \left(e^{\alpha_1(\delta_i^{(\ell)} - \delta_i)} - 1 \right) + \frac{c_2}{\alpha_2} \left(e^{\alpha_2(\delta_i^{(\ell)} - \delta_i)} - 1 \right) \right]$
      $\mathcal{S} \leftarrow \mathcal{S} \setminus \{i\}$
      for $j \in \mathcal{S}$ **do**
        if $\left(d_i^2 + d_j^2 \right)^{(1/2)} < d_I$ **then**
          $L_j \leftarrow 2(d_I^2 - d_j^2)^{1/2}$
          $\delta_j \leftarrow \omega_j + \pi/2$
          $\delta_{s,e}^{(1)} \leftarrow \delta_j - \arctan(d_j/d_i)$
          $\delta_{s,e}^{(2)} \leftarrow \delta_j - \arctan(d_j/(W_i + d_i))$
          $n_{b,j} \leftarrow \left\lfloor \left[(\rho_{h,j}^{(L)} + \rho_{h,j}^{(R)}) W_{sw,j} + \rho_{v,j} \right] L_j \right\rfloor$
          $P_j \leftarrow \frac{n_{b,j}}{\delta_{s,e}^{(1)} - \delta_{s,e}^{(2)}} \left[\frac{c_1}{\alpha_1} \left(e^{\alpha_1(\delta_{s,e}^{(1)} - \delta_{s,e}^{(2)})} - 1 \right) + \frac{c_2}{\alpha_2} \left(e^{\alpha_2(\delta_{s,e}^{(1)} - \delta_{s,e}^{(2)})} - 1 \right) \right]$
          $P_{sum,i} \leftarrow P_{sum,i} + P_j$
          $P_{prd,i} \leftarrow P_{prd,i} \times P_j$
          $\mathcal{S} \leftarrow \mathcal{S} \setminus \{j\}$
        else
          $P_{sum,i} \leftarrow 0$
          $P_{prd,i} \leftarrow 1$
        end if
      end for
      $P_{sum} \leftarrow P_i + P_{sum,i}$
      $P_{prd} \leftarrow P_i \times P_{prd,i}$
    else
      $P_i \leftarrow 0$
    end if
  end for
  $P \leftarrow P_{sum} - P_{prd}$
  return P
end procedure

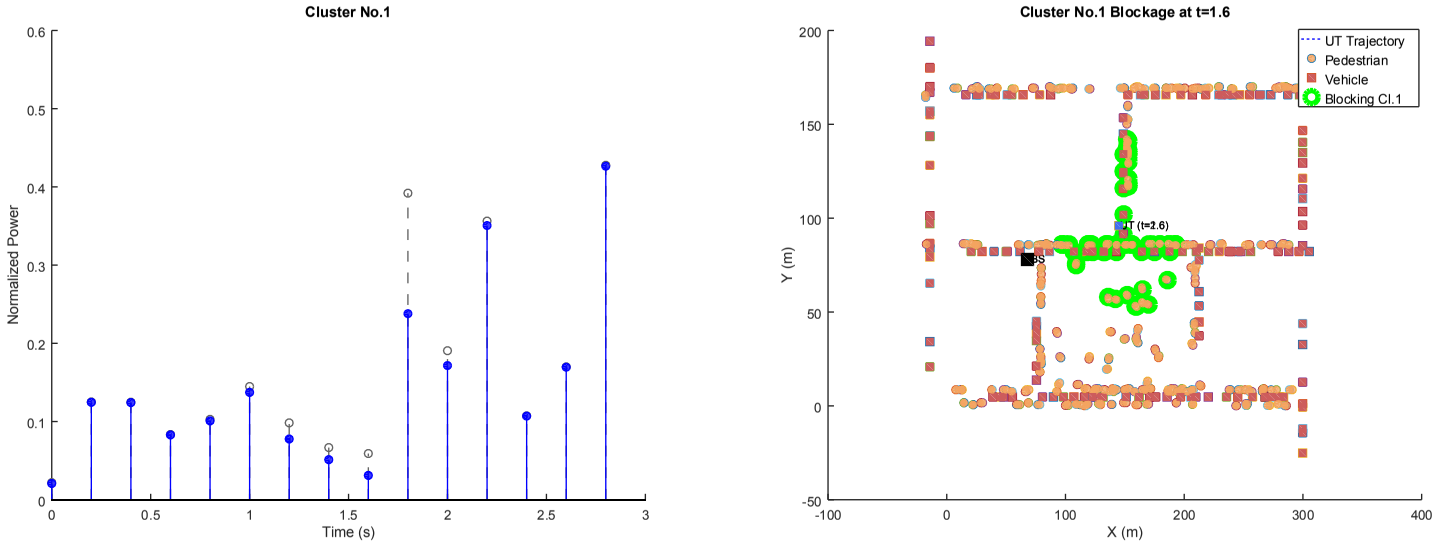

Figure 5.9: Effect of blockages on the PDP, NLOS case, as captured by Model B. Left: The PDP without blockages is depicted by the dashed grey plot and that with blockages by the blue plot for a representative cluster, namely cluster 1. Right: the corresponding 2D system map showing the blockers causing signal blockage for cluster 1 at time 1.6 s.

The human blocker velocity is set to 3.9 km/h. Vehicle speed on all streets is set to 28.8 km/h, except Park Ave and 3rd Ave, where it is set to 43.2 km/h and 36 km/h, respectively.

For this particular case, clusters 1,2,4,6,7,8,11, and 13 are affected by blockage. In Fig. 5.9 (left) significant attenuation is observed on Cluster 1 from time 1.2 to 2 s. On the right is the snapshot at time 1.6 s of blocker locations that are causing this attenuation. It is worthwhile to note that only blockers within a distance of 50 m from the UT are being considered. Attenuation due to blockage becomes more pervasive as this distance increases.

5.3.2 Link Blockage Probability

The two-term exponential approximation of the empirical probability of blockage for a given direction of arrival in (5.2) is defined by the parameters c_1, c_2, α_1, and α_2. The values of these parameters was determined based on Model B for a carrier frequency of 28 GHz. Fig. 5.10 shows comparison of the approximation with the empirical results for $\delta = 180°, \delta^{(r)} = 110°,$ and $\delta^{(\ell)} = 250°$. It is seen that our approximation largely follows the values that are derived from the Model B procedure in [1].

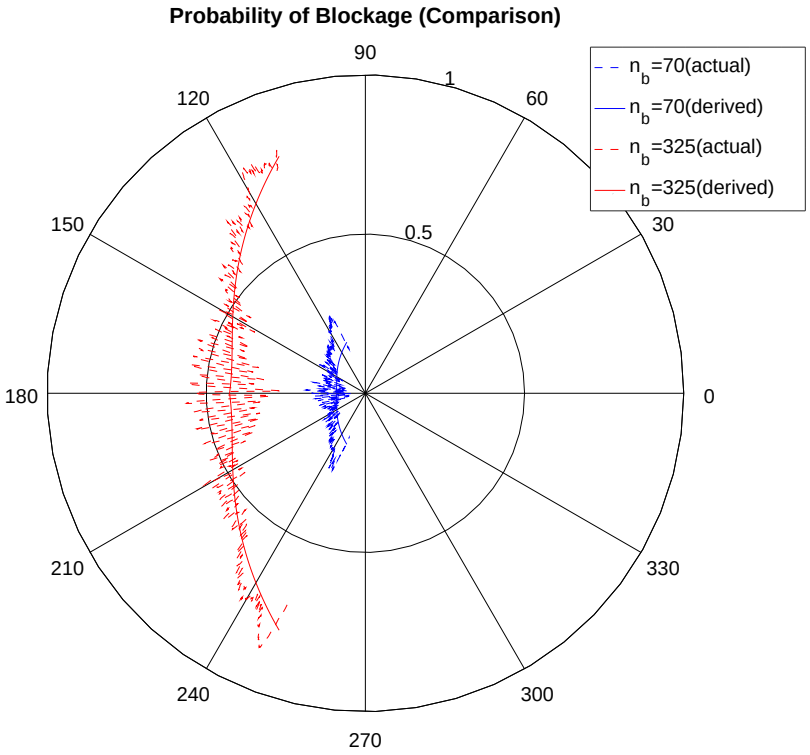

Figure 5.10: Comparison of the approximate and the actual values for the probability of blockage for the SSM. Here, for $n_b = 70$: $\rho_h^{(L)} = 0.1, \rho_h^{(R)} = 0.1, \rho_v = 0.014, W_{sw} = 2, L = 170$ and for $n_b = 325$: $\rho_h^{(L)} = 0.46, \rho_h^{(R)} = 0.0644, \rho_v = 2, W_{sw} = 170$. Here, $c_1 = 5.21 \times 10^{-4}$, $c_2 = 7.91 \times 10^{-4}$, $\alpha_1 = -0.0299$, and $\alpha_2 = 0.0157$.

Chapter 6

Conclusion and Future Work

The 5^{th} generation of communication systems hold the promise for several gigabits per second of data rates with ultra-low latencies. One of the main facilitators of this evolution is the migration from the microwave spectrum to the mm-wave spectrum. However, propagation in this spectrum comes with challenges such as increased path loss relative to the contemporary microwave spectrum, atmospheric absorption loss, and shadowing due to commonly found environmental objects.

Understanding the blockage phenomenon and remedying it is crucial to the success of 5G mm-wave deployments. The Open Area D2D environment assumed in this work is particularly prone to blockages owing to the lack of access point vantage (such as elevation). The 3GPP study item is a result of several valuable contributions from industry and academia. We provide an implementation of the 3GPP channel model for the UMi scenario which can be readily used by researchers and technology developers. We are hopeful that it serves to provide a result oriented insight into the stochastic and geometric channel generation procedure of the 3D SCM. The 3GPP study item specifies two models to assess the effect of blockages in mm-wave propagation on the link quality. The ready to use implementation can be used to perform location accurate blockage simulations in an urban grid environment for a range of parameters such as blocker size, blocker density, street size and so on. In addition to environmental factors, the study of 3GPP TR 38.901 under the real-world Open Area UMi-SC scenario helped understand the dependence on

practical issues such as beamforming accuracy. To have a tractable yet general enough blockage model we proposed a stochastic model that not only provides the probability of a LOS but also provides the attenuation as a function of the environment.

However, assessing the impact of blockages as specified in the 3GPP technical report comes with the cost of increased development time and processing complexity. To facilitate work where such a cost is infeasible, a parameterized model for the approximate probability of blockage for the 28 GHz UMi-SC environment is distilled out of the geometrically accurate blockage model, namely Model B. The probability of blockage can be evaluated for various instances of the UMi-SC environment since it is derived as a function of environmental parameters such as the layout dimensions and the blocker population. We hope that this is useful for studies where a single parameter (link blockage probability) based blockage model suffices.

The proposed stochastic blockage model quantifies the blockage effect in terms of a continuous metric: the signal attenuation that accounts for varying levels of blockage. The model holds for an open area mm-wave D2D environment. It is seen that a combination of factors such as the frequency of operation, the blocker size, and the size of the environment considered plays an important role in the degradation of link quality in the presence of random blockages. Further, the throughput analysis of the retransmission schemes shows that blockages in mm-wave D2D environments can severely impact the efficiency of such schemes. The model is utilized to provide a trade-off between the performance and a practical system design issue of beamforming misalignment, as a function of the blockage environment. The results clearly indicate that further work is required to investigate the impact of design factors such as the power allocation, the choice of the beam gains, and the choice of coding schemes that offer the best performance in terms of the overall throughput efficiency of the system while exploiting the diversity in the mm-wave channel.

Finally, we note some potential extensions of this work. In Chapter 3 we evaluate

the performance of retransmission schemes as a function of the blocker density and the misalignment error. Beamforming with the help of beam search commonly uses the beam sector sweep method. Here, the angular space around the transmitter and the receiver antenna is divided into angular sectors. Reference signals are transmitted and measured per sector and the pair of sectors (one at the transmitter and one at the receiver) with the best signal quality are chosen for beamforming. Refining the beam search by increasing the number of sectors can help reduce the misalignment accuracy. However, this will come with an overhead in terms of latency. Such a latency cost model if applied to the analysis in this work can give a trade-off between the beam setup time and the beamwidth (or gain) giving practically valuable insight into system design.

Further, the stochastic blockage model in Chapter 2 applies to environments where the blocker population density is uniform. This is owing to the homogeneous nature of the assumed 2D PPP. To model environments where blockers may not be uniformly spread across the geometry, a non-homogeneous PPP can be utilized.

Appendix A

Measure of Attenuation

In this work, the loss due to blockages is based on the double knife-edge diffraction (DKED) model provided in the ITU-R standard [22]. We assume a cylindrical blocker of width w that is at a distance d from the receiver. As per the spatial setup in Section 2.1, the transmitter is located on the edge of the CC of radius r. Applying the ITU-R DKED model to this setup we get the Fresnel zone geometry for the cylindrical blocker shown in Figure A.1.

Assumption 6 (Centered DKED)**.** The variation in the diffraction loss due to an offset between the center of the blocker C and the LOS (depicted by the segment TR in Fig. A.1) is ignored as it is negligible for $w << r$. Thus, we assume that the center of the cylindrical blocker C lies on the LOS TR between the transmitter and receiver.

The above assumption implies that the knife-edge diffraction (KED) loss contribution due to either side of the blocker is equal. Let $d_{R1} = d_{R2} := d_R$, $d_{T1} = d_{T2} := d_T$, $h_1 = h_2 := h$ and let λ denote the carrier wavelength in m. Further observing that $h = w/2$, the Fresnel zone parameter for KED at the upper edge is given by [22],

$$v = \frac{w}{2}\sqrt{\frac{2}{\lambda}\left(\frac{1}{d_T} + \frac{1}{d_R}\right)} \tag{A.1}$$

Assuming, $d_T \approx r - d$ and $d_R \approx d$, when $w << r$,

$$v \approx \frac{w}{2}\sqrt{\frac{2}{\lambda}\left(\frac{r}{d(r-d)}\right)} \tag{A.2}$$

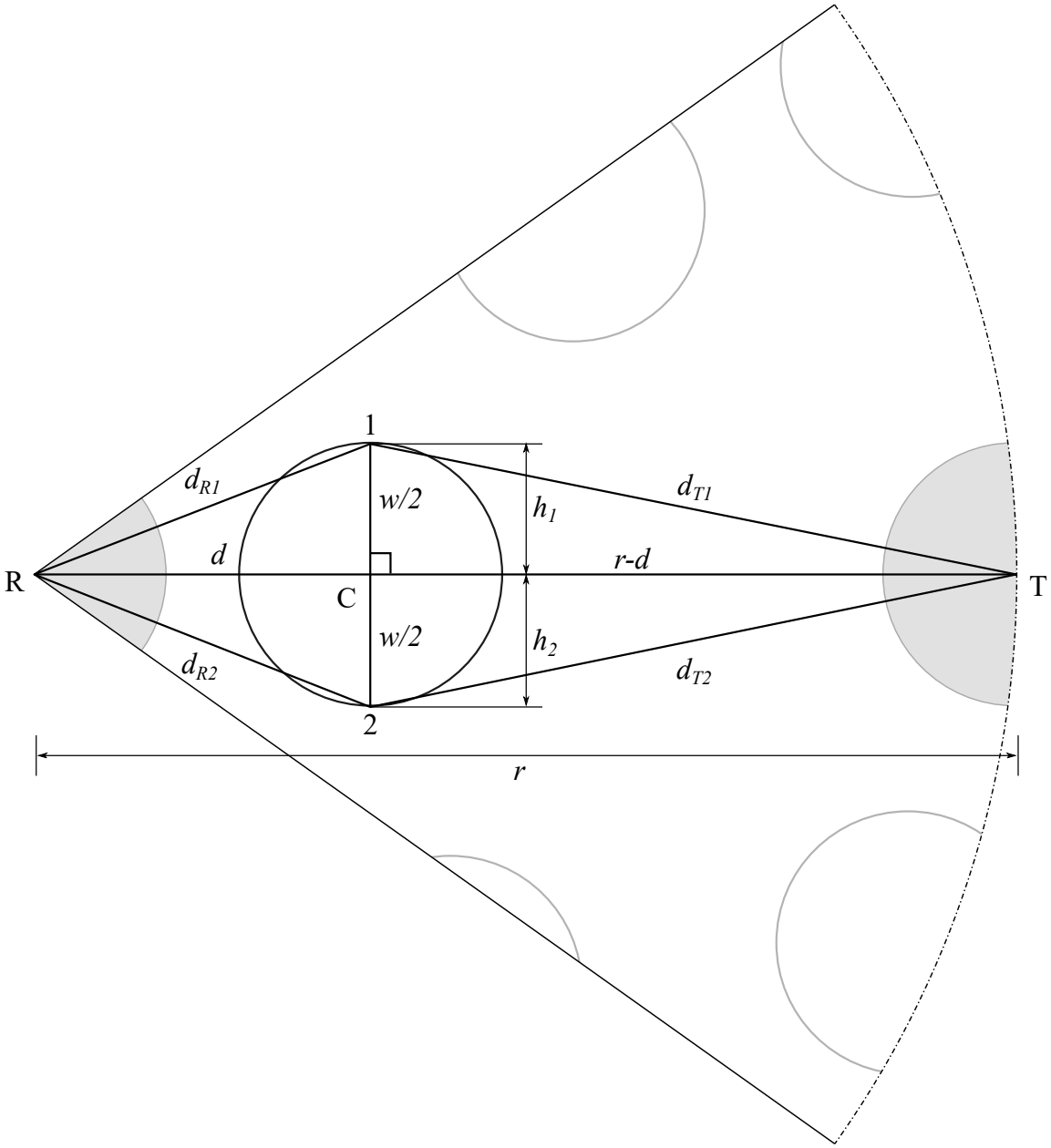

Figure A.1: Azimuth view of the DKED model geometry for the cylindrical blocker.

The KED loss at one edge of the blocker is given by,

$$j(v) = \frac{\sqrt{(v-0.1)^2+1}+v-0.1}{10^{-6.9/20}} \tag{A.3}$$

To maintain tractability of the overall model, we utilize a linear approximation of (A.3) given as, $j(v) \approx av$. It is observed that the minimum approximation error of $\approx 3\,\mathrm{dB}$ occurs at $a = 4.384$. Thus, the total KED loss due to the upper and the lower edge of the blocker $j_{av}(v)$ is given by the squared harmonic sum of the losses at each edge,

$$\frac{1}{j_{av}^2(v)} = \frac{1}{j_1^2(v)} + \frac{1}{j_2^2(v)} = \frac{2}{j^2(v)} = \frac{2}{a^2v^2}$$

where, in the above, $j_1(v) = j_2(v) = j(v)$. Thus,

$$j_{av}(v) = \frac{aw}{2}\sqrt{\frac{r}{\lambda d(r-d)}} \tag{A.4}$$

Thus, the attenuation $\zeta(r,d)$ is given as

$$\zeta(r,d) = \frac{1}{j_{av}(v)} = \frac{2\sqrt{\lambda}}{aw}\sqrt{\frac{d(r-d)}{r}} \tag{A.5}$$

The average attenuation for a blocker in the CC of radius r is

$$\begin{aligned}
\zeta(r) &= \int_{x=s}^{r} \frac{2\sqrt{\lambda}}{aw}\sqrt{\frac{x(r-x)}{r}} f_{D\,|\,R}(x\,|\,r)\,\mathrm{d}x \\
&\overset{(a)}{=} \int_{x=w}^{r} \frac{2\sqrt{\lambda}}{aw}\sqrt{\frac{x(r-x)}{r}} \frac{2x}{r^2-w^2}\,\mathrm{d}x \\
&= \frac{4\sqrt{\lambda}}{aw\sqrt{r}(r^2-w^2)} \int_{x=w}^{r} x\sqrt{x(r-x)}\,\mathrm{d}x
\end{aligned}$$

where, in (a) we have used (2.1) and set $s = w$. Thus,

$$\zeta(r) = \frac{\sqrt{\lambda}}{6aw\sqrt{r}(r^2-w^2)}\left[\frac{3\pi}{2} - r^3 3r^3 \arcsin(\sqrt{w/r}) - \sqrt{w(r-w)}(2w+r)(4w-3r)\right]$$

Further, maintaining the assumption that $w << r$ i.e. $r - w \approx r$, $r^2 - w^2 \approx r^2$, and $\arcsin(\sqrt{w/r}) \approx w/r$ we get,

$$\zeta(r) \approx \frac{1}{2a}\sqrt{\frac{\lambda}{w}}\left[1 + \frac{\pi}{2}\sqrt{\frac{r}{w}}\right]. \tag{A.6}$$

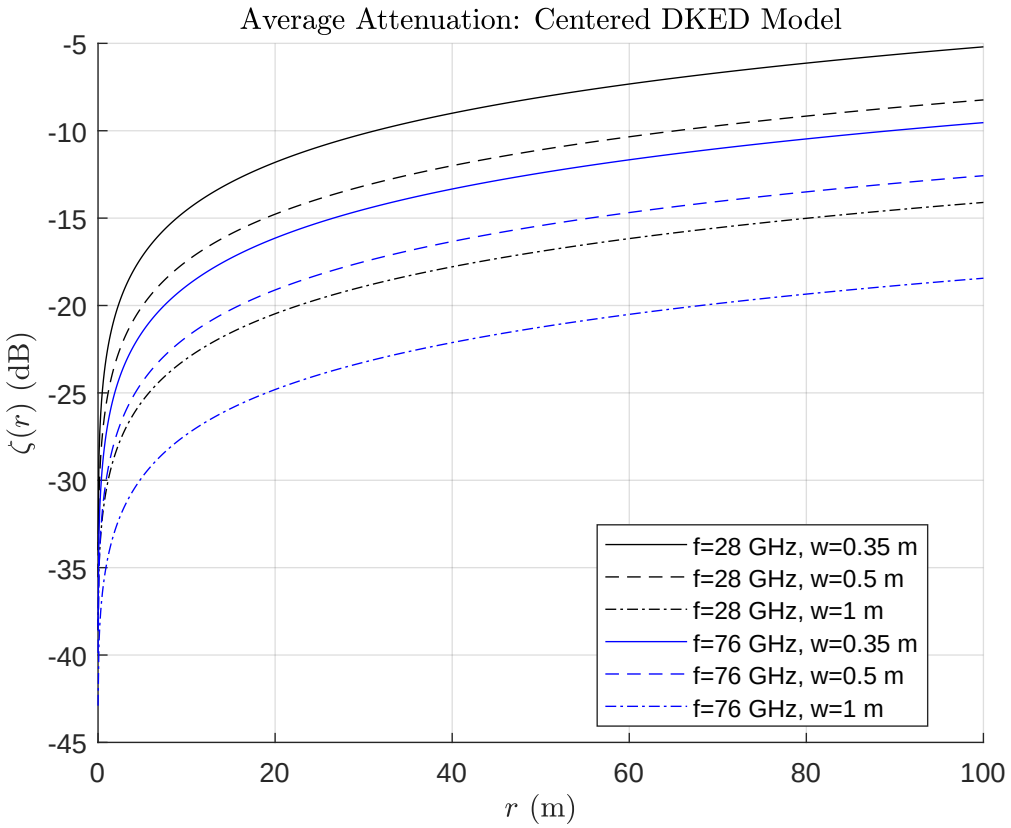

Figure A.2: Double knife-edge diffraction (DKED) model geometry for the cylindrical blocker.

As shown in Fig. A.2, the attenuation due to a cylindrical blocker increases with the size of the blocker and the carrier frequency. We can see that, as expected the attenuation increases (i.e. the blockage effect worsens) as the carrier frequency increases. This is owing to the reduction in the contribution of diffraction at 76 GHz relative to 28 GHz.

Appendix B

Hop Length Distribution

We consider the rectangular region with the area $W_X \times W_Y$ shown in Fig. 3.4 (right), $1 \leq W_X/W_Y \leq 3/2$. To determine the empirical distribution of the hop length, it is sufficient to determine the distribution between two arbitrary points of the assumed homogeneous 2D PPP inside the rectangular region. The empirical PDF is calculated for 10^6 values of the inter-point distance. In each trial, points are dropped inside the rectangular region of area $W_X \times W_Y$ according to a homogeneous 2D PPP of intensity ρ. Two points are randomly sampled without replacement and the distance between the sampled points is recorded. The empirical PDFs and their corresponding lognormal approximations are shown for various geography sizes (W_X, W_Y) in Fig. B.1. It is seen that the hop length $R_{\ell,i}$ of the i^{th} hop of the ℓ^{th} NLOS link, $1 \leq \ell \leq L$, can be approximated by a lognormal random variable whose support is truncated to the interval $(w, W_d]$, $W_d = \sqrt{W_X^2 + W_Y^2}$. Its mean $\theta_R = e^{\mu_R + \sigma_R^2/2}$ and variance $\delta_R = e^{2\mu_R + \sigma_R^2}\left(e^{\sigma_R^2} - 1\right)$. Where, μ_R and σ_R is the mean and variance of the underlying truncated normal distribution and are given as follows.

$$\mu_R = \mu_{R'} + \sigma_{R'}\left[\frac{\phi(\tilde{w}) - \phi(\tilde{W}_d)}{\Phi(\tilde{W}_d) - \Phi(\tilde{w})}\right] \tag{B.1}$$

$$\sigma_R^2 = \sigma_{R'}^2\left[1 + \frac{\tilde{w}\phi(\tilde{w}) - \tilde{W}_d\phi(\tilde{W}_d)}{\Phi(\tilde{W}_d) - \Phi(\tilde{w})} - \left(\frac{\phi(\tilde{w}) - \phi(\tilde{W}_d)}{\Phi(\tilde{W}_d) - \Phi(\tilde{w})}\right)^2\right] \tag{B.2}$$

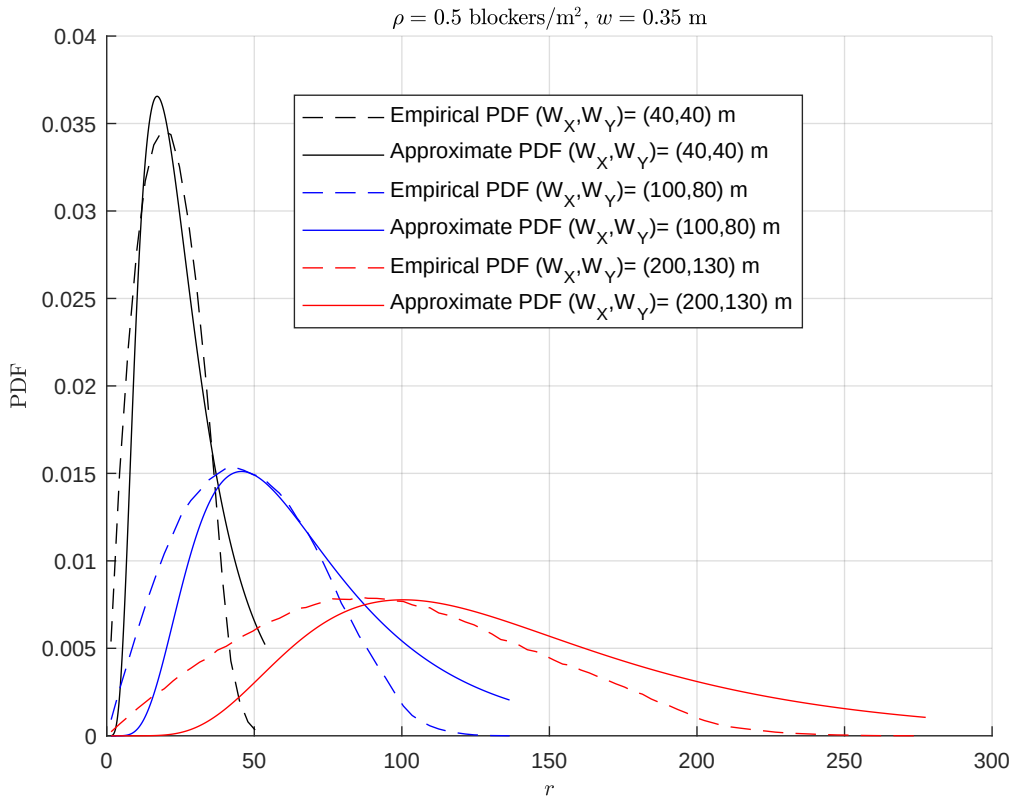

Figure B.1: Comparison of the empirical PDF of the inter-point distance with the corresponding lognormal approximation.

where, $\tilde{w} = \frac{\ln(w)-\mu_{R'}}{\sigma_{R'}}$, $\tilde{W}_d = \frac{\ln(W_d)-\mu_{R'}}{\sigma_{R'}}$. Here, $\mu_{R'} = \ln\left[\theta_{R'}\left(1+\frac{\delta_{R'}}{\theta^2_{R'}}\right)^{-1/2}\right]$ and $\sigma^2_{R'} = \ln\left(1+\frac{\delta_{R'}}{\theta^2_{R'}}\right)$ are the logarithmic mean and variance of a lognormal random variable $R' \in (0,\infty)$. The results in Fig. B.1 are plotted for $\theta_{R'} = \frac{W_d\sqrt{W_X/W_Y}}{2}$ and $\delta_{R'} = \frac{W_X^{3/2}W_Y^{1/2}}{5}$. The PDF of $R_{\ell,i}$ is given by (B.3).

$$f_{R_{\ell,i}}(r) = \begin{cases} \frac{e^{-\left[\ln(r)-\mu_R\right]^2/2\sigma_R^2}}{r\sigma_R\sqrt{2\pi}\left[\Phi\left(\frac{\ln(W_d)-\mu_R}{\sigma_R}\right)-\Phi\left(\frac{\ln(w)-\mu_R}{\sigma_R}\right)\right]} & w < r_{\ell,i} \leq W_d \\ 0 & \text{otherwise.} \end{cases} \tag{B.3}$$

Appendix C

Hop Attenuation

We begin by noting that, for $w << r$ and $s = w$, $\arcsin(w/2r) \approx w/2r$ and $\arcsin(w/2s) \approx 1/2$. Applying the above to (2.5) and using (2.7) we get,

$$\begin{aligned} f(r) &:= r^2 g(r)(1-\zeta(r)) \\ &\approx \frac{r^2 w}{8\pi r^2}\left[4r + 2(4r^2)^{1/2} - 4s - 2(3s^2)^{1/2}\right] \\ &\qquad \times \left[1 - \frac{1}{2a}\sqrt{\frac{\lambda}{w}}\left[1 + \frac{\pi}{2}\sqrt{\frac{r}{w}}\right]\right] \\ &\overset{(a)}{\approx} \left(\frac{2+\sqrt{3}}{16}\right)\frac{\sqrt{\lambda}w}{a} r^{1/2} + \left(\frac{w}{\pi} - \frac{\sqrt{\lambda w}}{2\pi a}\right) r \\ &\qquad + \left(\frac{2+\sqrt{3}}{4\pi}\right) w^{3/2}\left(\frac{\sqrt{\lambda}}{2a} - \sqrt{w}\right) \end{aligned}$$

where in (a), we have ignored higher than second order terms of r. This is because, the product of higher order terms of r with $\sqrt{\lambda}$ rapidly approaches zero with a small increase in r for mm-wave frequencies. This is especially true for mm-wave frequencies greater than 28 GHz. Thus,

$$\begin{aligned} \overline{A}(R_{\ell,i}) &\approx e^{-\rho_\ell \pi \left[1-\zeta(R_{\ell,i})\right] R_{\ell,i}^2 g(R_{\ell,i})} \\ &= e^{-\rho_\ell \pi f(R_{\ell,i})} \\ &= e^{-\rho_\ell \left(c_1 R_{\ell,i}^{1/2} + c_2 R_{\ell,i} + b\right)} \end{aligned} \tag{C.1}$$

where, $c_1 := \left(\frac{2+\sqrt{3}}{16}\right)\frac{\pi w\sqrt{\lambda}}{a}$, $c_2 := w - \frac{\sqrt{\lambda w}}{2a}$, and $b := \left(\frac{2+\sqrt{3}}{4}\right) w^{3/2}\left(\frac{\sqrt{\lambda}}{2a} - \sqrt{w}\right)$.

Appendix D

Link Length Distribution

From Appendix B, the length of the i^{th} hop of the ℓ^{th} link is modeled as a truncated Lognormal random variable with $R_{\ell,i} \sim \mathcal{LN}(\mu_R, \sigma_R^2)$ where, μ_R and σ_R^2 are given by (B.1) and (B.2), respectively.

Fact 2 (Lognormal Sum Approximation [40])**.** If $X = \sum_{j=1}^{n} X_j$ where, $X_j \sim \mathcal{LN}(\mu_j, \sigma_j), \forall j$ are independent lognormal, then the distribution of X can be approximately given by that of another lognormal random variable $\tilde{X}$ with parameters:

$$\sigma_{\tilde{X}}^2 = \ln\left[\frac{\sum_{j=1}^{n} e^{2\mu_j+\sigma_j^2}(e^{\sigma_j^2}-1)}{\left(\sum_{j=1}^{n} e^{\mu_j+\sigma_j^2/2}\right)^2}+1\right]$$

$$\mu_{\tilde{X}} = \ln\left(\sum_{j=1}^{n} e^{\mu_j+\sigma_j^2/2}\right) - \frac{\sigma_{\tilde{X}}^2}{2}$$

Using the above approximation, when $Q_\ell = q_\ell$, $R(q_\ell) = \sum_{i=1}^{q_\ell} R_{\ell,i} \sim \mathcal{LN}(\mu_R(q_\ell), \sigma_R^2(q_\ell))$ where,

$$\begin{aligned}\sigma_R^2(q_\ell) &= \ln\left[\frac{\sum_{i=1}^{q_\ell} e^{2\mu_R+\sigma_R^2}(e^{\sigma_R^2}-1)}{\left(\sum_{i=1}^{q_\ell} e^{\mu_R+\sigma_R^2/2}\right)^2}+1\right] \\ &= \ln\left[\frac{q_\ell e^{2\mu_R+\sigma_R^2}(e^{\sigma_R^2}-1)}{q_\ell^2\left(e^{\mu_R+\sigma_R^2/2}\right)^2}+1\right] \\ &= \ln\left(\frac{e^{\sigma_R^2}-1}{q_\ell}+1\right). \qquad \text{(D.1)}\end{aligned}$$

and

$$\begin{aligned}\mu_R(q_\ell) &= \ln\left(\sum_{i=1}^{q_\ell} e^{\mu_R+\sigma_R^2/2}\right) - \frac{\sigma_R^2(q_\ell)}{2} \\ &= \ln\left[q_\ell e^{\mu_R+\sigma_R^2/2} - \frac{1}{2}\ln\left(\frac{e^{\sigma_R^2}-1}{q_\ell}+1\right)\right] \\ &= \mu_R + \frac{\sigma_R^2}{2} + \ln\left[\left(\frac{q_\ell^3}{e^{\sigma_R^2}+q_\ell-1}\right)^{1/2}\right] \qquad \text{(D.2)}\end{aligned}$$

Appendix E

Expected Power Reflection Coefficient

The analysis in this work assumes that a blocker is composed of a lossy dielectric material. Electromagnetic wave incident on such a material is partly refracted into the material (absorption loss) and is partly reflected off the material (reflection loss) [25]. It is well known that a lossy dielectric can be characterized by a constant termed as its relative complex permittivity referred hereto as ξ. It is expressed as [25],

$$\xi = \xi_0 \xi_r - j\xi'. \tag{E.1}$$

In the above, $\xi_0 = 8.85 \times 10^{-12}$ F/m is the permittivity of free space and ξ_r is the permittivity of the lossy dielectric relative to that of a perfect (lossless) dielectric. And, $\xi' = \frac{\sigma}{2\pi f}$ where, σ is the conductivity of the material measured in Siemens/meter and f is the frequency of the electromagnetic wave.

The fraction of power incident at an angle θ_i on the dielectric surface is measured by the power reflection loss. It is defined separately for the cases of parallel ($R^2_{\parallel}(\theta_i)$) and perpendicular ($R^2_{\perp}(\theta_i)$) polarization [25] where,

$$R_{\parallel}(\theta_i) = \left| \frac{-\xi \cos\theta_i + \sqrt{\xi - \sin^2\theta_i}}{\xi \cos\theta_i + \sqrt{\xi - \sin^2\theta_i}} \right| \text{ and} \tag{E.2}$$

$$R_{\perp}(\theta_i) = \left| \frac{\cos\theta_i - \sqrt{\xi - \sin^2\theta_i}}{\cos\theta_i + \sqrt{\xi - \sin^2\theta_i}} \right| \tag{E.3}$$

Skin Model	ξ	$\beta_{\parallel}$	$\beta_{\perp}$
Gandhi [28]	$19.3 - j19.5$	0.3407	0.6528
Gabriel [41], [42]	$16.6 - j16.6$	0.3194	0.6314
Chahat (palm) [43]	$11.4 - j5.7$	0.2217	0.5222
Chahat (wrist/forearm) [43]	$16.6 - j9.4$	0.2734	0.5871
Alekseev (palm) [44]	$15.5 - j14.2$	0.3013	0.6133
Alekseev (forearm) [44]	$17.1 - j16.8$	0.3214	0.6338

Table E.1: Expected power reflection coefficient at 28 GHz for various skin models.

are the reflection loss coefficients for parallel and perpendicular polarization, respectively. To incorporate the loss due to reflection at each blocker in the stochastic geometry described in Section 2.1, we have the following assumption.

Assumption 7. We assume that the angle of incidence $\theta_i \in [0, \pi/2]$ at each reflection taking place in the system (Fig. 3.4 (left)) is random. It is denoted by the random variable $\Theta_i \sim \mathcal{U}(0, \pi/2)$, thus,

$$f_{\Theta_i}(x) = \begin{cases} \frac{2}{\pi} & 0 \leq x \leq \pi/2 \\ 0 & \text{otherwise.} \end{cases} \tag{E.4}$$

Thus, the expected power reflection coefficient $\beta_{\parallel}$ for the case of parallel polarization is given as,

$$\begin{aligned} \beta_{\parallel} &= \mathbb{E} R_{\parallel}^2(\theta_i) \\ &= \int_0^{\pi/2} R_{\parallel}^2(u) f_{\Theta_i}(u) \, \mathrm{d}u \\ &\overset{\text{(a)}}{=} \frac{2}{\pi} \int_0^{\pi/2} R_{\parallel}^2(u) \, \mathrm{d}u \end{aligned} \tag{E.5}$$

where, in (a) we have used (E.4). Similarly, $\beta_{\perp}$ can be calculated.

E.1 Reflection Loss due to Humans

In Table E.1, $\beta_{\parallel}$ and $\beta_{\perp}$ values are shown for the case where the lossy dielectric material is the human skin and the frequency of operation is 28 GHz. The table comprises of human skin models from various researchers that have been listed in [45].

Appendix F

High-Throughput FPGA QC-LDPC Decoder Architecture for 5G Wireless

This chapter presents a brief summary of related work on the architecture development for a class of LDPC codes on the Field Programmable Gate Array (FPGA) platform. This segment of the work served as a motivation towards considering practical issues such as processing latency et cetera for mm-wave system design. We begin the overview with an introduction to the application of LDPC codes in 5G NR. The high-level FPGA architecture is summarized later. Finally, we present two applications of the architecture which were able to deliver high-throughput performance.

Quasi-Cyclic LDPC codes have been chosen for the data plane in the 3GPP 5G NR [46]. It is well known that the structure offered by QC-LDPC codes [47] makes them amenable to time and space efficient decoder implementations relative to random LDPC codes. During the early stages of standardization of 3GPP 5G NR, in [2] we proposed scalable and reconfigurable FPGA decoder architecture for circulant-1 identity matrix construction based QC-LDPC codes.

Here we summarize the architecture along with two case studies with results that validate the proposed architecture. Since the QC-LDPC codes for 5G NR were not finalized at the time of this work, we chose a standard compliant code, with a throughput performance that well surpasses the requirement of the chosen standard. The proposed decoder architecture can be used for a wide range of circulant-1 identity construction based QC-LDPC

codes many of which have been accepted in several standards such as IEEE 802.11n/ac [48], IEEE 802.16e/m [49] and DVB [50].

Insightful work on high-throughput (order of Gb/s) BP-based QC-LDPC decoders is available, however, most of such works focus on an ASIC design [51], [52] which usually requires intricate customizations at the Register Transfer Level (RTL) level and expert knowledge of VLSI design. A sizeable subset of which caters to fully-parallel [53] or code-specific [54] architectures. From the point of view of an evolving research solution this is not an attractive option, especially for rapid-prototyping. In the relatively less explored area of FPGA-based implementation, impressive results have recently been presented in works such as [55], [56] and [57]. However, these are based on fully-parallel architectures which lack flexibility (code specific) and are limited to small block sizes (primarily due to the inhibiting routing congestion) as discussed in the informative overview in [58]. Since our case study is based on fully-automated generation of the Hardware Description Language (HDL), a fair comparison is done with another state-of-the-art implementation [59] in [2]. Moreover, in this report, we provide without loss of generality, strategies to achieve a high-throughput FPGA-based architecture for a QC-LDPC code based on a circulant-1 identity matrix construction.

The algorithmic strategies were realized in hardware for our case study by the *FPGA IP* [60] compiler in *LabVIEW™ CSDS™* which translated the entire software-pipelined high-level language description into VHSIC Hardware Description Language (VHDL), enabling state-of-the-art rapid-prototyping. The scalability of the proposed architecture has been demonstrated in an application that achieves a throughput of 2.48Gb/s [61] on the NI USRP-2953R.

High-level FPGA-based Decoder Architecture: The high-level decoder architecture is shown in Fig. F.1. The ROM holds the LDPC code parameters such as the block length and the

maximum number of decoding iterations. The APP memory is initialized with the channel LLR values corresponding to all the variable nodes (VN). The barrel shifter operates on blocks of VNs of size $z \times f$, where f is the fixed-point word length used in the implementation for APP values. It circularly rotates the values to the right by using the shift values from the ROM, effectively implementing the connections between the check nodes (CN) and VNs. The cyclically shifted APP memory values and the corresponding CN message values for the block in question are fed to the node processing unit (NPU) arrays. Here, the global node processing units (GNPU) compute VN messages and the local node processing units (LNPU) compute the CN messages [2]. These messages are then stored back at their respective locations in the RAMs for processing the next block. Once the processing of all blocks within a layer is done, blocks in the next layer are processed as depicted by the *Block Processing* loop within the *Layer Processing* loop in Fig. F.1.

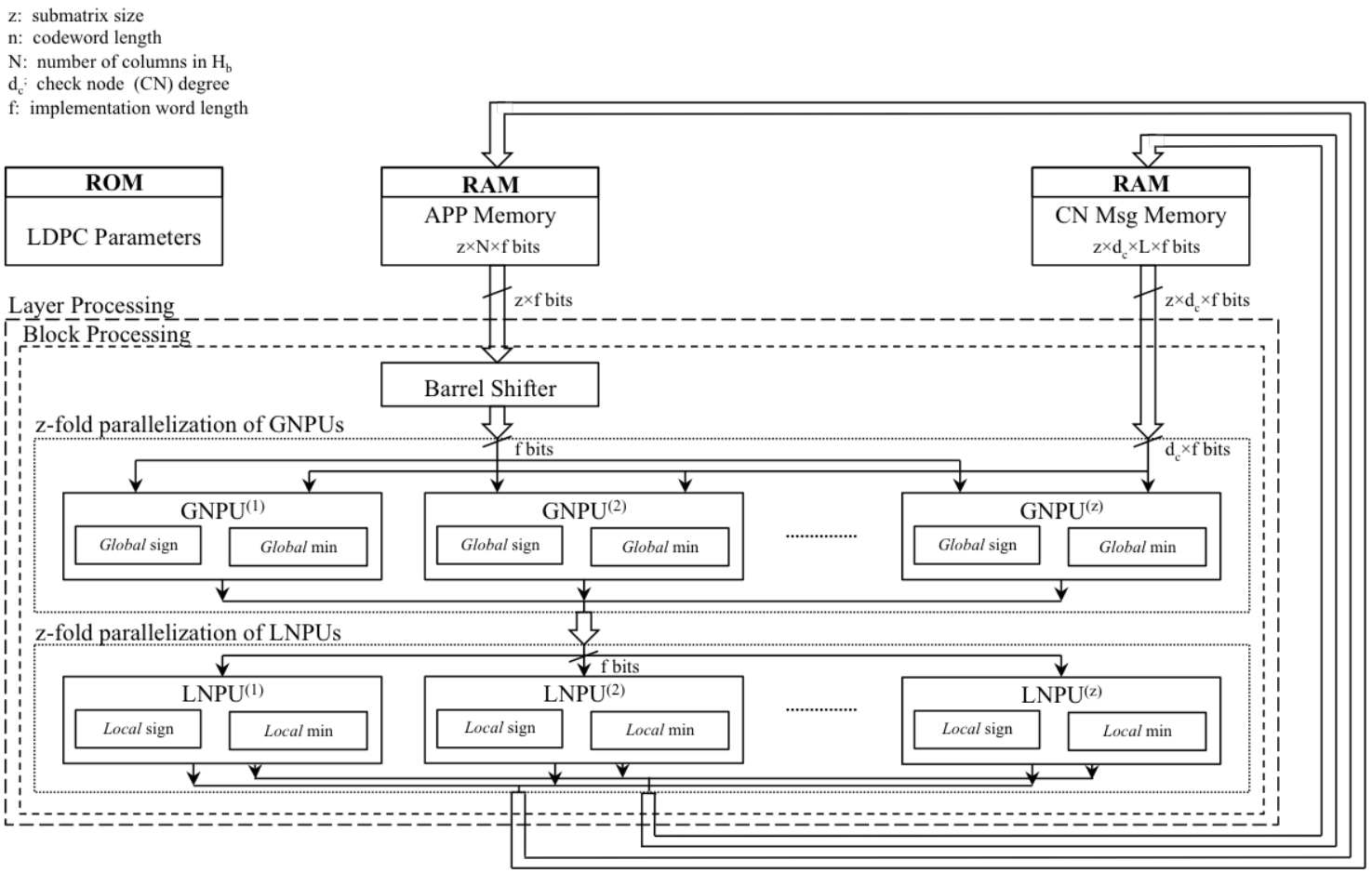

Figure F.1: High-level decoder architecture showing the z-fold parallelization of the NPUs with an emphasis on the splitting of the metric computation - GNPU and LNPU.

F.1 An IEEE 802.11n (2012) Compliant Decoder

This case study is based on the QC-LDPC code specified in the IEEE 802.11n (2012) standard [48]. For this code, $m_b \times n_b = 12 \times 24$, $z = 27$, 54 and 81 resulting in code lengths of $n = 24 \times z = 648$, 1296 and 1944 bits respectively. Our implementation supports the submatrix size of $z = 81$ and hence is capable of supporting all the block lengths for the rate $R = 1/2$ code.

The decoder algorithm for both versions was described using the *FPGA IP* compiler [60] in *LabVIEW™ CSDS™*. We would like to emphasize here that, both the versions were described in software at the algorithmic description level and not the HDL level. The algorithmic compiler translated the high-level description to an HDL description for the case study decoder implementation in approximately 3 minutes. The VHDL code was synthesized, placed and routed using the *Xilinx Vivado* compiler on the *Xilinx Kintex-7* FPGA available on the *NI PXIe-7975R* FPGA board.

Two versions of the decoder architecture namely $1x$ (non-pipelined version) and $2x$ (pipelined version) of depth two are implemented. The $2x$ version achieves an overall throughput of 608Mb/s at an operating frequency of 260MHz and a latency of 5.7μs with 4 decoding iterations. As seen in Table F.1, resource usage for the *2x* version is close to that of the *1x* version in spite of the $1.8x$ gain in throughput. The *FPGA IP* compiler chooses to use more FF for data storage in the *1x* version, while it uses more BRAM in *2x* version. A contemporary implementation of the *IEEE 802.11n* LDPC decoder on an FPGA (using high-level algorithmic description compiled to an HDL) shown in [59]. The decoder in [59] utilizes 2% of slice registers, 3% of slice LUTs and 20.9% of Block RAMs on the *Spartan-6 LX150T* FPGA with a comparable BER performance.

	1x	2x
Device	*Kintex-7k410t*	*Kintex-7k410t*
Throughput(Mb/s)	337	608
FF(%)	9.1	5.3
BRAM(%)	4.7	6.4
DSP48(%)	5.2	5.2
LUT(%)	8.7	8.2

Table F.1: LDPC Decoder IP FPGA Resource Utilization & Throughput on the Xilinx *Kintex-7 FPGA*.

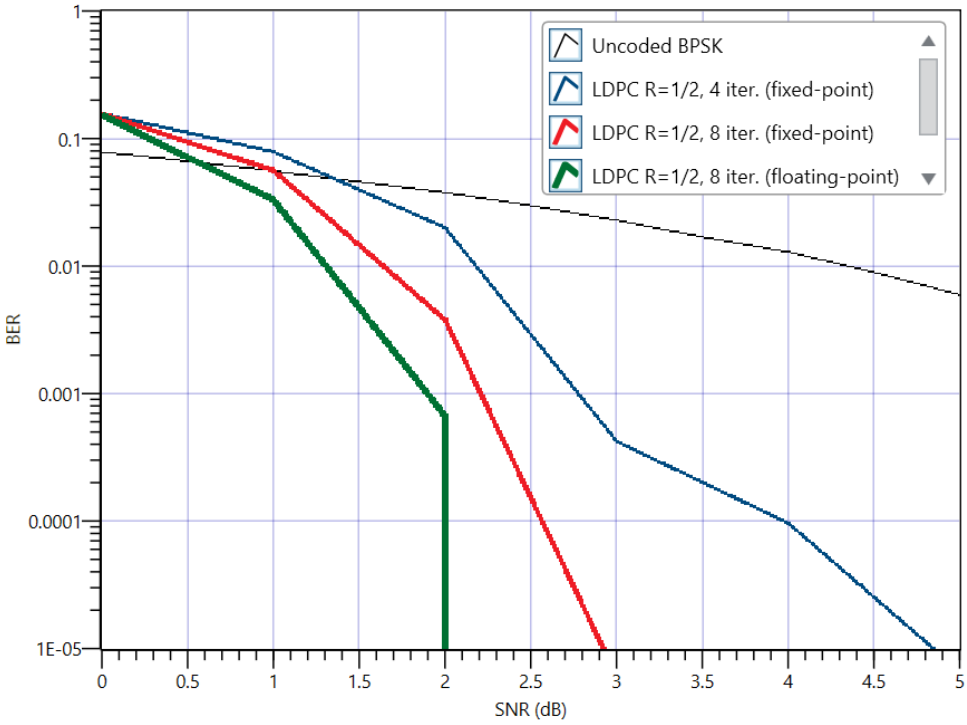

Figure F.2: Bit Error Rate (BER) performance comparison between uncoded BPSK (rightmost), rate=1/2 LDPC with 4 iterations using fixed-point data representation (second from right), rate=1/2 LDPC with 8 iterations using fixed-point data representation (third from right), rate=1/2 LDPC with 8 iterations using floating-point data representation (leftmost).

F.2 A 2.48Gb/s QC-LDPC Decoder on the NI USRP-2953R

In this section we present an application of the decoder architecture, a 2.48Gb/s FPGA-based QC-LDPC decoder implemented on the *NI USRP-2953R* (which has the *Xilinx Kintex7 (410t)* FPGA) using the *FPGA IP* compiler in *LabVIEW™ CSDS™*. Massive-parallelization was accomplished by employing 6 decoder cores in parallel without any modification at the HDL level. This application demonstrates the scalability of our decoder architecture [2] and the ability of the *LabVIEW™ CSDS™* tools to rapidly prototype high-level algorithmic description onto FPGA hardware. This application has been demonstrated in *IEEE GLOBECOM'14* where the QC-LDPC code for our case study was decoded with a throughput of 2.06 Gb/s. This throughput was achieved by using five decoder cores in parallel on the *Xilinx K7 (410t)* FPGA in the NI USRP-2953R.

F.2.1 Multi-core Decoder

On account of the scalability and reconfigurability of the decoder architecture in [2], it is possible to achieve high throughput by employing multiple decoder cores in parallel. Fig. F.3 shows the top-level multi-core decoder virtual instrument (VI), where 6 cores are deployed on a single *Xilinx Kintex7 FPGA (410t)*.

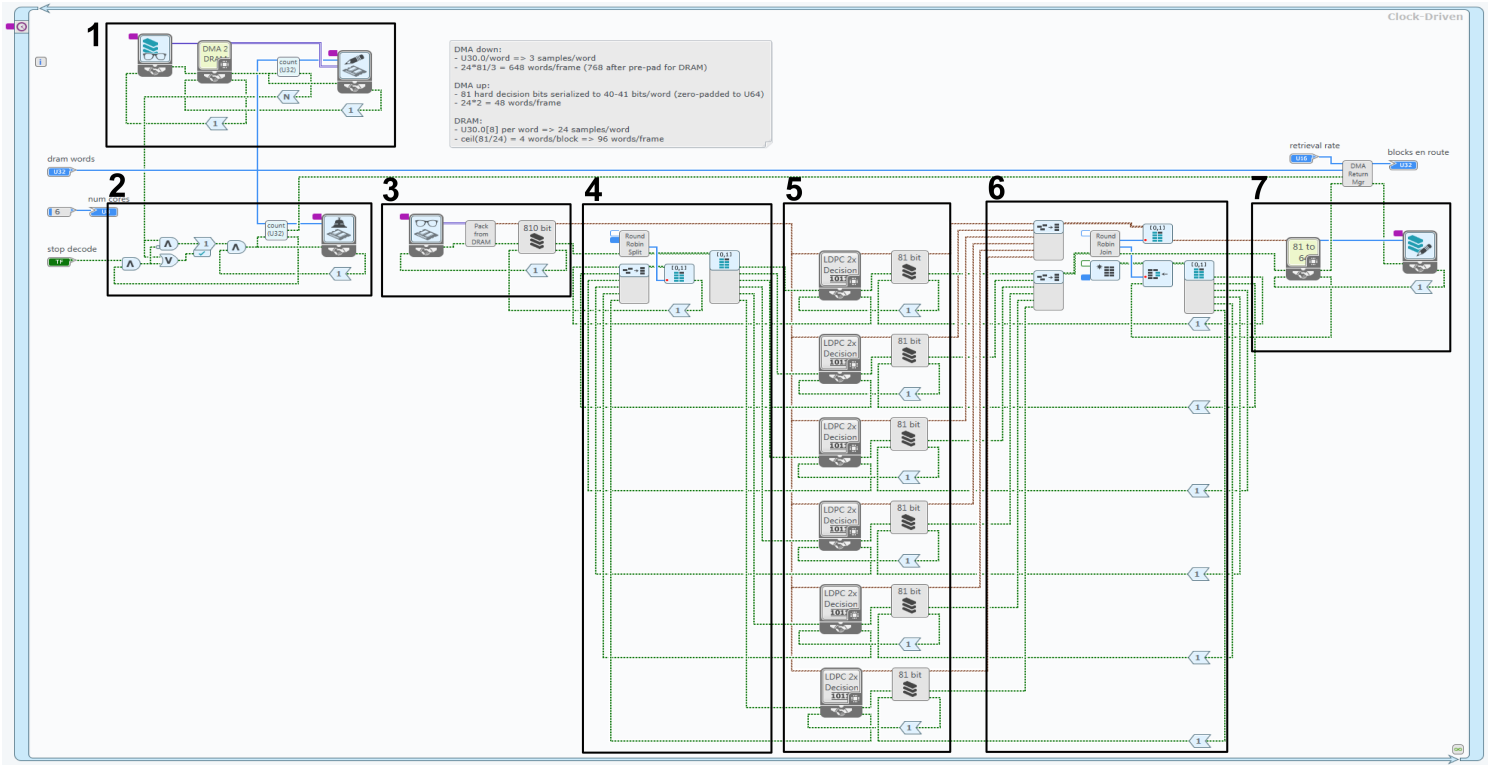

Figure F.3: Top-level VI describing the parallelization of the QC-LDPC decoder [2] on the *NI USRP-2953R* containing the Xilinx *Kintex7 (410t)* FPGA.

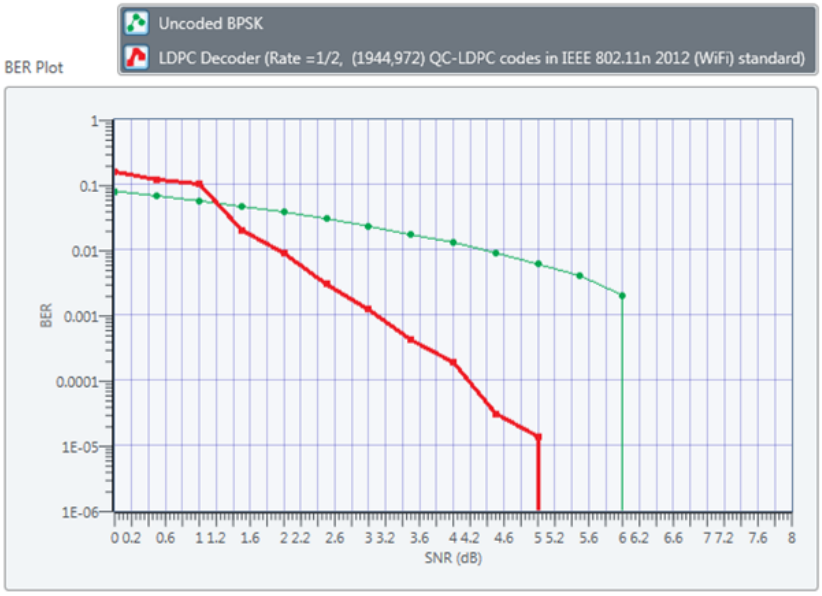

Figure F.4: Bit Error Rate (BER) performance comparison between uncoded BPSK (green) and the 2.48Gb/s, rate=1/2, QC-LDPC decoder (red) on the *NI USRP-2953R* containing the Xilinx *Kintex7 (410t)* FPGA.

F.2.2 Results

The 2.48Gb/s decoder was developed in stages, where at each stage a core was added (except for stage 3) and the performance and resource figures were recorded. The results of each stage are compared in Table F.2. The Bit Error Rate (BER) performance of the 2.48Gb/s version (with 6 cores) is shown in Fig. F.4.

Cores	**1**	**2**	**4**	**5**	**6**
Throughput (Mb/s)	420	830	1650	2060	2476
Clock Rate (MHz)	200	200	200	200	200
Time to VHDL (min)	2.08	2.08	2.08	2.02	2.04
Total Compile (min)	≈ 36	≈ 60	≈ 104	≈ 132	≈ 145
Total Slice (%)	28	44	77	85	97
LUT (%)	18	28	51	62	73
FF (%)	10	16	28	33	39
DSP (%)	5	11	21	26	32
BRAM (%)	11	18	31	38	44

Table F.2: Performance and resource utilization comparison for versions with varying number of cores of the QC-LDPC decoder implemented on the *NI USRP-2953R* containing the Xilinx *Kintex7 (410t)* FPGA.

References

[1] "3rd Generation Partnership Project; Technical Specification Group Radio Access Network; Study on channel model for frequencies from 0.5 to 100 GHz, V14.3.0," Dec 2017.

[2] S. Mhaske, H. Kee, T. Ly, A. Aziz, and P. Spasojevic, "High-throughput FPGA-based QC-LDPC decoder architecture," in *IEEE 82nd Veh. Technol. Conf., Fall*, Sep. 2015, pp. 1–5.

[3] "3rd Generation Partnership Project; Tech. Specification Group Radio Access Network; NR; NR and NG-RAN Overall Description; Stage 2, V15.7.0 Rel 15," Oct 2019.

[4] "3rd Generation Partnership Project; Tech. Specification Group Radio Access Network; Medium Access Control (MAC) Protocol Specification, V15.7.0 Rel 15," Oct 2019.

[5] "3rd Generation Partnership Project; Tech. Specification Group Radio Access Network; Radio Resource Control (RRC) Protocol Specification, V15.7.0 Rel 15," Oct 2019.

[6] G. R. MacCartney, S. Deng, S. Sun, and T. S. Rappaport, "Millimeter-Wave Human Blockage at 73 GHz with a Simple Double Knife-Edge Diffraction Model and Extension for Directional Antennas," in *2016 IEEE 84th Veh. Technol. Conf. (VTC-Fall)*, Sept 2016, pp. 1–6.

[7] M. Jacob, S. Priebe, A. Maltsev, A. Lomayev, V. Erceg, and T. Kürner, "A ray tracing based stochastic human blockage model for the ieee 802.11ad 60 ghz channel model," in *Proc. of the 5th European Conf. on Antennas and Propagation (EUCAP)*, Apr. 2011, pp. 3084–3088.

[8] T. Bai, R. Vaze, and R. W. Heath, "Using random shape theory to model blockage in random cellular networks," in *2012 Int. Conf. on Signal Process. and Commun. (SPCOM)*, Jul 2012, pp. 1–5.

[9] M. Gapeyenko, A. Samuylov, M. Gerasimenko, D. Moltchanov, S. Singh, E. Aryafar, S. Yeh, N. Himayat, S. Andreev, and Y. Koucheryavy, "Analysis of human-body blockage in urban millimeter-wave cellular communications," in *2016 IEEE Int. Conf. on Commun. (ICC)*, May 2016, pp. 1–7.

[10] "3rd Generation Partnership Project; Tech. Specification Group Radio Access Network; Study on Scenarios and Requirements for Next Generation Access Technol., V15.0.0," Jun 2018.

[11] R. I. Ansari, C. Chrysostomou, S. A. Hassan, M. Guizani, S. Mumtaz, J. Rodriguez, and J. J. P. C. Rodrigues, "5G D2D Networks: Techniques, Challenges, and Future Prospects," *IEEE Syst. J.*, pp. 1–15, 2018.

[12] J. Qiao, X. S. Shen, J. W. Mark, Q. Shen, Y. He, and L. Lei, "Enabling device-to-device communications in millimeter-wave 5G cellular networks," *IEEE Commun. Mag.*, vol. 53, no. 1, pp. 209–215, Jan. 2015.

[13] F. Boccardi, R. W. Heath, A. Lozano, T. L. Marzetta, and P. Popovski, "Five disruptive technology directions for 5G," *IEEE Commun. Mag.*, vol. 52, no. 2, pp. 74–80, Feb. 2014.

[14] "3rd Generation Partnership Project; Tech. Specification Group Radio Access Network; Study on LTE Device to Device Proximity Services; Radio Aspects, V12.0.1," Mar 2014.

[15] "3rd Generation Partnership Project; Tech. Specification Group Radio Access Network; Study on New Radio Access Technol., Physical Layer Aspects (Release 14), V14.3.0," Sep 2017.

[16] M. Cudak, A. Ghosh, T. Kovarik, R. Ratasuk, T. Thomas, F. Vook, and P. Moorut, "Moving Towards Mmwave-Based Beyond-4G (B-4G) Technology," in *Veh. Technol. Conf. (VTC-Spring), 2013 IEEE 77th*, Jun. 2013, pp. 1–5.

[17] M. Jacob, S. Priebe, T. Kürner, M. Peter, M. Wisotzki, R. Felbecker, and W. Keusgen, "Fundamental analyses of 60 GHz human blockage," in *2013 7th European Conference on Antennas and Propagation (EuCAP)*, April 2013, pp. 117–121.

[18] K. Akimoto, S. Kameda, M. Motoyoshi, and N. Suematsu, "Measurement of human body blocking at 60 ghz for inter-network interference of mmwave wban," in *2017 IEEE Asia Pacific Microwave Conference (APMC)*, Nov 2017, pp. 472–475.

[19] P. A. W. Lewis and G. S. Shedler, "Simulation of Nonhomogenous Poisson Point Processes by Thinning," *Naval Postgraduate School Rep.*, Jun 1978.

[20] M. Haenggi, *Stochastic Geometry for Wireless Networks.* Cambridge University Press, 2012.

[21] T. S. Rappaport, R. W. Heath, R. C. Daniels, and J. N. Murdock, *Millimeter Wave Wireless Communications.* Pearson Education Inc., 2015.

[22] "Rec. ITU-R P.526-14, Propagation by Diffraction," *ITU-R Recommendations*, 2018.

[23] "METIS Channel Model Tech. Rep. METIS2020 Deliverable D1.4 v3," Jul 2015, https://www.metis2020.com/wp-content/uploads/deliverables/METIS_D1.4_v1.0.pdf.

[24] A. Papoulis and S. U. Pillai, *Probability, Random Variables and Stochastic Processes*, 4th ed. McGraw-Hill Europe, 2002.

[25] T. S. Rappaport, *Wireless Communications*, 2nd ed. Prentice Hall, 2002.

[26] "IEEE Std. for Information Technology–Telecommunications and information exchange between LAN and MAN–Part 11: Wireless LAN Medium Access Control (MAC) and Physical Layer (PHY) Specifications Amendment 3: Enhancements for Very High Throughput in the 60 GHz Band," *IEEE Std 802.16.1-2012*, 2012, https://standards.ieee.org/findstds/standard/802.11ad-2012.html.

[27] A. Balanis, *Antenna Theory: Analysis and Design*, 4th ed. John Wiley and Sons, 2016.

[28] O. P. Gandhi and A. Riazi, "Absorption of Millimeter Waves by Human Beings and its Biological Implications," *IEEE Transactions on Microwave Theory and Techniques*, vol. 34, no. 2, pp. 228–235, Feb 1986.

[29] F. Khan and Z. Pi, "mmWave mobile broadband (MMB): Unleashing the 3-300GHz spectrum," in *Sarnoff Symp., 2011 34th IEEE*, May 2011, pp. 1–6.

[30] M. Zhang, M. Polese, M. Mezzavilla, S. Rangan, and M. Zorzi, "ns-3 Implementation of the 3GPP MIMO Channel Model for Frequency Spectrum above 6 GHz," in *arXiv.org*, Feb 2017, https://arxiv.org/pdf/1702.04822.

[31] S. Mhaske, A. Ameri, A. Aziz, and P. Spasojevic, "Implementation of the 3GPP TR 38.901 Channel Model," in *Github*, Dec. 2019, https://github.com/sdmgithub/3GPPChannelModelTR38901.

[32] "WP5: Propagation, Antennas and Multi-Antenna Techniques, D5.1: Channel Modeling and Characterization," *Millimetre-Wave Evolution for Backhaul and Access (MiWEBA)*, Jun 2014.

[33] "3GPP RAN WG1," in *3rd Generation Partnership Project (3GPP)*, 2016, http://www.3gpp.org/specifications-groups/ran-plenary/ran1-radio-layer-1/home.

[34] "3rd Generation Partnership Project; Tech. Specification Group Radio Access Network; Study on 3D channel model for LTE, V12.7.0," Dec 2017.

[35] "IST-4-027756: WINNER II Channel Models, D1.1.2 V1.2." Sep 2007.

[36] "IEEE Standard for Information technology– Local and metropolitan area networks– Specific requirements– Part 15.3: Amendment 2: Millimeter-wave-based Alternative Physical Layer Extension," *IEEE Std 802.15.3c-2009 (Amendment to IEEE Std 802.15.3-2003)*, pp. 1–200, Oct 2009.

[37] S. Collonge, G. Zaharia, and G. E. Zein, "Influence of the human activity on wideband characteristics of the 60 GHz indoor radio channel," *IEEE Trans. on Wireless Commun.*, vol. 3, no. 6, pp. 2396–2406, Nov 2004.

[38] P. Okvist, N. Seifi, B. Halvarsson, A. Simonsson, M. Thurfjell, H. Asplund, and J. Medbo, "15 GHz Street-Level Blocking Characteristics Assessed with 5G Radio Access Prototype," in *2016 IEEE 83rd Veh. Technol. Conf. (VTC Spring)*, May 2016, pp. 1–5.

[39] S. Mhaske, P. Spasojevic, A. Aziz, and M. Gul, "Link quality analysis in the presence of blockages for analog beamformed mm-wave channel," in *MILCOM 2016 - 2016 IEEE Military Communications Conference*, Nov 2016, pp. 219–224.

[40] L. Fenton, "The sum of log-normal probability distributions in scatter transmission systems," *IRE Transactions on Communications Systems*, vol. 8, no. 1, pp. 57–67, March 1960.

[41] C. Gabriel, S. Gabriel, and E. Corthout, "The dielectric properties of biological tissues: I. Literature survey," *Physics in Medicine and Biology*, vol. 41, no. 11, p. 2231, 1996. [Online]. Available: http://stacks.iop.org/0031-9155/41/i=11/a=001

[42] S. Gabriel, R. W. Lau, and C. Gabriel, "The dielectric properties of biological tissues: II. Measurements in the frequency range 10 Hz to 20 GHz," *Physics in Medicine and Biology*, vol. 41, no. 11, p. 2251, 1996. [Online]. Available: http://stacks.iop.org/0031-9155/41/i=11/a=002

[43] N. Chahat, M. Zhadobov, R. Augustine, and R. Sauleau, "Human skin permittivity models for millimetre-wave range," *Electronics Letters*, vol. 47, no. 7, pp. 427–428, Mar 2011.

[44] S. I. Alekseev and M. C. Ziskin, "Human skin permittivity determined by millimeter wave reflection measurements," *Electronics Letters*, vol. 28, no. 5, pp. 331–339, Mar 2007.

[45] T. Wu, T. S. Rappaport, and C. M. Collins, "The human body and millimeter-wave wireless communication systems: Interactions and implications," in *2015 IEEE International Conference on Communications (ICC)*, Jun 2015, pp. 2423–2429.

[46] "3rd Generation Partnership Project; Tech. Specification Group Radio Access Network; Multiplexing and Channel Coding, V15.7.0 Rel 15," Oct 2019.

[47] D. Costello and S. Lin, *Error Control Coding.* Pearson, 2004.

[48] "IEEE Std. for information technology–telecommunications and information exchange between LAN and MAN–Part 11: Wireless LAN medium access control (MAC) and physical layer (PHY) specifications," *IEEE P802.11-REVmb/D12*, pp. 1–2910, Nov. 2011.

[49] "IEEE standard for wireless MAN-advanced air interface for broadband wireless access systems," *IEEE Std 802.16.1-2012*, pp. 1–1090, Sep. 2012.

[50] "EN 302 307-1 V1.4.1, Digital Video Broadcasting (DVB); Second generation framing structure, channel coding and modulation systems for Broadcasting, Interactive Services, News Gathering and other broadband satellite applications; Part 1: DVB-S2 ," *ETSI 2014*, pp. 1–80.

[51] Y. Sun and J. Cavallaro, "VLSI architecture for layered decoding of QC-LDPC codes with high circulant weight," *IEEE Trans. Very Large Scale Integr. (VLSI) Syst.*, vol. 21, no. 10, pp. 1960–1964, Oct. 2013.

[52] K. Zhang, X. Huang, and Z. Wang, "High-throughput layered decoder implementation for QC-LDPC codes," *IEEE J. Sel. Areas Commun.*, vol. 27, no. 6, pp. 985–994, Aug. 2009.

[53] N. Onizawa, T. Hanyu, and V. Gaudet, "Design of high-throughput fully parallel LDPC decoders based on wire partitioning," *IEEE Trans. Very Large Scale Integr. (VLSI) Syst.*, vol. 18, no. 3, pp. 482–489, Mar. 2010.

[54] T. Mohsenin, D. Truong, and B. Baas, "A low-complexity message-passing algorithm for reduced routing congestion in LDPC decoders," *IEEE Trans. Circuits Syst. I: Reg. Papers*, vol. 57, no. 5, pp. 1048–1061, May 2010.

[55] A. Balatsoukas-Stimming and A. Dollas, "FPGA-based design and implementation of a multi-Gbps LDPC decoder," in *Int. Conf. Field Programmable Logic and Applicat.*, Aug. 2012, pp. 262–269.

[56] V. Chandrasetty and S. Aziz, "FPGA implementation of high performance LDPC decoder using modified 2-bit min-sum algorithm," in *Int. Conf. Comput. Research and Develop.*, May 2010, pp. 881–885.

[57] R. Zarubica, S. Wilson, and E. Hall, "Multi-Gbps FPGA-based low density parity check (LDPC) decoder design," in *IEEE Global Commun. Conf.*, Nov. 2007, pp. 548–552.

[58] P. Schläfer, C. Weis, N. Wehn, and M. Alles, "Design space of flexible multigigabit LDPC decoders," *VLSI Design, Hindawi Publishing Corp.*, vol. 2012, p. 4, 2012.

[59] E. Scheiber, G. H. Bruck, and P. Jung, "Implementation of an LDPC decoder for IEEE 802.11n using Vivado TM high-level synthesis," in *Int. Conf. Electron., Signal Process. and Commun. Syst.*, 2013, pp. 45–48.

[60] H. Kee, S. Mhaske, D. Uliana, A. Arnesen, N. Petersen, T. L. Riche, D. Blasig, and T. Ly, "Rapid and high-level constraint-driven prototyping using LabVIEW FPGA," in *IEEE Global Conf. Signal and Inform. Process.*, Dec. 2014, pp. 45–49.

[61] S. Mhaske, D. Uliana, H. Kee, T. Ly, A. Aziz, and P. Spasojevic, "A 2.48Gb/s FPGA-based QC-LDPC decoder: an algorithmic compiler implementation," in *IEEE 36th Sarnoff Symp.*, Sep. 2015, pp. 88–93.